A Linearized Free-Surface Method for Prediction of Unsteady Ship Maneuvering

by

Marc O. Woolliscroft

A dissertation submitted in partial fulfillment
of the requirements for the degree of
Doctor of Philosophy
(Naval Architecture and Marine Engineering)
in The University of Michigan
2015

Doctoral Committee:

Assistant Professor Kevin J. Maki, Chair
Assistant Professor Matthew D. Collette
Assistant Professor Eric Johnsen
Professor Armin W. Troesch

"Experience: that most brutal of teachers. But you learn, my God do you learn."

-C. S. Lewis

Dedicated to my family

ACKNOWLEDGEMENTS

Without doubt, this thesis is not solely a display of individual accomplishment. The presence of several people in my life motivate the production of this work in unique ways. I thank my advisor, Dr. Kevin Maki, for his continued support and patience throughout the course of my research. His ability to not only teach but also befriend I highly commend. I will appreciate his mentorship for my entire career. Dr. Armin Troesch and Dr. Matthew Collette provide me with invaluable knowledge and experiences through classes and conferences in addition to my doctoral work. Dr. Eric Johnsen is beneficial in offering a perspective outside the realm of naval architecture and marine engineering. I am a stronger student and engineering because of my committee members.

I would like to gratefully acknowledge Kelly Cooper of the U.S. Office of Naval Research and administer of program number N00014-13-1-0759 for providing funding for my education. Additional acknowledgment goes to the Flux HPC Cluster provided by the University of Michigan Office of Research and operated by the High Performance Computing Group at the College of Engineering. Travel funds for participation in an international workshop are kindly provided by the Rackham Graduate School. Also, thanks to the team at Engys for offering technical advice and consulting at the beginning stages of my thesis work.

My academic career is not possible without the support from my family, girlfriend, and friends who always encouraged me and provided me with refreshing distractions when a break from work was necessary. I am in debt to the friends that remain in

contact when I am less prone to do so. Most importantly, my parents, James and Elizabeth, show neverending love and support for me in all my endeavors. To all of you, please do not underestimate my gratitude.

TABLE OF CONTENTS

LIST OF FIGURES

Figure

LIST OF TABLES

Table

ABSTRACT

A Linearized Free-Surface Method for Prediction of Unsteady Ship Maneuvering

by

Marc O. Woolliscroft

Chair: Kevin J. Maki

Maneuvering prediction tools are valuable resources for naval and commercial ship designers. They estimate the ability of a ship to maintain or alter course. This enables designers to characterize the maneuvering performance of multiple conceptual hull forms and select an optimal design. A novel maneuvering prediction method is presented in this thesis. It is an unsteady Reynolds-averaged Navier-Stokes (URANS) approach that includes wave effects with linear free-surface boundary conditions. Therefore, it is a single-phase approach to solving multiphase problems. The solution of the URANS equations captures the viscous effects that are highly important in maneuvering due to the complex fluid interactions between the hull, propellers, and rudders. The linearized free-surface approximation accounts for first-order wave effects while reducing the necessary extents of the computational domain and the level of grid refinement required by nonlinear computational fluid dynamics (CFD) solvers. These simplifications lead to a substantial improvement in computational efficiency with respect to nonlinear methods, while retaining accuracy and empowering naval architects to obtain results earlier in the design cycle.

CHAPTER I

Introduction

Naval architects find balanced solutions between the main drivers in ship design. Speed, weight, space, and cost are routinely of the utmost concern. Primarily governed by the need to displace enough water in relation to the ship mass in order to float, the study of ship design uncovers a great deal of connectedness between these core drivers. Rarely is there an improvement in one area without adversely effecting another area to some degree. For example, new composite materials pose a great opportunity for savings in weight while maintaining high strength properties. Therefore, they can be ideal for high-speed applications. However, they are more expensive than traditional materials and require different methods of fabrication. In another case, it may be suggested that a smaller ship is generally less expensive to construct, but this obviously limits the amount of cargo that may be transported and is in contradiction with fundamental goals of commercial shipping companies. Also, naval warships can be made with thick steel plating to survive damage incurred in battles, yet this increases the weight of the ship which decreases the speed or increases fuel consumption. This may be overcome with a higher capacity powering system, but this in turn may require additional space and again increase weight. Clearly, ship design is a challenging problem. The inter-dependency of the engineering areas within the overall design causes a change in one area to propagate and require consideration

for subsequent changes in several other areas. It is the duty of naval architects to understand these connections and satisfy the requirements issued by ship owners for new vessel designs.

Maneuvering plays a large role within the highly-connected areas of ship design. Interactions between water, appendages, and control surfaces are not trivial. The boundary layer present on a hull as it moves through water accounts for a large viscous drag force. In addition, viscous separation can be generated from chines or sonar domes during maneuvering. Violent and chaotic flow features exist such as propeller cavitation and turbulence from appendages. Such widely varied flow features can be present near the transom where the most important appendages for maneuvering - rudders, propellers, skegs, et cetera - are located. Designing these control surfaces requires consideration of the effects they have on course-keeping, fuel efficiency, signatures, and so on. Making the proper design decisions is important because the maneuverability of a vessel has direct effects on safety and performance. For instance, a dynamically unstable ship needs proper skegs and rudders for frequent course-checking. However, large skegs and frequent use of the rudders has a negative impact on fuel consumption. On the other hand, a vessel which is too stable can not turn within a reasonable distance. The ability to operate in specific ports throughout the world requires various levels of maneuverability. Similarly, certain operations such as ship-to-ship replenishment and canal navigation necessitate a high level of vessel control. And furthermore, emergency situations need to be considered, and it must be demonstrated that a ship can adequately change direction and stop to help avoid catastrophic events.

However, these requirements create conflicting goals. Simple desires such as a low hull resistance and the ability to stop quickly do not necessarily go hand-in-hand. This leads to a design space containing conceptual hull forms, each of which satisfy the design requirements to various degrees. The goal of a naval architect is to evaluate the

trade offs within the design space and deliver an optimal solution. Nevertheless, real-world constraints such as schedules and budgets often result in a partial exploration of novel hull forms. These design ideas resonate with those of set-based design, as opposed to point-based design, discussed in Singer et al. (2009). Typically, historical hull forms are used as a starting point. On one hand, it may be argued that an existing hull can fully satisfy the requirements of a new design, but this approach lacks a motivated effort to evolve the designs of the largest transportation vehicles in the world. It simply does not push designs toward an optimized form. But, this is not to suggest that high fidelity technologies are not available.

Surely, computational fluid dynamics (CFD) and structural finite-element methods (FEM) exist and are in use from time-to-time for design analysis. Even the highly-important problem of arrangements on warships is the focus of early-stage optimization efforts (Parsons et al., 2008; Gillespie, 2012). However, these tools can be difficult to use requiring specially-skilled and well-trained designers. At times, expensive licensing fees are associated with the use of high fidelity design software. In addition, structural and fluid dynamics simulations can be very time-consuming. These are all factors which limit the wide-spread use of such advanced tools. Still, on rare occasions, a more original design may be pursued using high fidelity hydrodynamic methods, but determining the maneuvering characteristics with these methods is a difficult task.

Currently, maneuvering prediction capabilities consist of geometrically scaled model tests and a variety of numerical methods. Model tests can provide a plethora of data, helpful for studying ship motions as well as fluid dynamics, but they require expensive facilities, models, and instruments, as well as methods to account for scaling effects (Cope, 2012; Ueno et al., 2014). Numerical methods vary from inviscid potential flow codes to multiphase CFD. Historically, the velocity potential framework provides solutions to several ship-motions problems, ranging from stability assessment

to the overtaking of one ship by another (Sclavounos and Thomas, 2007; Newman and Tuck, 1974). But potential flow codes inherently lack the ability to capture viscous separation, which is especially significant near the hull appendages that influence maneuverability. Viscosity can not be ignored in complex, fully-inclusive simulations involving rotating propellers moving a hull through a real fluid. On the other hand, CFD and model tests can be used to obtain viscous predictions on hulls with appendages (Broglia et al., 2013). However, these are costly and time-consuming. Most designers do not have the computational resources necessary for unsteady CFD simulations. Systems-based methods use equation-of-motion coefficients that have been obtained from physical experiments or CFD to predict maneuvering capabilities. These coefficients become less accurate with large motions or with changes in hull geometry.

The main drawbacks of the existing technologies make them limited for hull form optimization in early stages of design. Therefore, it is an important endeavor to provide efficient and accurate tools that allow for a broad exploration of the design space and the ability to develop more optimized designs within realistic time and monetary constraints. A maneuvering prediction tool is presented in this thesis to achieve this goal, but first it is necessary to define the important aspects of the ship maneuvering problem.

1.1 Definition of Maneuvering

Maneuvering may be defined as ship motions caused by the interaction between water and all surfaces of a vessel with which it is in contact. It is important to note just how many surfaces this may include; the hull, bilge keels, rudders, stabilizer fins, propellers, skegs, exposed struts and shafts, bulbous bows, gondolas, and all other underwater appendages that interact with the water. Indeed, many of these surfaces have been developed for the exact purpose of dictating maneuvering characteristics.

Termed control surfaces, these may be passive, as with skegs, or active, as with rudders. Typical maneuvers include turning, stopping, and docking.

Maneuvering consists of low frequency ship motions usually requiring $\mathcal{O}(10-100)$ seconds and $\mathcal{O}(1-10)$ ship lengths, L, to perform. Other scales to consider include oncoming waves occurring with frequencies corresponding to $\mathcal{O}(10)$ seconds and propeller rotations every $\mathcal{O}(1)$ second with blade-passings occurring more frequently. Scales of $\mathcal{O}(0.01)$ seconds and smaller are needed to describe turbulence. Overall, waves and other environmental factors affect maneuvering, but motions associated with maneuvering occur at lower frequencies than oncoming waves, making it very different than the study of seakeeping.

1.2 Design for Maneuverability

Upon receiving owner requirements for a novel ship design, maneuverists within a design team have several options available to begin analyzing hull forms. Unlike airplanes or automobiles, ships are unique because full-scale prototypes are infeasible due to the enormous cost and time associated with constructing entire ships. This leads one to consider a more reasonable approach; one in which a hull is scaled to a smaller size. Geometrically scaled models let designers use towing tanks and maneuvering basins to characterize hull forms in a physical setting. Here, they can prescribe trajectories, many of which are not even possible at full scale, in order to obtain very specific information about the hydrodynamic forces present during maneuvering.

A high-fidelity alternative to model testing is fully nonlinear, multiphase CFD. In this digital setting, designers are not limited by testing facilities or machining tools, so meshes for multiple hulls may be tested simultaneously. Obviously, this is instead limited by the computing resources available to the designers. A patent benefit of numerical simulations is the possibility to perform analyses at a full scale Reynolds

number. These are not yet common, but obtaining solutions to full scale problems while avoiding full scale construction holds great potential value.

Clearly, both physical experiments and nonlinear CFD simulations are important tools for the study of ship maneuvering. They have been developed and improved upon for decades, and they will remain widely-used in the future. However, the use of these approaches comes with difficulties that can not be denied; difficulties that hinder the idea of designing for maneuverability.

The Maritime Research Institute Netherlands (MARIN) reports constructing 150 models during the 2009 calender year using a CNC milling device which can be operated 24 hours a day (de Boer, 2009). The year prior, Strock and Brown (2008) use the U.S. Navy Advanced Ship and Submarine Evaluation Tool (ASSET) to generate 8,841 conceptual designs of a ballistic missile defense cruiser. ASSET is a multi-platform design tool offering modules such as hull form, structures, resistance, propulsion, machinery, weight, and spaces; but not maneuvering. Of the 8,841 designs, 156 are "non-dominated," or unique designs which should be explored further and compared to determine strengths and weaknesses. Also in 2008, a nonlinear CFD simulation of a bare hull 5415 model takes approximately 320 CPU hours to simulate a 7.5 second maneuver (Miller, 2008). If the same computation is applied to the 156 non-dominated designs, nearly 50,000 CPU hours are required, and this ignores time required for meshing, data transfer, post-processing, et cetera.

Undoubtedly, there is space for improvement. Tools such as ASSET make it possible to generate thousands of designs and truly explore a design space for optimized solutions. However, state-of-the-art research centers such as MARIN and nonlinear CFD simulations can not be used extensively at this stage. ASSET does provide resistance estimation, but it is from the Holtrop-Mennen regression-based method (Holtrop and Mennen, 1978, 1982). Certainly, the novel designs being generated may differ greatly from the data used to construct the regression. Therefore, an oppor-

tunity exists for the development of efficient physics-based maneuvering prediction methods that can be used in early stages of design.

The ability of a vessel to adequately stop, change direction, and maintain course is key to performance and safety. Navigating through the entrances of ports may require a specific path to avoid obstructions and other vessels. In a more extreme situation, a drastic change in direction and speed may be necessary to prevent a catastrophic collision. Ship size and operating requirements help dictate desired maneuvering characteristics. Therefore, qualifications of ideal maneuverability differ between vessels with different purposes. For example, a small patrol boat may actually be designed to have low stability characteristics that allow for increased agility. In addition to intended purpose, environmental factors such as water depth, channels, waves, and currents influence maneuverability (Lincoln et al., 1989). The combination of these factors and conflicting operational requirements make designing vessels for maneuverability a truly complex problem.

In addition to owner requirements, regulatory bodies drive the design for particular maneuvering qualities. Due to the need for a certain level of low frequency ship motion control, the International Maritime Organization (IMO) has developed maneuvering requirements for vessels over 100 meters in length. Requirements consist of turning circle, zig-zag, and crashback (stopping) tests which are intended to measure course-keeping, course-changing, and stopping abilities (IMO, 2002). The vessel length and speed are often used as criteria to determine if these have been completed satisfactorily. For instance, the diameter of a turning circle must be less than five ship lengths.

Furthermore, the American Bureau of Shipping (ABS) classification society, requires that vessels demonstrate the ability to successfully perform these IMO maneuvers during sea trials (ABS, 2006). The standards allow owners to conduct the maneuvers in a condition other than full load only if predictive maneuvering analysis

has been performed at the design stage and deemed satisfactory. If trials are undergone in a condition other than full load, the results must agree with those obtained with predictions. It is then assumed that the full load condition will agree with the full load condition from the design stage. If predictions are not available, the sea trials must be performed at the full load condition (Belenky and Falzarano, 2006). Generally, this is not achievable due to the volume and expense of cargo that needs to be on board, so maneuvering prediction during the design stage is almost always necessary. Regardless, attempting to fulfill IMO maneuvering requirements only during the full scale sea trials comes with great risk as this can lead to unsatisfactory results causing costly hull form modifications, especially for novel designs that lack historical data.

The linearized URANS method provides the ability for physics-based maneuvering predictions in earlier design stages than nonlinear CFD or model tests. It relies on first principles of free-surface boundary conditions as a basis for this novel approach. The free-surface boundary conditions are considered in the classical linearized form, but developed under the RANS variables for a viscous, turbulent fluid. Other state-of-the-art technologies such as semi-automatic mesh generation, turbulence modeling, and sliding mesh interfaces are coupled with this idea for an efficient and accurate design solution to maneuvering prediction.

The development of the linearized URANS method herein primarily concerns ship maneuvering problems from an inertial, Earth-fixed frame of reference. Forces and moments are of the highest importance, but flow field information is also discussed. In Chapter II, current state-of-the-art solutions to maneuvering problems are discussed. A theoretical presentation of the fully nonlinear free-surface boundary conditions appears in Chapter III. Also in this chapter, analysis is presented of the linear conditions for a viscous, turbulent flow. Next, Chapter IV introduces the specific numerical aspects of the linearized URANS method. This is a new formulation

to the ship maneuvering problem, where linear free-surface boundary conditions are solved with a RANS approach in an Arbitrary Lagrangian-Eulerian manner. This is followed by a two-dimensional transom stern study found in Chapter V. An investigation of the magnitude of viscous and nonlinear terms at the air-water interface offers justification for the linearization performed on the free-surface boundary conditions. This numerical study is beneficial because previous studies of turbulent free-surface flows do not correspond to the large Reynolds-number regime that characterizes ship flows. In addition, a free-surface piercing body is not always the focus for these previous investigations. Chapter V also compares results computed using the linearized free-surface conditions to those obtained with the fully nonlinear CFD solver. This canonical study is challenging for linear free-surfaces approaches, but the linearized URANS method performs well. The use of the linearized URANS method is expanded to a variety of maneuvering tests on two versions of the David Taylor Model Basin (DTMB) 5415 destroyer hull in Chapter VI. One version is fitted with only bilge keels, while the other is fully appended and operates with rotating propellers. The demonstration of this novel method on a real bare hull ship model is shown to be accurate, and the computational cost is significantly less than for nonlinear CFD. Lastly, this work is summarized in Chapter VII with a discussion of additional research possibilities.

CHAPTER II

Background

The main focus of this thesis is to present a novel approach to numerically predict the maneuverability of bodies near or in contact with a free-surface. The unique qualities of the work reside in the judicious linearization with conventional RANS variables to deliver accurate and fast-running simulations. First, it is necessary to address the common prediction techniques currently used in design.

2.1 Maneuvering Prediction Methods

Since there is a great need for maneuvering prediction capabilities in ship design, it is important to address the common techniques currently available. In the most basic form, maneuvering prediction requires the study of equations of motion in the horizontal plane. Referring to the coordinate system shown in Figure 2.1, the surge force X, the sway force Y, and the yaw moment moment N, can be expressed as a function of the velocities and accelerations of the ship in this horizontal plane (Lincoln et al., 1989). There exists an Earth-fixed coordinate system described with x and y, which is initially aligned with the ship-fixed coordinate system, having origin, O. The ship has a velocity of U with a bow-aligned component u and a lateral component v. The angle between the velocity and the bow-aligned axis is the drift angle, β, and the angle between the original, bow-aligned x-axis and some new bow-aligned axis is

the heading angle, ψ. The rate with which the ship rotates in the horizontal plane is the yaw rate, r. Lastly, the deflected position of the rudder can be described with the rudder angle, δ.

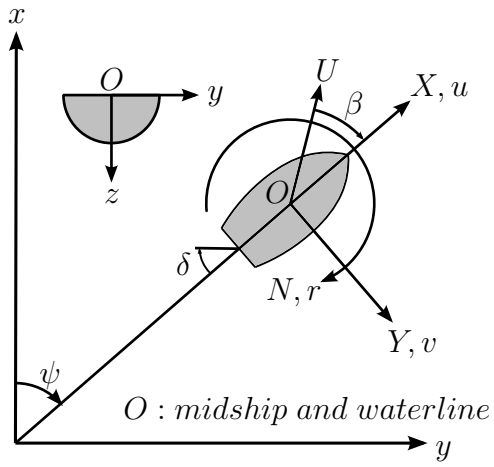

Figure 2.1: Ship maneuvering coordinate system

$$\begin{aligned} X &\approx F_x\left(u_1, v_1, \dot{u}_1, \dot{v}_1, \dot{\psi}_1, \ddot{\psi}_1\right) + (u-u_1)\,X_u + (v-v_1)\,X_v + \cdots + \left(\ddot{\psi}-\ddot{\psi}_1\right) X_{\ddot{\psi}} \\ Y &\approx F_y\left(u_1, v_1, \dot{u}_1, \dot{v}_1, \dot{\psi}_1, \ddot{\psi}_1\right) + (u-u_1)\,Y_u + (v-v_1)\,Y_v + \cdots + \left(\ddot{\psi}-\ddot{\psi}_1\right) Y_{\ddot{\psi}} \\ N &\approx F_\psi\left(u_1, v_1, \dot{u}_1, \dot{v}_1, \dot{\psi}_1, \ddot{\psi}_1\right) + (u-u_1)\,N_u + (v-v_1)\,N_v + \cdots + \left(\ddot{\psi}-\ddot{\psi}_1\right) N_{\ddot{\psi}} \end{aligned} \tag{2.1}$$

Shown in Equation 2.1 are Taylor series expansions which are used to approximate the ship forces. This is a traditional approach to analyze maneuvering. In this case, a linear approximation is shown, but nonlinear approximations can be made with higher-order and cross-coupled terms including the rudders. These equations include velocity $(u, v, \dot{\psi})$ and acceleration $(\dot{u}, \dot{v}, \ddot{\psi})$ terms and initial conditions, denoted with numerical subscripts. Also included are terms referred to as either force and moment derivatives, hydrodynamic derivatives, or maneuvering coefficients. These are shown with X_u, Y_u, $N_{\ddot{\psi}}$, et cetera, and they indicate changes in the forces or moment due to a velocity or acceleration imposed on the hull. For example, Y_u represents the change in sway force due to a surge velocity. These derivatives depend on the geometry of

a hull, and can be zero with symmetry. A hull which is symmetric about centerline does not induce lateral motions due to surge, so $Y_u = Y_{\dot{u}} = N_u = N_{\dot{u}} = 0$.

Solutions to these expansions can provide designers with details about the stability characteristics of a vessel. For a vessel traveling at a constant speed in calm water, a disturbance can result in several types of stability or instability depending on the hull form and subsequent rudder deflections. Some examples are shown in Figure 2.2. There exist several experimental and numerical approaches to determine the maneuvering coefficients, as well as more direct methods to maneuvering prediction.

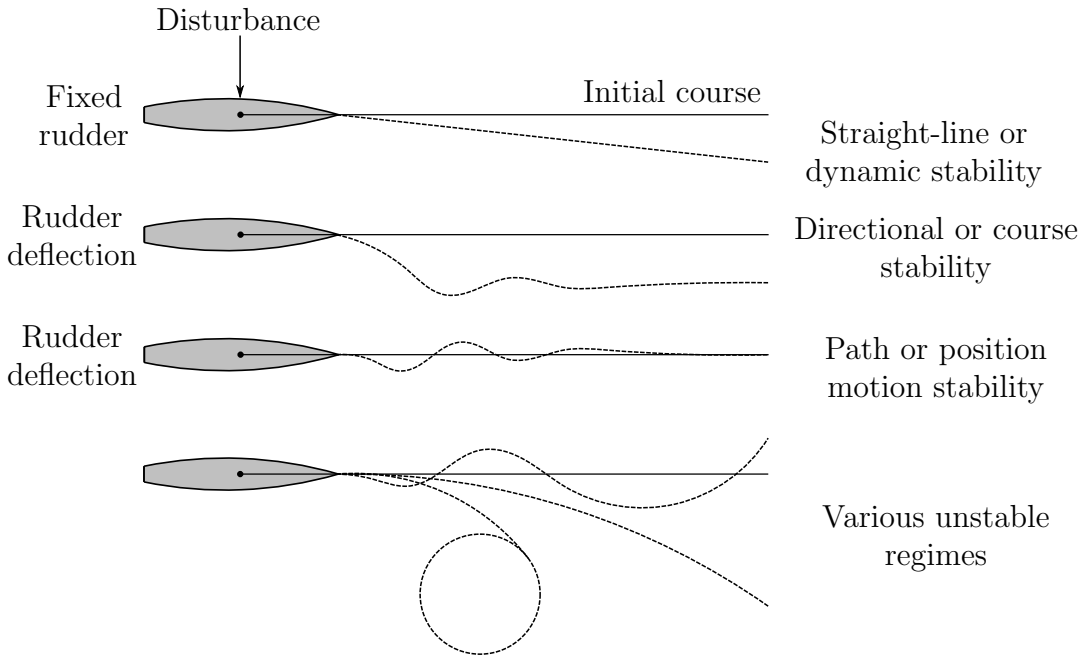

Figure 2.2: Various types of maneuvering stability and instability

2.1.1 Experiments

A popular method for obtaining hydrodynamic derivatives is physical experiments with a scaled model. This approach uses a tow-tank or maneuvering basin and prescribed trajectories which the model is forced to follow in order to obtain the desired maneuvering coefficients. Solutions can then be found to the set of equations in Equation 2.1 to numerically model zig-zags or turning circles. However, self-propelled

model tests can also be performed which allow for direct prediction of the turning circles and zig-zag maneuvers that are performed at full scale.

2.1.1.1 Captive model tests

Captive model tests are performed with either a planar motion mechanism (PMM) or a rotating arm for circular motion tests (CMT). Prescribed motions in the horizontal plane (surge, sway, and yaw) allow experimentalists to characterize hull forms in very specific ways. Examples of pure sway and pure yaw tests are shown in Figure 2.3. A pure drift test can be performed by fixing the model at a nonzero drift angle β and running the carriage with no oscillation from the PMM. The experiments can determine the force and moment derivatives necessary for solving the equations of motion.

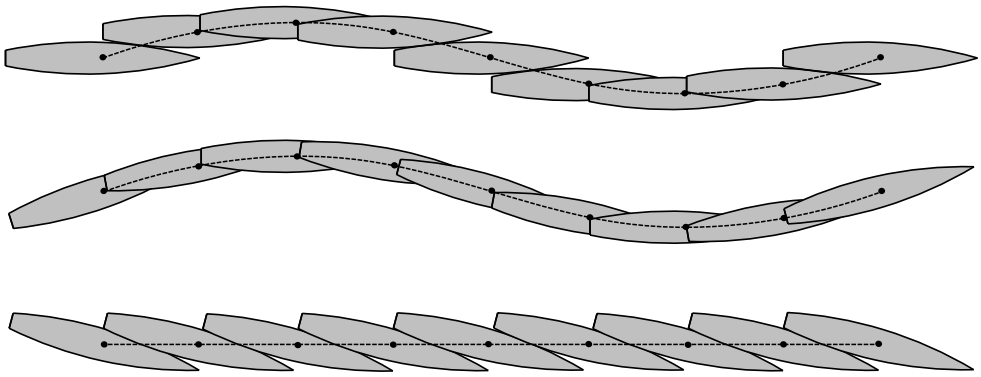

Figure 2.3: Pure sway (top), pure yaw (middle), and static drift (bottom) PMM tests

For example, to determine the change in lateral force with respect to a change in lateral velocity, Y_v, static drift tests are performed at various drift angles. A transducer measures the force and moment on the model, and the sway velocity is obtained with $v = U \sin \beta$ where U is the carriage velocity. Then, Y is expressed as a function of v and the value of the velocity derivative, Y_v, is found by calculating the slope of the relation. One can see that the carriage velocity could be varied while keeping the drift angle constant to acquire a range of sway velocities and replicate

the same experiment. However, Reynolds scaling can not be achieved due to the unattainable speeds at which the carriage is required to move. Therefore, boundary layers are not correctly scaled between the model and ship. This difference in viscous effects is especially important near the transom when considering the forces on the rudder – the most influential control surface in maneuvering.

The CMT method can also be used to find the derivatives for the equations of motion. It works by moving the model in a circle about a vertical axis fixed in a basin. The radius of rotation, drift angle, and yaw motion can be varied to obtain the necessary derivatives. The PMM and rotating arm methods can also be performed with rudders at various deflection angles and propellers operating at the ship propulsion point. Therefore, both are suitable in providing information that can be used to quantify nonlinear and cross coupling effects. Cross coupling is the effect that force derivatives have on each other.

2.1.1.2 Free model tests

Compared to captive model tests, free model tests are a more direct approach at predicting full scale maneuvering capabilities. Turning circles, zig-zags, and reverse spirals can be performed using a remotely operated, self-propelled model. Several criteria must be met for these tests to scale accurately. The propeller slip ratio of the model and full scales should be equal. To satisfy this requirement, an air propeller can be used to provide a portion of the thrust (Ueno et al., 2014). Also, the motor powering the model propeller should be equipped with a thrust and torque transducer to simulate the full scale engine characteristics that change during various maneuvers (Pivano, 2008). This is sometimes ignored, resulting in model tests that predict less speed loss than full scale tests. The inability to satisfy Reynolds scaling produces inconsistencies between model and full scale boundary layer thicknesses. Propellers have even been seen operating in a laminar regime (Cope, 2012). Turbulence inducing

measures can be implemented, but this scaling issue significantly restricts free model tests from accurately predicting stopping maneuvers (ITTC, 2002). Overall, the viscous force inaccuracies are even greater in free model tests than captive tests because of the interactions between the rudder, propeller, and hull. In addition to these difficulties, free model tests require large maneuvering basins to insure that data are not affected by the tank boundaries and simply that there is ample space in which to perform a full maneuver with a large model. Some facilities do not have this capability. Thus, they are forced to perform partial maneuvers and extrapolate data.

2.1.1.3 Systems based methods

Nonlinear maneuvering simulations in the time-domain can be performed with systems based methods. These mathematical models use force and moment derivatives to solve the equations of motion. The derivatives can be obtained using empirical data (Furukawa et al., 2008), model tests (Kim and Kim, 2008), or CFD (Simonsen et al., 2012). The use of empirical data introduces uncertainty with the design of original hull forms. Model tests and CFD are time-consuming, so while a maneuvering simulation may be fast with a systems based method, the data necessary to solve the equations of motion are not easily gathered quickly. In addition, a lack of consistency between models can be seen, showing a significant amount of sensitivity due to different model inputs.

2.1.2 Numerical Simulations

Several state-of-the-art numerical approaches currently exist for examining the flow around vessels undergoing steady or unsteady maneuvers. Ranging from inviscid potential flow tools to fully nonlinear CFD, these methods vary widely in the resources required and data attainable.

2.1.2.1 Inviscid methods

Potential flow methods for maneuvering prediction may be efficient due to the boundary-integral nature of the formulation, opposed to solving equations in a field. And this efficiency may appeal to designers. However, these approaches are also inviscid in nature. Therefore, viscous separation is not resolved. Free surface elevations at large drift angles and fluid forces on rudders are areas where the inviscid assumption significantly affects predictions. For example, aft of the transom, rudders are positioned in an area of highly rotational flow. The irrotational qualities stemming from the inviscid assumption make for poor predictions of the forces on rudders (Söding, 1999). These forces are very important for maneuvering. Viscous approximations can be made using empirical data or corrections from supplemental CFD simulations. Results from Kring et al. (2011) show good prediction of maneuvering forces on a surface effect ship in waves using a potential flow method and viscous correction from CFD. However, empirical data are limited to similar hull forms and may not be applicable to novel designs. The use of CFD corrections can lead to questions of whether potential methods possess enough fidelity for a wide range maneuvering prediction despite the possibility of fully nonlinear, time-domain solutions (Tanizawa and Naito, 1998). The overwhelming drawback lies in viscosity being neglected and challenges encountered in trying to overcome this shortcoming.

2.1.2.2 Viscous methods

Common viscous methods solve for flow information on boundaries as well as within fluid domains by seeking solutions to the URANS equations. Large-eddy simulation (LES) is another viscous approach, but the URANS method is the main concern for this nonlinear CFD discussion. The multiphase volume-of-fluid (VOF) method solves the URANS equations in two fluids - air and water. Sufficient accuracy and numerical stability depend on the adequacy of the grid refinement required to capture the air-

water interface. The computational cells (control volumes) need to be small in order to resolve breaking waves, far-field waves, et cetera. Small time steps stem from these highly resolved grids which are necessary even far from the hull. Work of Maki and Wilson (2008) shows forces from a steady drift test using a VOF method that are very comparable to experiments. Several free-running simulations on a variety of hulls are shown in Shen et al. (2014).

A level-set approach can be used in a single phase or multiphase manner for maneuvering prediction. Here, a signed distance function (level-set) is solved to determine the location of the interface. Steep waves can be handled with this approach. Simulations of captive model tests have been performed with a single phase level-set to obtain maneuvering coefficients (Araki et al., 2014). In addition, free model turning circle and zig-zag tests have been simulated at model and full scale (Carrica et al., 2012; Broglia et al., 2013).

Alternatives to surface capturing methods are surface tracking methods. These use grid deformation to estimate an evolving free surface. Relatively simple forward-speed resistance problems have been possible for some time (Kim, 2002). Surface tracking has also been used for a numerical study on a constant turn maneuver (Burg and Marcum, 2003). Small time-steps and numerical stability become issues since the extent of grid deformations must be regulated. Surface tracking methods have issues in the simulation of breaking waves due to the overturning of the wave and domain.

Finally, zero Froude number (double body) approximations enforce a flat free surface. Therefore, the significant presence of the viscous effects is captured while neglecting waves. Depending on the Froude number, this reduction in accuracy may be accepted due to the increase in efficiency compared to multiphase approaches. For example, maneuvering in ports or ship-to-ship operations are cases where this method can yield accurate results. Turnock et al. (2008) suggests that double-body simulations can be roughly 1,000% faster than a VOF approach. Low Froude number

simulations have been shown to compare well with experimental results of static drift tests (Wang et al., 2008) and of pure sway tests (Turnock et al., 2008). Toxopeus (2009) shows good agreement of bare hull forces to experiments when using double approximations with Froude numbers less than $Fr = 0.2$. In addition, Broglia et al. (2008) and Hochbaum et al. (2008) have performed pure yaw simulations with a flat free surface.

Overall, nonlinear CFD can produce impressively accurate solutions of maneuvering simulations. The VOF and level-set methods are two high-fidelity, well-studied tools that should be utilized when the expense required for them is acceptable. The capability of modeling the viscous effects in addition to a nonlinear free surface, possibly with breaking waves, is established as state-of-the-art. But these methods do not greatly impact design because of expense, difficulty, and time.

2.1.3 Summary

Model tests require large facilities and the construction of accurately scaled models. For low frequency PMM tests, even long tanks may allow for only two or three periods of motion. The inability to satisfy Reynolds scaling severely affects the accuracy of rudder-induced motions, especially with free model tests because the interactions between hull, propeller, and rudder are not easily scaled. Furthermore, the need to produce physical models is expensive and time-consuming which limits the amount of changes one can make on a hull form. The cost of materials for a single 4.9 meter model with propellers and rudders can be approximately 70,000 USD (Cope, 2012) This is not conducive to hull form iterations required at early stages of design. The limitations model tests and systems based methods pose for early phase design have motivated the development of numerical methods.

Numerical methods possess their own set of limitations. Double-body formulations give little information on the shape of the free surface and force an incor-

rect no-penetration condition on velocity. In turn, this adversely affects the solution to the pressure in the flow which becomes problematic at Froude numbers greater than $Fr = 0.1$. The use of surface tracking requires grid deformation which is time-consuming and difficult to perform accurately, especially when breaking waves are present. Likewise, the main drawback for each of the fully nonlinear methods is computational expense. Even with recent advancements in parallel computing, the grid refinement and computational requirements are burdening in nature. Currently, the time and computational resources needed for these approaches make their use impractical in early stages of design. The need to include water and air portions within a domain and the high grid resolution required, even far from the body, greatly increases the number of cells.

The linearized URANS method aims to improve the maneuvering prediction capabilities - from forward speed resistance tests to the simulation of free running model tests - available to designers. The development of the technology embodies fast-running simulations and simplified physics to more completely explore design spaces for optimized solutions to modern naval architecture needs.

CHAPTER III

Free-Surface Boundary Conditions

The linearized URANS method is a single-phase approach to solving multiphase problems. Efficiency is sought through the use of a linearized free-surface approximation. This is opposed to solving for an air-water interface or a nonlinear free-surface and requires an investigation of the kinematic and dynamic boundary conditions associated with a free-surface as well as an appropriate procedure for linearization. A discussion of such matters is presented in this section.

3.1 The Air-Water Interface

In a physical setting, floating bodies pierce an air-water interface at which stresses between the the two fluids are in balance. Therefore, the jump in stress is zero, $\left[\left[\overline{\overline{\sigma}} \cdot \hat{n}\right]\right] = 0$. For more detail, see Rood (1995), van Brummelen (2002), and Yeh (1995). An all-inclusive description of these stresses contains effects from surface tension. However, this cohesive molecular property is ignored in the present investigation of ship flows. Bubbles, droplets, and other features that depend on surface tension are not considered significant for maneuvering prediction compared to inertial and viscous forces. As such, the stress (and force) from the water must be in balance with

the stress (and force) from the air at the air-water interface,

$$\overline{\overline{\sigma}}_{\text{water}} \cdot \hat{n} - \overline{\overline{\sigma}}_{\text{air}} \cdot \hat{n} = \vec{0} \tag{3.1}$$

where $\hat{n}$ is a common unit normal vector for both fluids, pointing out of the water into the air as shown in Figure 3.1. The total stress tensor for each fluid is denoted with $\overline{\overline{\sigma}}$.

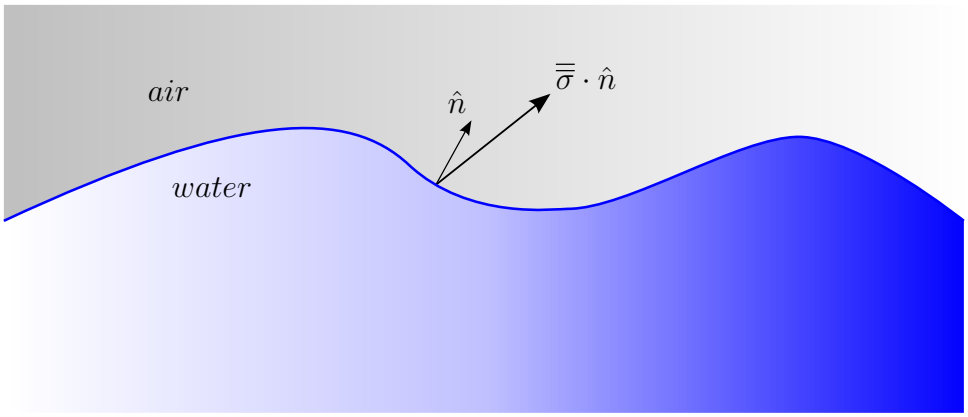

Figure 3.1: Stress at the air-water interface

The large differences between the values of density and viscosity in air and water are the source for free-surface assumptions. When no wind is present, the dynamic effect from the air on the surface of the water is virtually nonexistent. Therefore, the stress from the air is ignored, and the problem is reduced from an air-water interface to a free-surface condition:

$$\overline{\overline{\sigma}}_{\text{water}} \cdot \hat{n} = \vec{0} \tag{3.2}$$

Employing a free-surface approximation is integral to the linearized URANS method. In addition, the free-surface boundary conditions are made linear and inviscid. The inviscid condition is not used out of convention but rather because the role of viscous stress is assumed small at the air-water interface. This assumption is analyzed in detail in Chapter V, where the implications of simplifying from a multiphase ship maneuvering environment are studied.

3.2 Nonlinear Free-Surface Boundary Conditions

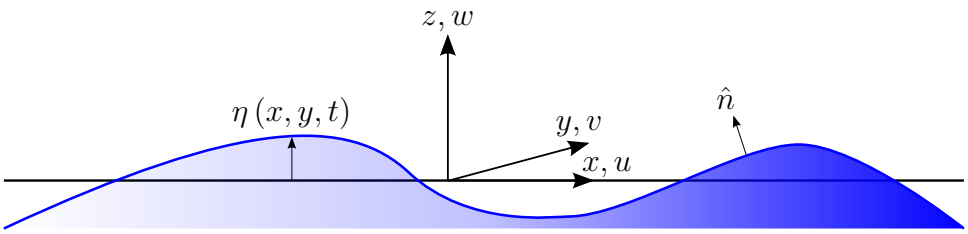

Figure 3.2: Example of nonlinear free-surface

To develop linear kinematic and dynamic free-surface boundary conditions to complement the viscous URANS equations, one must first consider the fully nonlinear forms. Referring to Figure 3.2, the origin is located at the calm-water plane. Space is represented in a three-dimensional, Cartesian manner with x, y, and z. The fluid velocity vector, $\vec{U} = u\hat{i} + v\hat{j} + w\hat{k}$, contains components which act along the three spatial axes. The free-surface elevation is η and is a function of x, y, and time, t. Lastly, the unit vector, $\hat{n}$, which is normal to free-surface everywhere and at all times, points out of the water. The kinematic boundary condition requires that a particle on the free-surface remains on the free-surface. This is shown with the relative velocity between the fluid and the free-surface itself:

$$\vec{U} \cdot \hat{n} - \vec{U}_{\text{fs}} \cdot \hat{n} = 0 \tag{3.3}$$

$\vec{U}_{\text{fs}}$ is the velocity of the free-surface. To express the condition in terms of the free-surface elevation, the location of the free-surface may be defined with a function:

$$F(x, y, z, t) = z - \eta(x, y, t) = 0 \tag{3.4}$$

The value of the function in 3.4 is always zero on the surface. As such, the total

derivative of the function is also zero on the surface:

$$\frac{DF}{Dt} = \frac{\partial F}{\partial t} + \vec{U} \cdot \nabla F = 0 \tag{3.5}$$

Evaluating the total derivative of the free-surface function in terms of η results in:

$$-\eta_t + u\left(-\eta_x\right) + v\left(-\eta_y\right) + w = 0 \tag{3.6}$$

By rearranging, the fully nonlinear kinematic free-surface boundary condition is obtained:

$$w = \eta_t + u\eta_x + v\eta_y \tag{3.7}$$

The dynamic free-surface boundary condition can be derived by invoking a zero total stress condition. Since this is a free-surface, only the stresses in the water are of concern, and the fluid subscript is dropped ($\sigma = \sigma_{\text{water}}$). Deeming surface tension insignificant for ship waves, the total stress tensor is composed of an isotropic term and a viscous term:

$$\overline{\overline{\sigma}} = -P\overline{\overline{I}} + \overline{\overline{\tau}} \tag{3.8}$$

Here, P is the total pressure, $\overline{\overline{I}}$ is the diagonal identity matrix, and the viscous stress tensor is τ. The total pressure is composed of a hydrodynamic and a hydrostatic part:

$$P = p + \rho\vec{g} \cdot \vec{x} \tag{3.9}$$

The gravitational acceleration vector is $\vec{g}$, and the position vector is $\vec{x}$. In conjunction with the coordinate system currently in use, the hydrostatic pressure can be described

as follows:

$$\vec{g} = -g\hat{k} \tag{3.10}$$

$$\rho\vec{g} \cdot \vec{x} = -\rho g z \tag{3.11}$$

At the water surface, $z = \eta$. The incompressible viscous stress tensor is:

$$\overline{\overline{\tau}} = \mu\left(\nabla\vec{U} + \left(\nabla\vec{U}\right)^T\right) \tag{3.12}$$

The dynamic viscosity is represented by μ. Expanding the viscous stress tensor gives:

$$\overline{\overline{\tau}} = \mu\begin{bmatrix} \left(u_x + u_x\right) & \left(u_y + v_x\right) & \left(u_z + w_x\right) \\ \left(v_x + u_y\right) & \left(v_y + v_y\right) & \left(v_z + w_y\right) \\ \left(w_x + u_z\right) & \left(w_y + v_z\right) & \left(w_z + w_z\right) \end{bmatrix} \tag{3.13}$$

Seeking a zero total stress boundary condition implies:

$$\overline{\overline{\sigma}} \cdot \hat{n} = \vec{0} \tag{3.14}$$

The unit normal vector can be written as:

$$\hat{n} = q\hat{i} + r\hat{j} + s\hat{k} \tag{3.15}$$

In expanded form, the total stress vector appears as:

$$\overline{\overline{\sigma}} \cdot \hat{n} = \begin{bmatrix} -\left(p - \rho g z\right)q & + & \mu\left(2u_x q + \left(u_y + v_x\right)r + \left(u_z + w_x\right)s\right) \\ -\left(p - \rho g z\right)r & + & \mu\left(\left(v_x + u_y\right)q + 2v_y r + \left(v_z + w_y\right)s\right) \\ -\left(p - \rho g z\right)s & + & \mu\left(\left(w_x + u_z\right)q + \left(w_y + v_z\right)r + 2w_z s\right) \end{bmatrix} \tag{3.16}$$

The function $F = (x, y, z, t)$ from Equation 3.4 is used to express the normal vector

in terms of the free-surface elevation:

$$\hat{n} = \frac{\nabla F}{\mid \nabla F \mid} = \frac{-\eta_x \hat{i} - \eta_y \hat{j} + \hat{k}}{\sqrt{\eta_x^2 + \eta_y^2 + 1}} \tag{3.17}$$

Using the normal vector from Equation 3.17 and performing the operation to obtain the total stress vector, $\overline{\overline{\sigma}} \cdot \hat{n}$, results in the fully nonlinear, dynamic free-surface boundary conditions in the x, y, and z-directions, respectively:

$$\begin{aligned}
(p - \rho g \eta)\, \eta_x - 2\mu u_x \eta_x - \mu\,(u_y + v_x)\, \eta_y + \mu\,(u_z + w_x) &= 0 \\
(p - \rho g \eta)\, \eta_y - \mu\,(v_x + u_y)\, \eta_x - 2\mu v_y \eta_y + \mu\,(v_z + w_y) &= 0 \\
-\,(p - \rho g \eta) - \mu\,(w_x + u_z)\, \eta_x - \mu\,(w_y + v_z)\, \eta_y + 2\mu w_z &= 0
\end{aligned} \tag{3.18}$$

This set of dynamic boundary conditions is nonlinear and coupled by the unknowns of u, v, w, p, and η. They are to be satisfied on the $z = \eta$ surface.

Lastly, the body boundary condition for the fully nonlinear problem states that the velocity of the fluid is equal to the velocity of the body.

$$\vec{U} = \vec{U}_{\text{body}} \tag{3.19}$$

The boundary conditions for the fully nonlinear ship maneuvering problem have been presented. A free-surface assumption is made initially, and the implications of this are shown in Chapter V with a viscous-interface study.

3.3 Linearized Free-Surface Boundary Conditions

With the goal of linearization, the free-surface boundary conditions need to be expressed in a form which is able to be satisfied on the $z = 0$ plane. This problem is studied extensively within a velocity potential framework. Ship waves generated in calm water described with the velocity potential variable by Kelvin (1887) lay the

foundation for decades of additional work. Continuous functions describe ship waves for large domains as discussed in Noblesse et al. (2013, 2011). These show robustness and efficiency of applying a linearized free-surface approximation. Additional work extends to ship motions in the presence of incident waves (Beck and Loken, 1989; Salvesen et al., 1970) as well as waves described in an inertial reference frame (Noblesse and Yang, 2007). Comparisons of a linear approximation as apposed to a nonlinear free-surface are also considered with velocity potential (Havelock, 1937, 1940). This inviscid approach is shown to provide solutions to very complex problems such as dredging in a shallow water channel in Beck et al. (1975). Overall, the linearized free-surface boundary conditions alone are not new. However, exploring the suitability of a linearized free-surface in conjunction with a viscous, turbulent fluid is a unique endeavor; one that is important for the viscous, unsteady problem of ship maneuvering.

For this work, it is assumed that the waves associated with ship maneuvering are predominantly of small height and small slope. Thus, a first-order wave approximation will suffice while ignoring nonlinear and breaking waves. To display this mathematically, the free-surface conditions must first be made dimensionless to evaluate the relative values of each term. Quantitatively, the small slope assumption implies that $\mid \eta_x \mid, \mid \eta_y \mid \ll 1$. What follows is a process for linearization which one may pursue stemming from this assumption, as well as further inviscid assumptions within the dynamic condition resulting in wave effects that are solvable on the $z = 0$ plane.

Beginning again with the fully nonlinear kinematic free-surface boundary condition shown in Equation 3.7, one can consider a fluid moving past a floating body. From the perspective of a body-fixed observer, the horizontal components of the fluid

velocity vector can be decomposed into a mean and perturbing component:

$$\begin{aligned} u &= U + u^* \\ v &= V + v^* \\ w &= W + w^* \end{aligned} \tag{3.20}$$

The mean components are represented with U, V, and W, while the perturbation velocities are denoted with u^*, v^*, and w^*. For a forward speed ship resistance test, the mean velocity may simply be the mean surge velocity with respect to time, but a mean velocity is more difficult to define for a transient maneuver. Using decomposed velocities from Equation 3.20 in the fully nonlinear kinematic condition from Equation 3.7 results in the following modified nonlinear kinematic condition:

$$W + w^* = \eta_t + (U + u^*)\,\eta_x + (V + v^*)\,\eta_y \tag{3.21}$$

In order to determine the relative magnitude of each term in Equation 3.21, each quantity is represented non-dimensionally with U, L, and T. U is some suitable velocity scale, possibly the ship speed; L is the ship length or possibly a wave length;

and T is a time scale, perhaps a wave period. Each quantity is made dimensionless:

$$\begin{aligned}
\widetilde{W} &= \frac{W}{U} & \widetilde{w^*} &= \frac{w^*}{U} & \tilde{t} &= \frac{t}{T} \\
\widetilde{U} &= \frac{U}{U} = 1 & \widetilde{u^*} &= \frac{u^*}{U} & \tilde{\eta} &= \frac{\eta}{L} \\
\widetilde{V} &= \frac{V}{U} & \widetilde{v^*} &= \frac{v^*}{U} & \tilde{x} &= \frac{x}{L} \\
\tilde{\eta}_{\tilde{x}} &= \frac{L}{L}\eta_x = \eta_x & \tilde{\eta}_{\tilde{y}} &= \eta_y & \tilde{y} &= \frac{y}{L} \\
& & \tilde{\eta}_{\tilde{t}} &= \frac{T}{L}\eta_t
\end{aligned} \tag{3.22}$$

Assuming perturbation velocities, wave slopes, and wave heights are on the order of some small value, $\mathcal{O}(\epsilon)$, an order-or-magnitude analysis is performed. Substituting the values from Equation 3.22 into the fully nonlinear condition of Equation 3.21 and dividing by U gives the dimensionless equation:

$$\begin{array}{cccccc}
\widetilde{W} & +\widetilde{w^*} & = \dfrac{L}{UT}\tilde{\eta}_{\tilde{t}} & +\widetilde{U}\tilde{\eta}_{\tilde{x}} & +\widetilde{u^*}\tilde{\eta}_{\tilde{x}} & +\widetilde{V}\tilde{\eta}_{\tilde{y}} \quad +\widetilde{v^*}\tilde{\eta}_{\tilde{y}} \\
\mathcal{O}(\epsilon) & & = \mathcal{O}(\epsilon) & +\mathcal{O}(\epsilon) & +\mathcal{O}(\epsilon^2) & +\mathcal{O}(\epsilon) \quad +\mathcal{O}(\epsilon^2)
\end{array} \tag{3.23}$$

Only horizontal motions are performed with the linearized URANS method. As such, there is no mean vertical velocity, $\widetilde{W} = 0$. Furthermore, higher order terms, $\mathcal{O}(\epsilon^2)$, are very small and neglected resulting in the linear kinematic free-surface boundary condition, shown dimensionally:

$$w = \eta_t + U\eta_x + V\eta_y \tag{3.24}$$

The magnitude of the mean velocities depends on the frame of reference in which the maneuvering problem is described. For a forward speed resistance problem rep-

resented in a ship-fixed reference frame, $U = U_{\text{ship}}$ and $V = V_{\text{ship}} = 0$. Thus, the kinematic free-surface boundary condition in this ship-fixed description is reduced to a linearized form:

$$w = \eta_t + U\eta_x \tag{3.25}$$

In an earth-fixed frame of reference, calm water has a zero mean velocity, $U = V = 0$. Only perturbation velocities exist as the hull disturbs the calm water. Again, these are deemed small, and the linear kinematic free-surface boundary condition in an Earth-fixed frame of reference is obtained. It is known as the zero-speed kinematic condition:

$$w = \eta_t \tag{3.26}$$

A slightly different approach needs to be taken for the dynamic free-surface boundary conditions in Equation 3.18. The wave slope and wave height are considered small, but less can be said about the velocity gradients on the surface of the water. As a starting point, one can again select velocity and length scales with which to characterize the problem. Commonly with ship flows, the ship speed and ship length are chosen for these scales. As such, the non-dimensional Reynolds and Froude numbers are used, respectively,

$$Re = \frac{UL}{\nu} = \frac{UL\rho}{\mu} \tag{3.27}$$

$$Fr = \frac{U}{\sqrt{gL}} \tag{3.28}$$

where U is the speed of the ship, L is the length of the ship, ν is the kinematic viscosity, ρ is the water density, and g is the magnitude of gravity. In addition to the use of Reynolds and Froude numbers for viscous and gravitational terms, each

remaining term in Equation 3.18 can be represented non-dimensionally:

$$\tilde{p} = \frac{p}{\frac{1}{2}\rho U^2}$$
$$\tilde{\eta} = \frac{\eta}{L}$$
$$\widetilde{\nabla \vec{U}}_{\mathrm{ij}} = \frac{\nabla \vec{U}_{\mathrm{ij}}}{U/L}$$

The ship speed and length are suitable quantities for non-dimensionalizing the gravity waves which govern the hull forces. After all, the fundamental wavelength, λ, of ship generated waves in deep water is defined using these quantities:

$$\frac{\lambda}{L} = \frac{2\pi U^2}{gL} \tag{3.29}$$

However, these scales are not representative of the boundary layer flow near the hull. To some extent, this boundary layer interacts with the water surface, so caution must be used when using the ship length, L, as the length scale for dimensionless analysis with this viscous problem. Applying this non-dimensional analysis to the nonlinear dynamic conditions, and dividing by $\frac{1}{2}\rho U^2$, offers insight into the possible significance of each term with following the dimensionless equations:

$$\begin{aligned}
\left(\tilde{p} - 2Fr^{-2}\tilde{\eta}\right)\tilde{\eta}_{\tilde{x}} - 4Re^{-1}\tilde{u}_x\tilde{\eta}_{\tilde{x}} - 2Re^{-1}\left(\tilde{u}_y + \tilde{v}_x\right)\tilde{\eta}_{\tilde{y}} + 2Re^{-1}\left(\tilde{u}_z + \tilde{w}_x\right) &= 0 \\
\left(\tilde{p} - 2Fr^{-2}\tilde{\eta}\right)\tilde{\eta}_{\tilde{y}} - 2Re^{-1}\left(\tilde{v}_x + \tilde{u}_y\right)\tilde{\eta}_{\tilde{x}} - 4Re^{-1}\tilde{v}_y\tilde{\eta}_{\tilde{y}} + 2Re^{-1}\left(\tilde{v}_z + \tilde{w}_y\right) &= 0 \\
-\left(\tilde{p} - 2Fr^{-2}\tilde{\eta}\right) - 2Re^{-1}\left(\tilde{w}_x + \tilde{u}_z\right)\tilde{\eta}_{\tilde{x}} - 2Re^{-1}\left(\tilde{w}_y + \tilde{v}_z\right)\tilde{\eta}_{\tilde{y}} + 4Re^{-1}\tilde{w}_z &= 0
\end{aligned} \tag{3.30}$$

Again, the boundary layer presents ambiguity in determining the relative magnitudes of each quantity in Equation 3.30 because the velocity gradients may be large, and the length and velocity scales differ significantly from those used to describe the ship generated waves. If one assumes small velocity gradients in addition to the small wave slopes, the products of the two are negligible or $\mathcal{O}\left(\epsilon^2\right)$. This assumption produces

dynamic conditions which are linear:

$$\begin{aligned} 2Re^{-1}\left(\tilde{u}_z + \tilde{w}_x\right) &= 0 \\ 2Re^{-1}\left(\tilde{v}_z + \tilde{w}_y\right) &= 0 \\ -\left(\tilde{p} - 2Fr^{-2}\tilde{\eta}\right) + 4Re^{-1}\tilde{w}_z &= 0 \end{aligned} \tag{3.31}$$

Furthermore, Reynolds numbers are generally large for ship flows, resulting in small viscous terms in Equation 3.31. Neglecting all viscous terms in the dynamic condition results in a single, zero total pressure condition.

$$\tilde{p} - 2Fr^{-2}\tilde{\eta} = 0 \tag{3.32}$$

However, the assumption of large Reynolds number raises questions. Indeed, typical Reynolds numbers are at least $\mathcal{O}\left(10^5\right)$ for model scale. But these scales may not be an appropriate description for maneuvering flows. Certainly, the turbulent flow in the wake region aft of the transom contains length and velocity scales that are much shorter and slower than outside of the wake. Therefore, smaller lengths scales may be a more suitable representation of the flow in this region.

A variety of work has been conducted using different forms of the dynamic boundary conditions. Studies by Shen et al. (1999, 2000, 2002) implement the viscous linearized boundary conditions (Equation 3.31) for investigating the flow in the wake of a towed ship model. The model Reynolds and Froude numbers are $\mathcal{O}\left(10^3\right)$ and $\mathcal{O}\left(10^{-2}\right)$, respectively, and the beam is only four centimeters (Shen et al., 2002). It is found that the x and y components of the dynamic condition are very small at the water surface, but also that the wakes of real ships contain significantly more turbulence. Work by Rosemurgy et al. (2012) shows good results for free-surface flows using the inviscid, zero total pressure condition (Equation 3.32). Reynolds numbers for this work are $\mathcal{O}\left(10^5\right)$, but submerged bodies are studied in a steady manner. In

addition, Hong and Walker (2000) investigate free-surface flows with submerged jets. The jet diameter Reynolds number is $\mathcal{O}(10^4)$, and the Froude number is $\mathcal{O}(10^1)$. Viscosity is deemed negligible due to the high Reynolds number, but the absence of no-slip boundary conditions also influences this assumption.

The various problems, approaches, and conclusions in previous work prompts the need for a unique set of studies to determine the effect of viscosity and vorticity at the air-water interface of maneuvering flows. The goal of the present work is to extend the investigation of free-surface flows to large Reynolds and Froude numbers. In order to perform a thorough investigation, the entire fully nonlinear dynamic conditions from Equation 3.30 are studied. No *a priori* assumptions are made about the wave slopes, the velocity gradients, or eddy viscosity. This allows for a quantitative examination of the importance of each term in the zero total stress condition. The geometry used for this problem is that of a two-dimensional ship transom and is presented in Chapter V.

CHAPTER IV

Linearized Free-Surface Solver

4.1 ALE Formulation

The equations that govern the free-surface elevation are linearized, i.e. first-order kinematic and dynamic boundary conditions that are solved on the $z = 0$ plane.

$$w = \frac{\partial \eta}{\partial t} \tag{4.1}$$

$$p - \rho g \eta = 0 \tag{4.2}$$

Due to the linearization, the computational domain where the momentum equations are solved does not extend above the $z = 0$ calm-water plane. Body exact ship motions are limited to surge, sway, and yaw. These horizontal-plane motions are performed in an inertial, Earth-fixed reference frame that necessitates an arbitrary Lagrangian-Eulerian (ALE) formulation of the governing equations. Equations are solved for each computational cell that has volume V and is bounded by the surface S with outward normal $\hat{n}$. $S_o(t)$ is the portion of the boundary of a computational cell that is adjacent to the $z = 0$ plane, and $l(t)$ is the contour of this area. The development of the ALE form of the kinematic free-surface boundary condition begins

with the Leibniz integral rule applied over a surface to the right-hand side of Eq. 4.1,

$$\frac{\partial}{\partial t}\int\limits_{S_o(t)} \eta \; dS = \int\limits_{S_o(t)} \frac{\partial \eta}{\partial t} \; dS + \int\limits_{l(t)} \eta \frac{\partial \vec{x}_{\text{mesh}}\,(t)}{\partial t} \cdot \hat{n} \; dl \tag{4.3}$$

where,

$$\frac{\partial \vec{x}_{\text{mesh}}\,(t)}{\partial t} = \vec{U}_{\text{mesh}} = u_{\text{mesh}}\hat{i} + v_{\text{mesh}}\hat{j} + 0\hat{k} \tag{4.4}$$

Equation 4.3 can be modified to appear as:

$$\int\limits_{S_o(t)} \frac{\partial \eta}{\partial t} \; dS = \frac{\partial}{\partial t}\int\limits_{S_o(t)} \eta \; dS - \int\limits_{l(t)} \eta \vec{U}_{\text{mesh}} \cdot \hat{n} \; dl \tag{4.5}$$

With this, one can see that the mesh motion gives rise to a convective term in the ALE formulation of the kinematic free-surface boundary condition. And the form of the condition solved is:

$$\frac{\partial}{\partial t}\int\limits_{S_o(t)} \eta \; dS - \int\limits_{l(t)} \eta \vec{U}_{\text{mesh}} \cdot \hat{n} \; dl = \int\limits_{S_o(t)} w \; dS \tag{4.6}$$

Similarly, the ALE form of the momentum and continuity equations is solved,

$$\frac{\partial}{\partial t}\int\limits_{V} \rho \vec{U} \; dV + \int\limits_{S} \rho \vec{U} \vec{U}_{\text{rel}} \cdot \hat{n} \; dS = -\int\limits_{S} \bar{p} \cdot \hat{n} \; dS + \int\limits_{S} \mu_{\text{eff}} \left(\nabla \vec{U} + \nabla \vec{U}^T \right) \cdot \hat{n} \; dS \tag{4.7}$$

$$\int\limits_{S} \vec{U}_{\text{rel}} \cdot \hat{n} \; dS = 0 \tag{4.8}$$

where,

$$\vec{U}_{\text{rel}} = \vec{U} - \vec{U}_{\text{mesh}} \tag{4.9}$$

and the effective viscosity is the sum of the molecular and turbulent viscosities, $\mu_{\text{eff}} = \mu + \mu_t$.

4.2 Boundary Condition at Free-Surface/Body Juncture

In physical settings and nonlinear simulations of ship maneuvering, the height of the water level varies along the hull. If using a VOF method, a macroscopic boundary condition for the phase indicator variable, α, on the hull is a Neumann condition where the gradient of α is zero in the direction of the normal vector on the body:

$$\nabla\alpha \cdot \hat{n} = 0 \tag{4.10}$$

The zero-gradient condition allows bow waves to force water above the calm waterline and ventilated transom sterns to lower the surface to the depth of the transom. These phenomena raise challenges for the linearized free-surface method, especially near the transom. Since the free-surface elevation is calculated on a rigid $z = 0$ plane, the domain level around the hull never actually changes. Therefore, a unique boundary condition is required for the free-surface elevation on the body. Transom sterns that become ventilated during an unsteady simulation pose the greatest risk for divergence with the linearized URANS method. A zero-gradient condition is suitable on the majority of the hull, but a Dirichlet condition is useful in the transom region. A Dirichlet condition specifies the value of the free-surface elevation. As such, users may set the free-surface elevation to the depth of a ventilated transom. The capability to impose both Neumann and Dirichlet conditions on the hull is possible with the use of a Robin or mixed condition, in discretized form:

$$\eta = V_f\left(\eta_{\mathrm{bc}}\right) + \left(1 - V_f\right)\eta_p \tag{4.11}$$

V_f is the volume-fraction that dictates the blending of a fixed-value and zero-gradient in the condition. The volume-fraction can take values from $0 \leq V_f \leq 1$. A value of $V_f = 1$ makes the free-surface elevation on the body equal to a user-specified

fixed-value, η_{bc}. A value of $V_f = 0$ activates a zero-gradient (Neumann) condition which makes the free-surface elevation equal to the value at the center of the cell adjacent to the boundary, η_p. The value of V_f is computed with Equation 4.12:

$$V_f = C_m \left[max \left(0,\ \frac{1}{1 - C_t} \left(-\hat{n}_f \cdot \frac{\vec{U}_{\text{ship}}}{\mid \vec{U}_{\text{ship}} \mid} - C_t \right) \right) \right] \tag{4.12}$$

Here, U_{ship} is the velocity of the body, and $\hat{n}_f$ is the outward pointing normal of the body. The transition coefficient, C_t, is a user-specified value ranging from $0 \leq C_t < 1$ that helps determine the location where the boundary condition will transition from Neumann to Dirichlet. If the angle between the velocity vector of the body and the outward-pointing normal of the body is less than $\arccos(C_t)$, V_f will be set to zero, and the boundary condition will be fully zero-gradient (Neumann). However, if the angle between the velocity and outward-pointing normal is greater than $\arccos(C_t)$, the condition is partially fixed-value and zero-gradient. When the flow is aligned with the normal, $V_f = 1$, the condition becomes fully fixed-value (Dirichlet). C_m is a multiplication coefficient a user can change to further modify the boundary condition. This approach for the boundary condition for η at the free-surface/body juncture is very useful. A user can calculate the transom-based Froude number to determine if a transom stern is ventilated. Then the geometry of the hull can be considered along with the type of maneuvering test to set an angle with C_t at which the free-surface elevation will be fixed at a certain value (perhaps the depth of the transom).

As an example, a hull with an elliptic water-plane cross-section is considered. It translates purely in the $(+x)$-direction with some velocity, $u_{\text{ship}}\hat{i}$. Figure 4.1 shows the region on the hull where the boundary condition is mixed for several values of C_t. For this example, the free-surface elevation forward of midship is always governed by the Neumann, zero-gradient condition, where $V_f = 0$. Depending on the value of C_t, the condition becomes mixed at some point aft of midship. All instances of the

condition become Dirichlet-type at the stern where the outward pointing normal is aligned with the ship velocity.

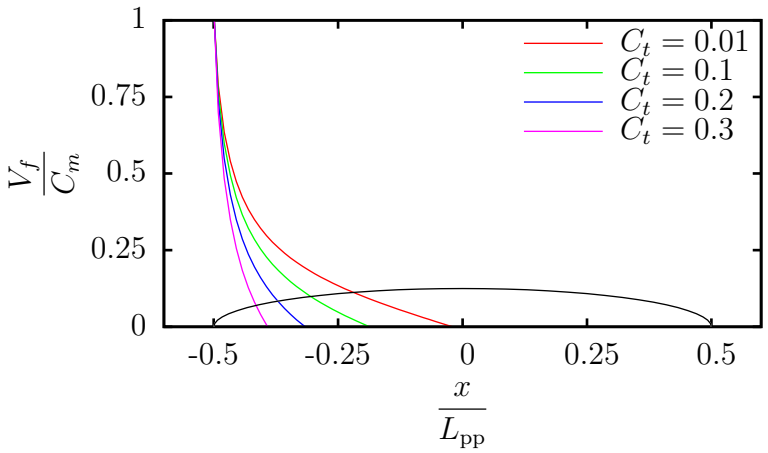

Figure 4.1: Free-surface body boundary condition with varying C_t values

4.3 Numerical Aspects

The linearized URANS method is a custom finite volume CFD algorithm based within the OpenFOAM C++ library. It consists of solutions to the URANS equations and a linear free-surface condition. At the free-surface, values for the wave elevation, η, are solved at cell centers and interpolated onto cell faces.

Results discussed in this paper are obtained on structured and unstructured grids. A PISO-like algorithm is used to solve for pressure and velocity. Time discretization is performed with a first-order Euler implicit scheme. A second-order linear upwind scheme is used for convective terms. The Spalart-Allmaras turbulence model is used with an adaptive wall function based on the Spalding universal law of the wall.

To simulate motions in the horizontal plane, the entire computational domain moves with rigid-body motion. The ship motion is described in an inertial, Earth-fixed reference frame. This approach allows for a natural description of the acceleration of the body from rest and avoids issues related to an impulsive start. Furthermore, it closely resembles the actual motions in a physical setting (which in this validation

is a towing tank). While the entire grid undergoes rigid body motion, propellers and rudders rotate relative to the body with a sliding-mesh approach. A cylinder enclosing a propeller or rudder rotates independently from the remainder of the mesh. Figure 4.2 describes the steps of the algorithm with the unique features outlined in red. The solution of the momentum equations provides the vertical velocity which is used in the kinematic boundary condition. In a typical segregated manner, the pressure equation is then solved and used to correct the velocities at cell centers. Upon updating the boundary conditions over the computational domain, the pressure condition on the free-surface uses the wave elevation from the kinematic condition to apply the hydrostatic pressure. Steady problems can be modeled by using time steps to dictate the number of iterations with no inner correctors, outer correctors, or time-derivatives. For unsteady problems, time steps can dynamically adjust to a user-defined Courant number restriction. For stability, inner correctors can be used to solve the momentum equations multiple times within a single time step. Lastly, under-relaxation may be employed in combination with outer correctors for time-accurate solutions employing large time steps.

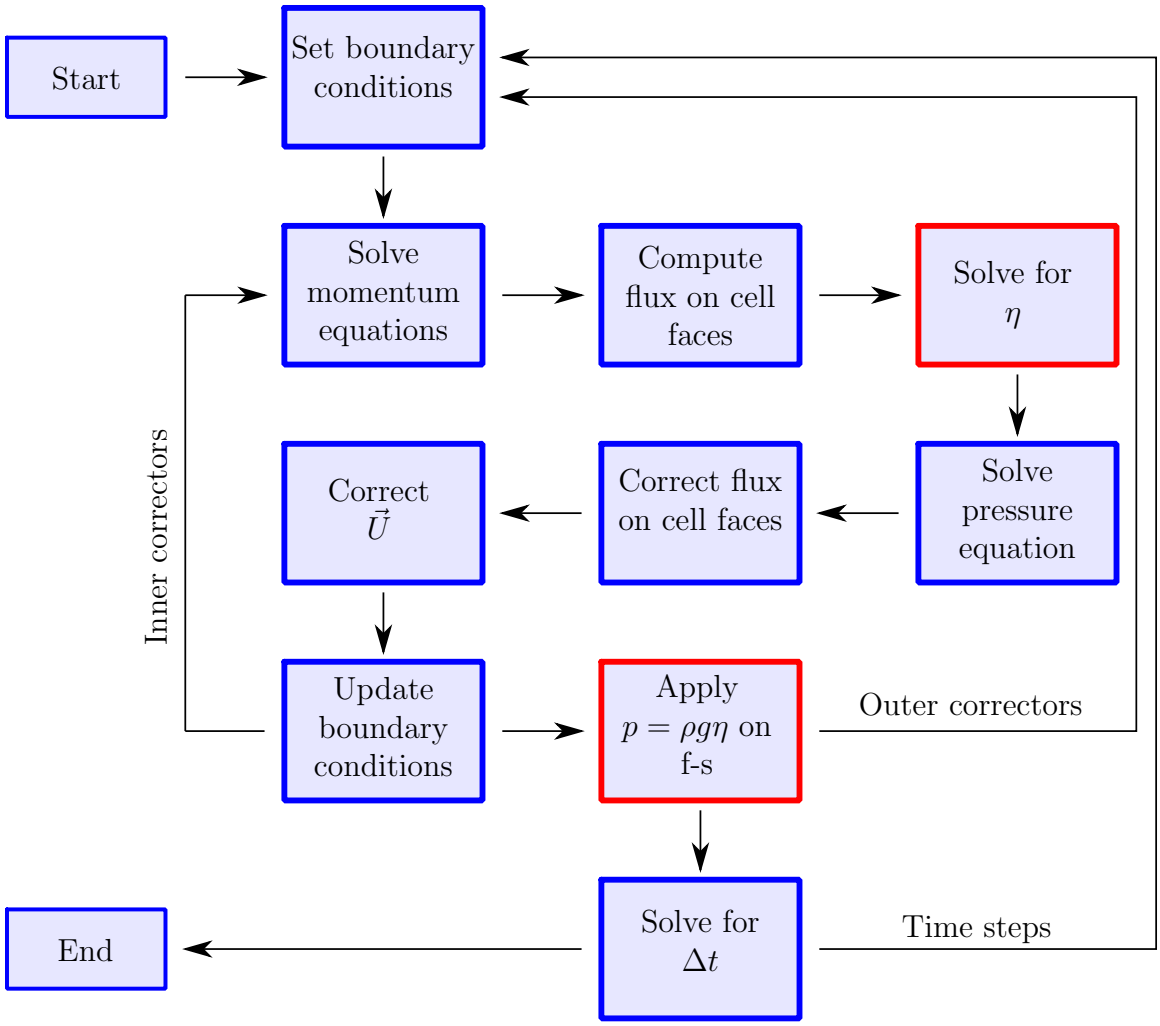

Figure 4.2: Steps of the linearized URANS algorithm

4.4 KCS Validation

As an initial validation of the linearized free-surface boundary conditions, the KRISO container ship (KCS) hull is studied at forward speed over a range of Froude numbers. Although the ultimate goal is maneuvering prediction, requiring the accurate solutions to forces and moments, this relatively simple study provides an opportunity to view the wave height along the hull as well as predictions of sinkage and trim. Vertical motions are not performed with the linearized RANS method, but the heave and pitch can be calculated with an approach consistent with linear theory using

Equations 4.13 and 4.14:

$$\text{Sinkage} = \frac{\mathrm{F_z}}{\rho \mathrm{g A_{wp}}} \tag{4.13}$$

$$\text{Trim} = \frac{\mathrm{M_y}}{\rho \mathrm{g I_{yy}}} \tag{4.14}$$

The net force is the vertical direction is denoted with F_z and the net moment of inertia about the pitch axis is M_y. The area of the waterplane is represented with A_{wp} and I_{yy} is the area moment of inertia about the pitch axis.

The KCS is $7.31m$ long, and is tested at five Froude numbers ranging from $Fr = 0.152 - 0.282$. The converged solution from $Fr = 0.26$ is shown in Figure 4.3 which is colored by the free-surface elevation. The grid contains approximately 430,000 cells. Due to the steady nature of the forward speed tests, the simulations are performed in a steady, ship-fixed frame of reference.

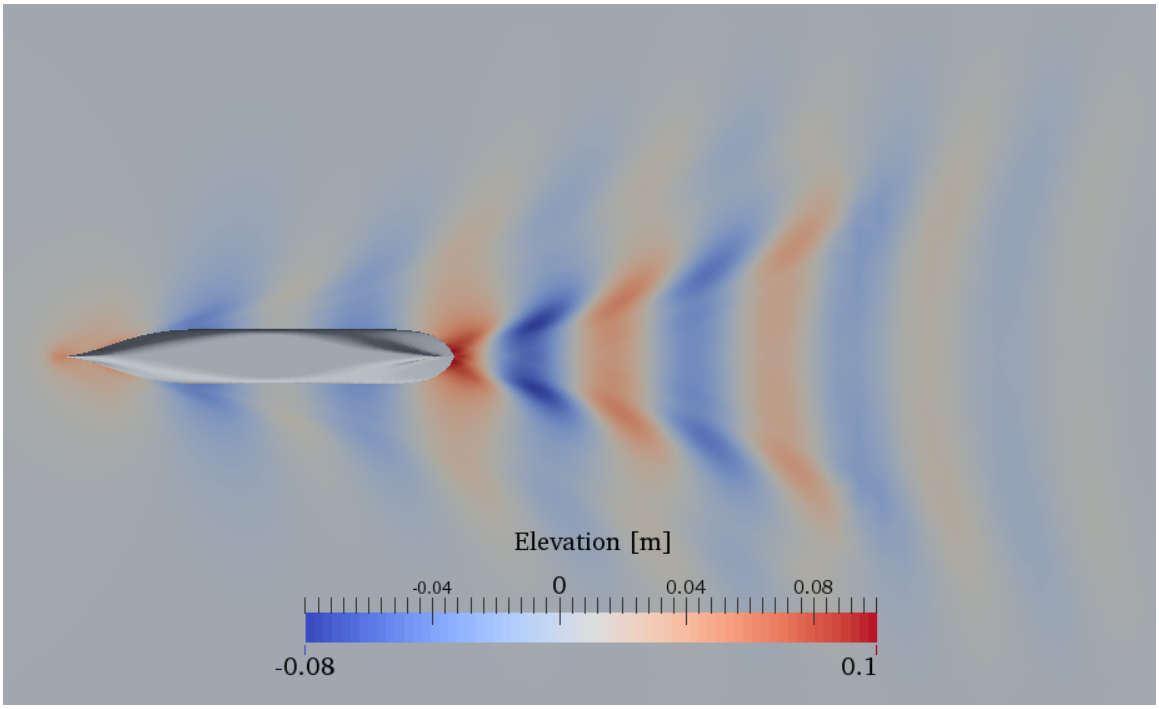

Figure 4.3: Free-surface elevation for KCS at $Fr = 0.26$

The calculated sinkage and trim are shown in Figure 4.4 along with the measured values from the experiments. The sinkage is predicted very well over the full range

of Froude numbers with the linearized RANS method. The largest discrepancy compared to the experimental data is approximately one millimeter occurring at the high and low Froude number limits. The trim angles agree well at the low Froude numbers, but show increasing differences at higher Froude numbers. However, the largest difference between the simulations and experiments is still roughly 0.1 degrees.

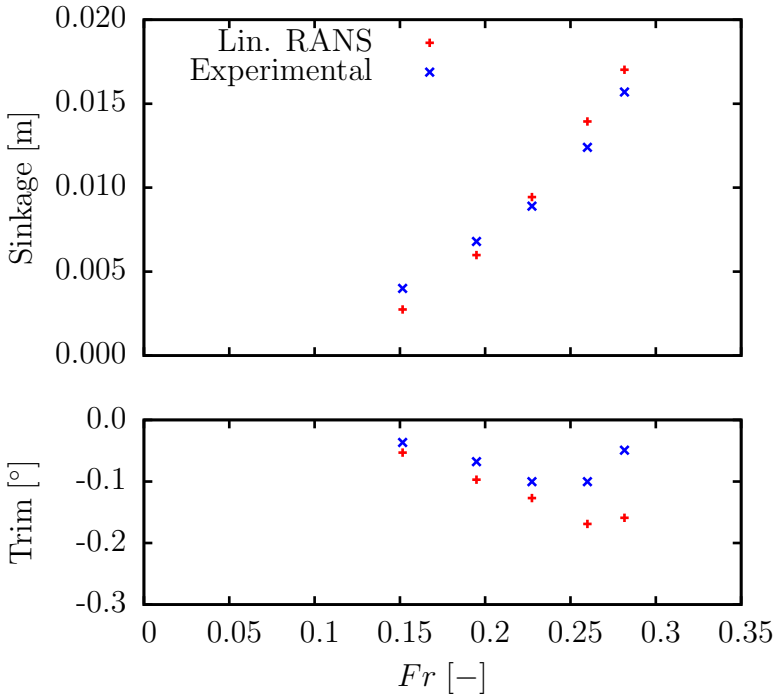

Figure 4.4: Sinkage (top) and trim (bottom) of KCS at various Froude numbers. Values are measured for the experiments and computed for the simulations

The wave elevation along the hull is presented in Figure 4.5 for Froude number $Fr = 0.26$. The linearized data agrees well along the majority of the hull. However, there is a noticeable under-prediction near the bow and an over-prediction at the stern. For this study, a zero normal-gradient condition is used for the free-surface boundary condition at the free-surface/body juncture. In Section 4.2, a custom body boundary condition is presented which aids in mitigating the discrepancies that are possible to produce with a zero normal-gradient condition.

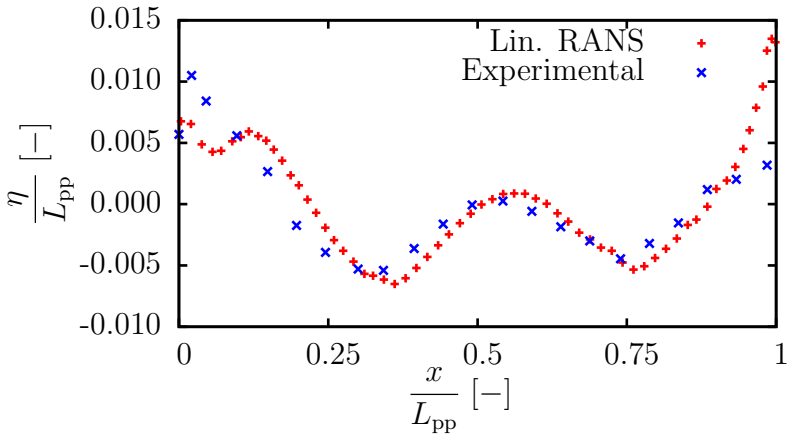

Figure 4.5: Wave along KCS hull at $Fr = 0.26$

CHAPTER V

Viscous Air-Water Interface Study

5.1 Canonical Viscous Interface Study

In order to quantify the relative importance of each term in the fully nonlinear dynamic free-surface boundary condition, a canonical study is performed with a two-dimensional transom stern geometry. An interface capturing approach is employed by using a fully nonlinear VOF method. This allows one to quantify the effects of reducing problems from an air-water interface to a free-surface, as well as the effects of linearization and the neglect of viscous terms. A diagram of the two-dimensional ship transom is shown in Figure 5.1.

The two-dimensional transom study is a challenging problem for the linear method. The entire domain is filled with water below the $z = 0$ calm-water plane. However, wave elevations oscillate some small value, η, about the flat free-surface. So, the linear approximation possesses an interesting feature - the conservation of mass and momentum is satisfied for a single phase in each computational cell, but the pressure within these cells can correspond to being filled with either water or air. For example, in the case of a ventilated transom stern, a trough of the wave is located at the bottom of the transom. The linearized method has computational cells above this trough, but the dynamic pressure within them corresponds to the hydrostatic pressure at the base.

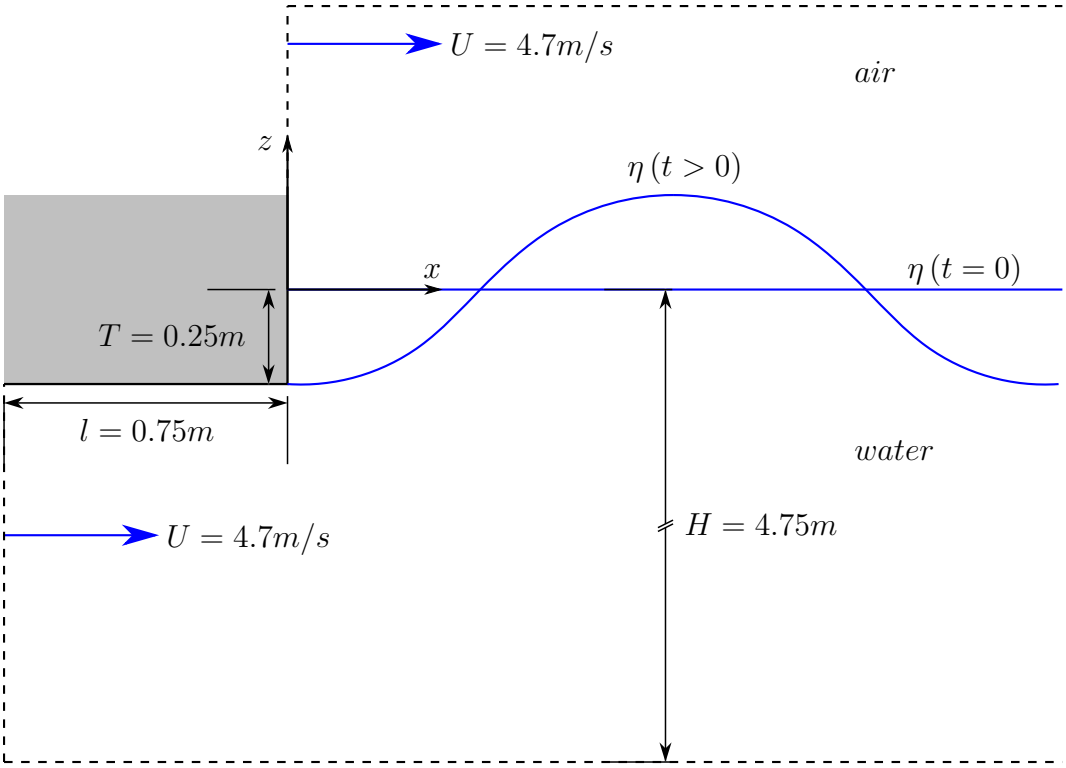

Figure 5.1: Two-dimensional canonical transom stern geometry

5.1.1 VOF Numerical Method

This multiphase interface study is performed with OpenFOAM which is an open source CFD software package. The standard collection of C++ libraries that comprise OpenFOAM consists of solvers for many partial differential equations governing a variety of physics. In addition, several turbulence models, linear system solvers, and discretization schemes can be selected to best suit the needs of a user. Modifications and additions to the software can be made for custom applications. OpenFOAM employs the finite-volume method (FVM), calculating the value of field (non-boundary) variables at the center of computational cells. For details of the FVM applied to fluid flows see Jasak (1996).

Due to the FVM approach, the two-dimensional transom study is conducted on a three-dimensional grid that has a single cell extruded in the y-direction. The incom-

pressible URANS equations are solved in both air and water:

$$\frac{\partial \rho \vec{U}}{\partial t} + \nabla \cdot \rho \vec{U}\vec{U} = -\nabla p + \nabla \cdot \left[(\mu + \mu_\tau) \left(\nabla \vec{U} + \nabla \vec{U}^T \right) \right] \tag{5.1}$$

$$\nabla \cdot \vec{U} = 0 \tag{5.2}$$

The dynamic eddy viscosity is represented with μ_τ and arises due to modeling the fluctuating components after Reynolds-averaging. The solution to μ_τ is obtained using the one-equation Spalart-Allmaras turbulence model (Spalart and Allmaras, 1992). The pressure-velocity coupling is handled in a segregated manner where these variables are decoupled and solved implicitly. For a thorough description of this approach see Barton (1998) and Issa (1986).

The air-water interface is captured using a VOF method. This technique is well suited for large deformations between fluids with significant differences in density (Hirt and Nichols, 1981; Lafaurie et al., 1994). Two fluids are treated as one continuous fluid composed of two regions with different properties of density and viscosity:

$$\rho(\vec{x}, t) = \rho_{\text{water}} \alpha(\vec{x}, t) + \rho_{\text{air}} (1 - \alpha(\vec{x}, t)) \tag{5.3}$$

$$\mu(\vec{x}, t) = \mu_{\text{water}} \alpha(\vec{x}, t) + \mu_{\text{air}} (1 - \alpha(\vec{x}, t)) \tag{5.4}$$

The locations of the air and water regions are determined by the value of the phase-indicator variable, α, which varies from zero to one throughout the domain. Cells occupied by water have a value of $\alpha = 1$, and cells occupied by air have a value of $\alpha = 0$. The interface is not sharp but rather smeared across multiple cells. Those cells at the interface have values of $0 < \alpha < 1$. The solution to the phase-indicator variable is governed by an advection equation,

$$\frac{\partial \alpha}{\partial t} + \nabla \cdot \left(\alpha \vec{U} \right) + \nabla \cdot \left(\alpha (1 - \alpha) \vec{U}_r C_\alpha \right) = 0 \tag{5.5}$$

where $\vec{U}_r$ is a compression velocity which acts normal to and towards the interface. It helps regulate the smearing of the interface, and it is only active where $0 < \alpha < 1$. The coefficient C_α allows a relative magnitude of the compression velocity to be applied. For this study, the value of C_α is constant, $C_\alpha = 1$

Time discretization is performed with a first-order implicit Euler scheme. Integration over faces is done with a second-order midpoint rule. Lastly, the divergence operator is discretized with a second-order upwind-biased scheme for velocity and a van Leer limited scheme for the phase indicator variable. The equation for the phase indicator variable is solved in an explicit manner. The linear systems of equations are solved with a generalized geometric-algebraic multi-grid (GAMG) solver.

5.1.2 Description of Canonical Problem

The purpose of these studies is to determine the dominant terms that govern the pressure at the water surface of an air-water interface. In particular, the effects of viscosity and velocity gradients are of interest in order to reach a clear conclusion of which terms to include when choosing a pressure boundary condition for the linearized URANS method. Due to the unsteady nature of maneuvering, a variety of flow is produced. Breaking waves, non-breaking waves, large areas of recirculation, and relatively calm water can all be witnessed. To account the for range of phenomena, nine combinations of Reynolds numbers and transom-based Froude numbers are tested as shown in Table 5.1. The transom-based Froude number is defined in Equation 5.6. For each simulation, the initial values of the kinematic eddy viscosity, ν_τ, on the inlet are equal to the molecular kinematic viscosities shown in Table 5.1.

Table 5.1: Two-dimensional transom test viscosity and gravity variable values

Re	ν [m^2/s]
$1e4$	$3.52e-4$
$1e5$	$3.52e-5$
$1e6$	$3.52e-6$

Fr_T	g [m/s^2]
3	9.81
2	22.1
0.2	2207

$$Fr_T = \frac{U}{\sqrt{gT}} \tag{5.6}$$

The work of Maki (2006) studies transom stern hydrodynamics and discusses the highly unsteady nature of the flow at particular Froude numbers. This is useful for choosing the transom-based Froude numbers for the numerical experiments at hand. A Froude number of $Fr_T = 3$ produces a steady wave, $Fr_T = 2$ produces an unsteady breaking wave, and $Fr_T = 0.2$ produces a recirculation region with a nearly flat air-water interface. Therefore, these Froude numbers display flows which commonly occur near ship hulls during maneuvering.

The main reason behind changing the values of gravity and viscosity is to use the same grid for each test. Since velocity, U, is a shared variable between the Reynolds and Froude numbers, changing it requires new grids with subsequent changes of length, l, and draft, T. The current approach avoids this issue. However, changing the value of viscosity while not changing the grid spacing adjacent to the no-slip boundary condition presents issues with the dimensionless wall distance, y^+:

$$y^+ \equiv \sqrt{\frac{\tau_w}{\rho\nu^2}} \tag{5.7}$$

$$\tau_w = \mu \left(\frac{\partial u}{\partial z}\right)_{\text{wall}} \tag{5.8}$$

The wall shear stress is denoted with τ_w and defined in Equation 5.8 using the coordinate system for these experiments. With low-Reynolds number turbulence models, the dimensionless wall distance is required to be $y^+ < 1$. To overcome this restriction, an adaptive wall function is used to account for the average y^+ values for these experiments which are within the range $0.1 < y^+_{\text{mean}} < 50$. Table 5.2 shows the mean and maximum y^+ values for each simulation.

Table 5.2: Two-dimensional transom test y^+ values

	$Fr_T = 3$		$Fr_T = 2$		$Fr_T = 0.2$	
Re	y^+_{mean}	y^+_{max}	y^+_{mean}	y^+_{max}	y^+_{mean}	y^+_{max}
$1e4$	1.49	2.46	1.87	4.16	0.71	2.31
$1e5$	5.41	8.38	5.13	9.28	3.29	7.49
$1e6$	30.13	97.39	33.27	105.42	18.21	41.48

The grid for the study is fully structured and consists of approximately 2.9M entirely orthogonal cells. The resolution of the grid in the interface region is of great importance due to the smearing of the interface over multiple cells with the VOF method. To minimize the distance over which the smearing occurs, the back face of the transom is discretized with 598 cells, each with a height of roughly $0.83mm$. Gradual stretching is employed from the bottom and back faces of the transom. A qualitative representation of the grid appears in Figure 5.2.

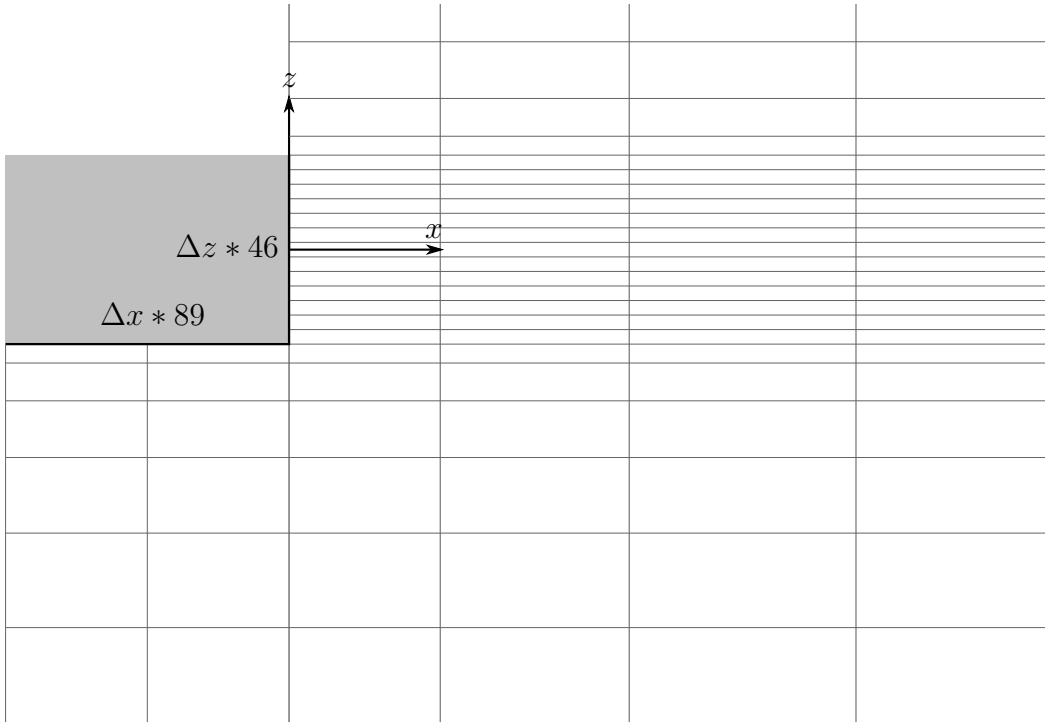

Figure 5.2: Transom grid characteristics. Cell dimensions adjacent to the transom are scaled for visualization. The stretching away from the transom is not to scale and is only meant for a qualitative description.

5.2 Results

The results from the two-dimensional transom stern study are divided into three sections corresponding to the three Froude numbers tested. The goal of the experiments is the same for all cases – to measure the suitability of the linearized free-surface conditions for maneuvering prediction. As a starting point, it must be shown that indeed an interface condition is satisfied. Therefore, the total stress of each fluid at the air-water interface is a concern for this investigation:

$$\begin{aligned} \overline{\overline{\sigma}}_{\text{water,air}} \cdot \hat{n} &= \left[-\left(p - \rho_{\text{water,air}} g\eta\right) \overline{\overline{I}} + \overline{\overline{\tau}} \right] \cdot \hat{n} \\ &= \left[-\left(p - \rho_{\text{water,air}} g\eta\right) \overline{\overline{I}} + \mu_{\text{eff}_{\text{water,air}}} \left(\nabla \vec{U} + \left(\nabla \vec{U} \right)^T \right) \right] \cdot \hat{n} \end{aligned} \tag{5.9}$$

For each Froude number, the terms which make up the total stress tensor will be considered in slightly different ways to best describe the important flow characteristics at hand. The beginning of each section contains a brief description of the way in which the terms will be evaluated. First, the cases with $Fr_T = 3$ are presented. This Froude number produces a steady wave, so two-dimensional plots are used to convey results which show the air-water interface condition and the small role of viscosity in the free-surface condition. Next, the cases with $Fr_T = 2$ are presented. With these, an unsteady breaking wave is generated, so iso-surfaces are used to show the small values of viscous stress and the balance between hydrostatic and hydrodynamic pressure at different moments in time. Lastly, cases where $Fr_T = 0.2$ are the low Froude number regime, and two-dimensional plots are again used to analyze this steady set of data.

Within each Froude number, the tests appear in order of increasing Reynolds number ($Re = 1e4,\ 1e5$, and $1e6$). Turbulence modeling is performed with the Spalart-Allmaras turbulence model, so viscous terms are shown using the effective viscosity $\mu_{\text{eff}} = \mu + \mu_t$. The study is two-dimensional, thus only the variables corresponding to the x and z-directions are reported. Also, all pressure and stress

quantities are presented in non-dimensional form, normalized by $\frac{1}{2}\rho_{\text{water}}U^2$, unless otherwise noted. This is simply used as a stress scale that corresponds to the stagnation pressure at the calm-water elevation, or the largest possible dynamic pressure in the flow under the irrotational assumption. A tilde is used above terms to symbolize dimensionless quantities. The downstream distance is non-dimensionalized by the fundamental wave length, λ, which is calculated for each Froude number:

$$\lambda = 2\pi Fr_T^2 T \tag{5.10}$$

The cases of $Fr_T = 3$ and $Fr_T = 0.2$ include a study of the kinematic condition by plotting the nonlinear and linear forms, respectively:

$$w = u\eta_x \tag{5.11}$$

$$w = U\eta_x \tag{5.12}$$

The vertical velocity at the surface of the water is w. The horizontal velocity from the solution is u, and the linear constant velocity from the inlet is $U = 4.7m/s$. When presented, these quantities from the kinematic condition are normalized by U.

Lastly, each section concludes with a comparison of the canonical study computed with the linearized URANS method, and the suitability of transferring the boundary conditions from the $z = \eta$ to the $z = 0$ plane is discussed. The geometry and magnitudes of gravity of the linear simulations are equivalent to those of the nonlinear simulations. However, the mesh does not extend beyond the $z = 0$ plane, and it contains only 7,909 computational cells.

5.2.1 $\mathbf{Fr_T = 3}$ – Steady Wave

This section presents the results from the highest Froude number tested, $Fr_T = 3$. The wave length corresponding to this flow is $\lambda \approx 14.1m$. As such, the water depth corresponds to an intermediate-depth condition, but the boundary condition employed on the bottom of the domain is not impenetrable. Instead, it is a zero normal-gradient condition, $\frac{\partial \vec{U}}{\partial n}$. Therefore, bottom effects are not as significant as with a physical boundary at this depth. The stress balance interface condition is shown to be satisfied, and the linearized free-surface condition is shown to be a reasonable assumption for this flow. Due to the steady nature of the non-breaking wave, the common normal vector is expressed in terms of the wave elevation:

$$\hat{n} = \frac{-\eta_x \hat{i} + \hat{k}}{\sqrt{\eta_x^2 + 1}} \tag{5.13}$$

First, the wave profiles are shown. Next, the stress in each fluid is considered to ensure that the interface condition is satisfied:

$$\overline{\overline{\sigma}}_{\text{water}} \cdot \hat{n} - \overline{\overline{\sigma}}_{\text{air}} \cdot \hat{n} = \vec{0} \tag{5.14}$$

From here on, the air is no longer studied, but the suitability of the free-surface approximation is investigated by considering stress terms from the water only:

$$\overline{\overline{\sigma}} \cdot \hat{n} = \begin{bmatrix} \left(\tilde{p} - Fr^{-2}\tilde{\eta}\right)\eta_x & - & 2Re^{-1}\tilde{u}_x\eta_x + Re^{-1}\left(\tilde{u}_z + \tilde{w}_x\right) \\ -\left(\tilde{p} - Fr^{-2}\tilde{\eta}\right) & - & Re^{-1}\left(\tilde{w}_x + \tilde{u}_z\right)\eta_x + 2Re^{-1}\tilde{w}_z \end{bmatrix} \tag{5.15}$$

The horizontal and vertical components of the stress vector are discussed individually. The viscous terms from the rate-of-strain tensor are presented. For brevity, a conservative approach is taken where the magnitude of each term is calculated, and these are summed giving insight into the total effect that the viscous terms have on

the water surface:

$$\frac{\mid -2\mu_{\text{eff}} u_x \eta_x \mid + \mid \mu_{\text{eff}} \left(u_z + w_x\right) \mid}{0.5\rho_{\text{water}} U^2} \tag{5.16}$$

$$\frac{\mid -\mu_{\text{eff}} \left(w_x + u_z\right) \eta_x \mid + \mid 2\mu_{\text{eff}} w_z \mid}{0.5\rho_{\text{water}} U^2} \tag{5.17}$$

Lastly, the hydrodynamic and hydrostatic pressure are compared. Only the terms from the vertical component of the stress vector, p and $\rho g \eta$, are plotted as these are representative of the terms from the horizontal component, $p\eta_x$ and $\rho g \eta \eta_x$, which are simply scaled by the wave slope.

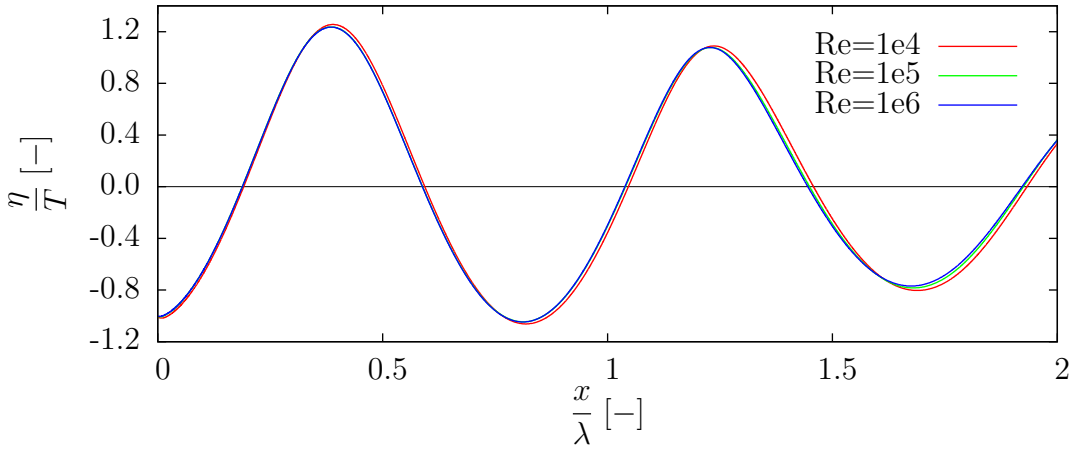

Figure 5.3: Wave elevations

The wave height for all the tested Reynolds numbers is shown in Figure 5.3. This is a steady wave that develops and remains for the duration of the simulation. One can see that the transom, with a depth of $T = 0.25m$, is fully ventilated under these conditions. The difference in Reynolds number results in no significant variation in the wave height.

The boundary layer profiles corresponding to each Reynolds number are presented in Figure 5.4. These are sampled one transom depth, T, forward from the transom edge. As expected, an increase in Reynolds number shows a thinning of the boundary layer thickness.

To investigate the accuracy with which the interface condition is satisfied, the

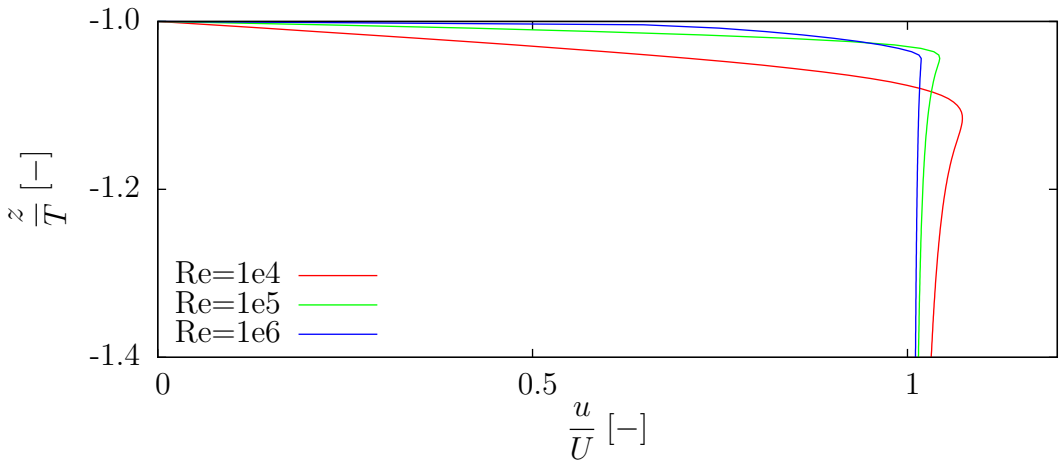

Figure 5.4: Boundary layer velocity profiles

modulus of the total stress vector dotted with the common unit normal, $\mid \overline{\overline{\sigma}} \cdot \hat{n} \mid$, is calculated for air and water. These magnitudes are plotted in Figure 5.5. To differentiate the two fluids, a contour of $\alpha = 0.99$ is used for water and $\alpha = 0.01$ for air. As such, the finite region that contains the interface is largely ignored. These phase-indicator variable restrictions are chosen as a conservative approach to identify stresses which very nearly correspond to either air or water rather than the unphysical slurry which is the interface calculated with the VOF method. It is because of this conservative approach that the stress in the water is not in balance with the stress in the air. Using a less rigorous approach, such as $\alpha = 0.55$ and $\alpha = 0.45$, produces a balance, but not from fluid that is strictly air or water. Still, referring to Figure 5.5, the magnitude of stress in the air is very small, being well below 1% of the of the chosen stress scale, $\frac{1}{2}\rho_{\text{water}}U^2$. The stress in the water is greater, but still less than 1% of the irrotational stagnation pressure.

Overall, the stress exhibited at the interface from each fluid is small, motivating the idea that a free-surface is a suitable approximation for this problem. Since water is the main fluid of concern, the small dynamic effects from the air are deemed negligible and the free-surface condition, $\overline{\overline{\sigma}}_{\text{water}} \cdot \hat{n} = \vec{0}$, governs the stress at the water surface. It is this condition that will now be studied to determine the dominant terms within

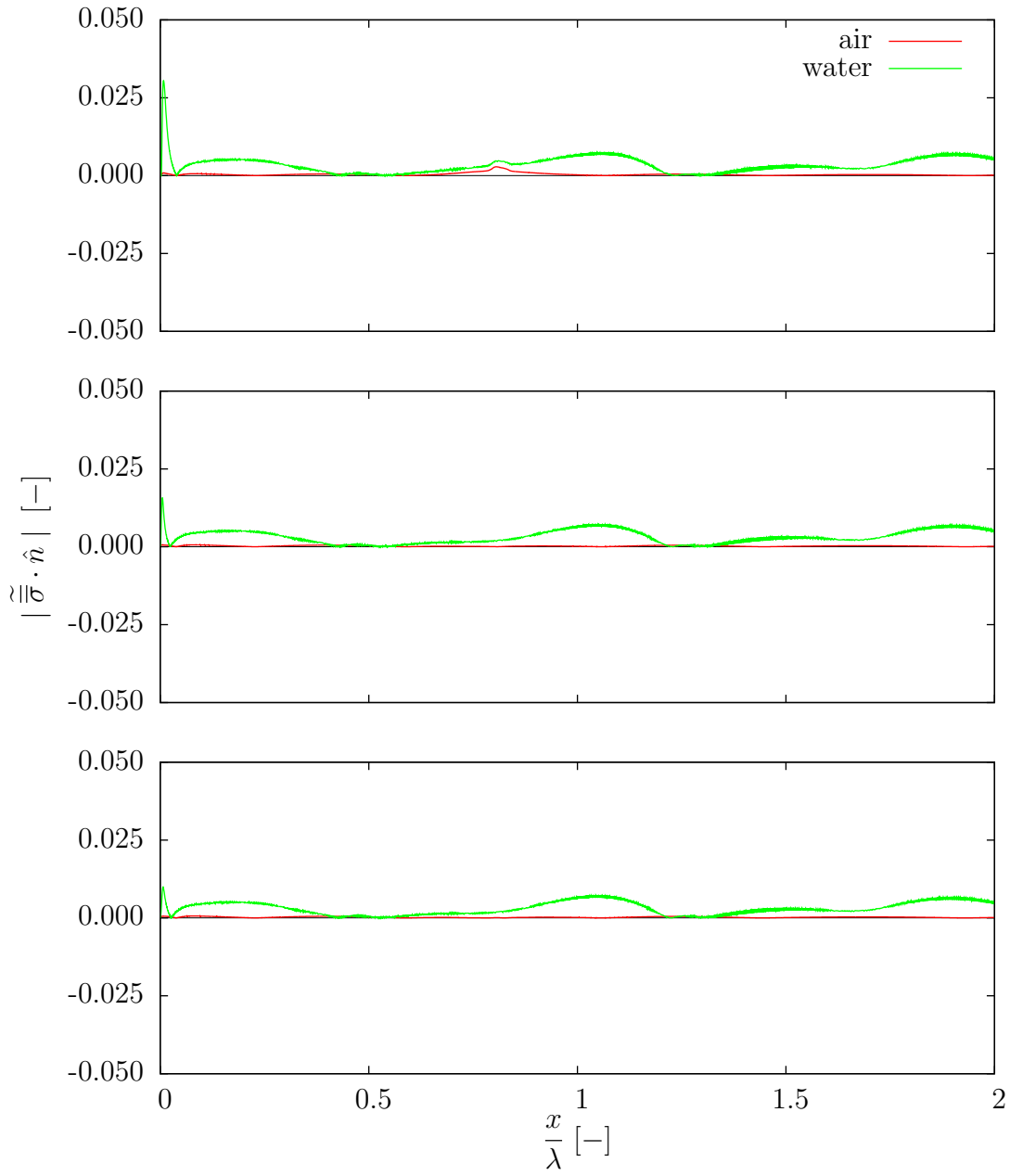

Figure 5.5: Stresses at air-water interface for Re=1e4 (top), Re=1e5 (middle), and Re=1e6 (bottom)

the total stress tensor, $\overline{\overline{\sigma}}_{\text{water}}$.

This study has successfully demonstrated that the dynamic effects from the air may be neglected, allowing for a free-surface approximation. As such, phase subscripts are removed, and all quantities refer to the water. The expansion of the total stress tensor dotted with the unit normal vector shows the quantities which govern the

stress of the water at the exact free-surface in Equation 5.15. The viscous terms from the horizontal and vertical components of the stress vector are plotted against the downstream position in Figure 5.6 and 5.7, respectively. As a conservative approach, the magnitudes of each term are summed. Indeed, these terms are measurable as seen from the nonzero values along the wave. However, the values are very small being less than 0.001% of the stagnation pressure. Dimensionally, this corresponds to less than one-tenth of a Pascal. As a reference, changes in pressure this small correspond to changes in depth of less than $0.01mm$ in water on Earth. Another notable observation is that the viscous terms scale linearly with Reynolds number which is evident by the fact that the variations in pressure from the viscous terms decrease by one order of magnitude with an increase in Reynolds number by one order of magnitude. Therefore, it may be concluded that the velocity gradients are not affected by changes in viscosity within this range of Reynolds numbers. Instead, the viscous terms simply scale due to the changes in μ_{eff}.

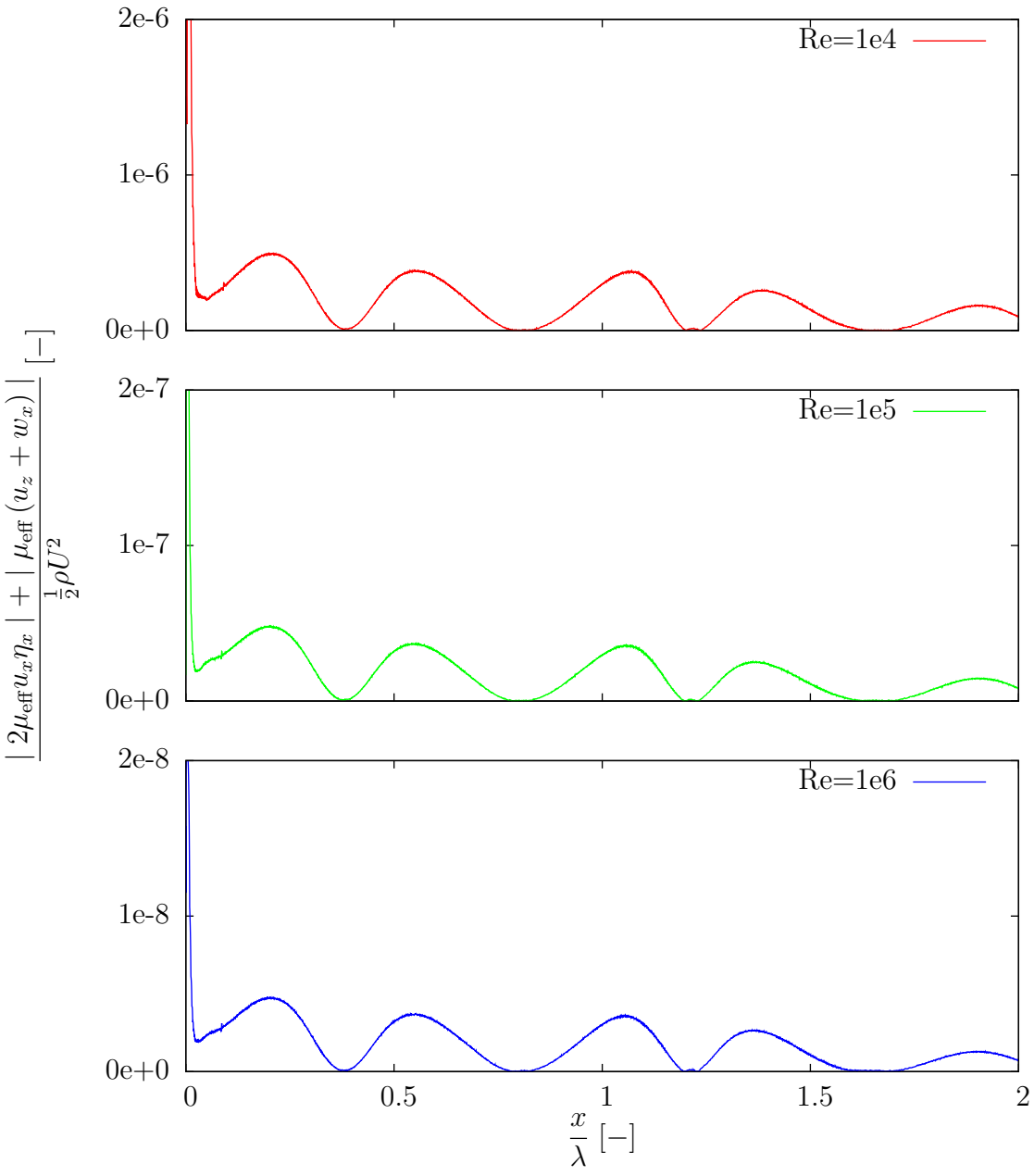

Figure 5.6: Magnitudes of horizontal viscous stresses at air-water interface

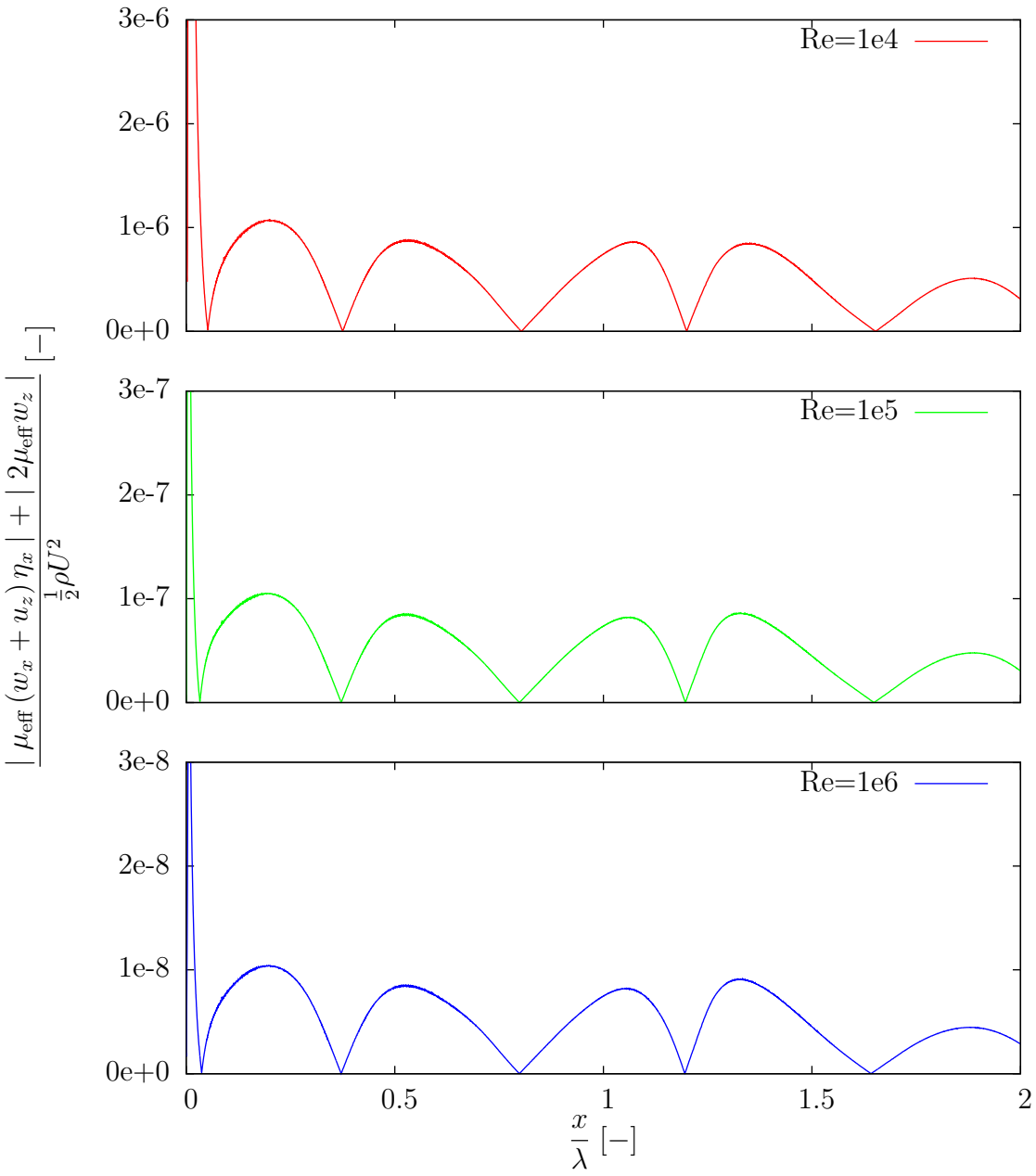

Figure 5.7: Magnitudes of vertical viscous stresses at air-water interface

With the insight that the viscous terms are very small in both the horizontal and vertical components of the stress vector, it is important to investigate the dynamic and hydrostatic pressure terms. These are shown for the vertical component of the stress vector in Figure 5.8. Compared to the viscous terms, the pressure terms are noticeably greater in value. They are at least $\mathcal{O}(10^5)$ times greater. Clearly, the pressure dominates at the water surface. The static and dynamic pressure in the

horizontal component of the stress vector are at most 10% of the vertical component, occurring where the wave slope is greatest, $\eta_x \approx 0.1$. It is also important to note that the dynamic pressure is nearly identical to the hydrostatic pressure. Not only does

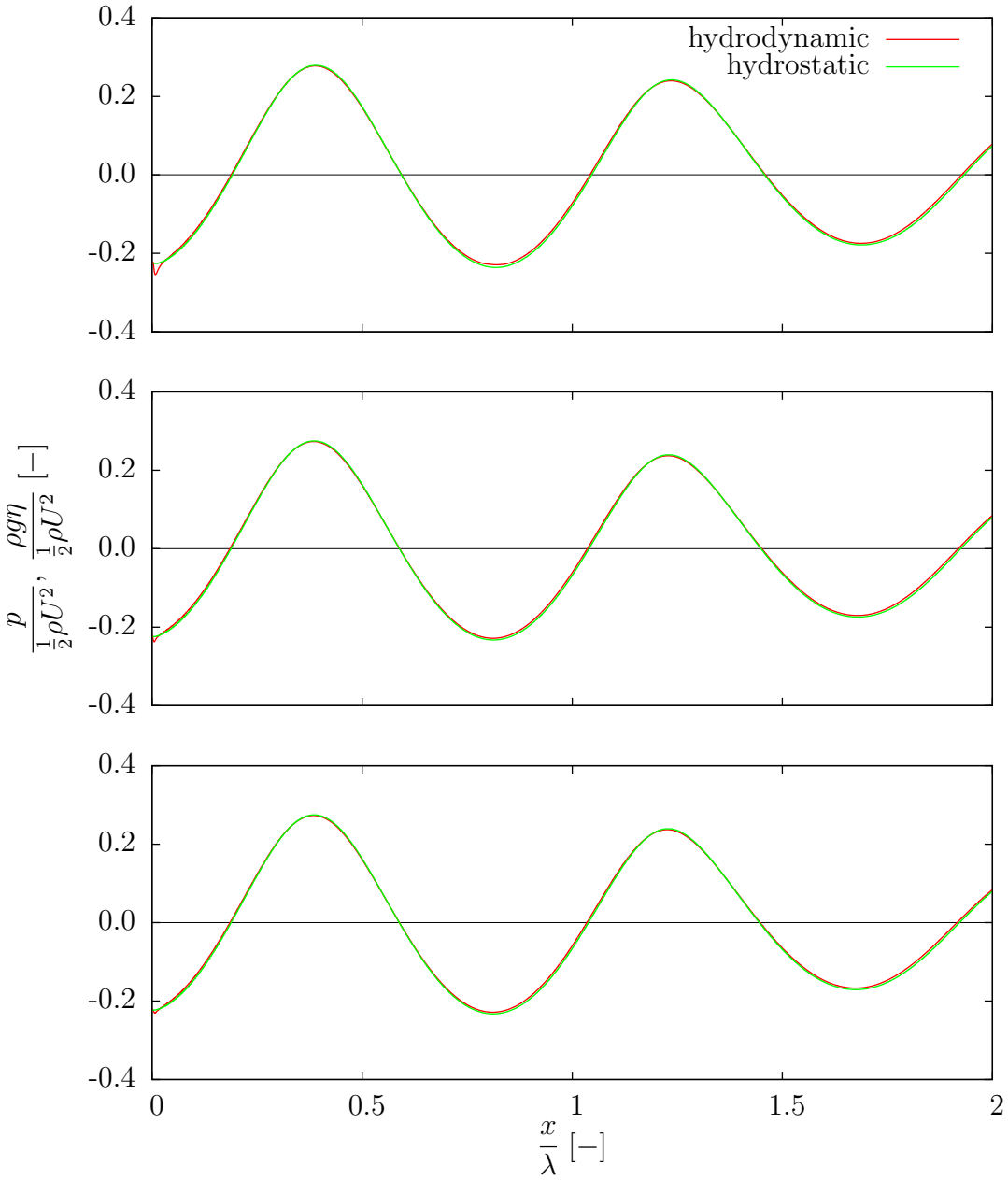

Figure 5.8: Hydrodynamic and hydrostatic pressure at water surface for Re=1e4 (top), Re=1e5 (middle), and Re=1e6 (bottom)

this coincide with the small viscous values previously discussed, but it also shows the validity of employing an inviscid, zero total pressure condition in the vertical

direction. Indeed, this is the boundary condition solved with the linearized URANS method:

$$p = \rho g \eta \tag{5.18}$$

Satisfying a pressure boundary condition on an exact free-surface requires the pressure from both the horizontal and vertical component of the stress vector. However, the linearized URANS method does not account for the horizontal component because the wave elevations are approximated on a flat free-surface with a normal vector continuously aligned with the z-axis. This approximation is valid for small wave heights that do not deviate far from the $z = 0$ calm-water surface. Figure 5.9, demonstrates this by comparing the wave elevations obtained with the VOF method as well as those obtained by replicating the experiment with the linearized URANS method. Only the results from the Reynolds number $Re = 1e4$ are compared. In addition, at the transom the linearized URANS method uses the free-surface elevation and pressure which coincide with the fully ventilated scenario, $\eta = -0.25m$ and $p = -2452.5Pa$. Due to the fixed-value pressure condition, a zero normal-gradient condition is imposed on velocity. However, the bottom, or keel, maintains a no-slip boundary condition. It is only the back face of the transom that requires special consideration with the linear method. Although the two methods do not compute wave elevations which are entirely agreeable, the results are qualitatively similar. Those computed on $z = 0$ show slightly lower values at both wave crests and troughs compared to the nonlinear results. There is also a difference in wave length, however the linear simulations show a length which is closer to the estimated value, $2\pi Fr_T^2 T \approx 14.1m$.

The comparison of nonlinear and linear kinematic free-surface boundary conditions appears in Figure 5.10. Each curve represents data from the VOF solution only and is normalized by U. The linear condition is computed with the constant inlet velocity, $U = 4.7m/s$, whereas the nonlinear condition uses the actual horizontal

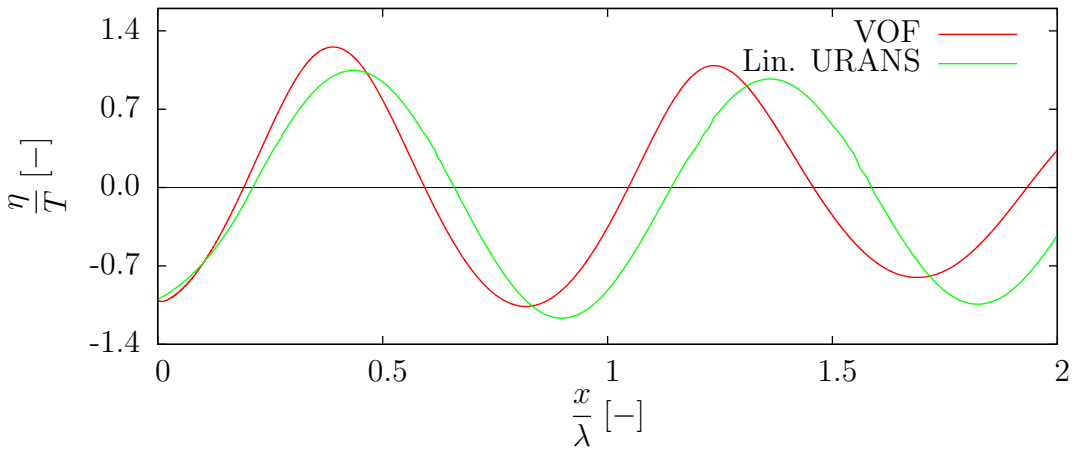

Figure 5.9: Wave elevations using VOF and linerized URANS for $Fr_T = 3$ and $Re = 1e4$

component of velocity, u, from the solution. Lastly, w is the actual vertical component of velocity. There is a slight difference between both conditions and the vertical velocity along the majority of the wave. This difference decreases downstream, and on the whole all three velocities are quite similar. Most importantly, the difference between the linear and nonlinear conditions is very small, demonstrating that the linear kinematic condition used with the linearized URANS method is suitable, in a body-fixed reference frame:

$$w = U\eta_x \tag{5.19}$$

It is interesting that the linear kinematic condition agrees well with the vertical velocity at the water surface. One may not expect this to be the case when a surface-piercing body in uniform flow possesses a boundary layer. And, in the case of a ventilated transom stern, the boundary layer is shed at the surface of the water. So, vorticity may be prominent at the wave surface. An explanation can be found in Figure 5.11, which is colored by the absolute value of the vorticity in the y-direction normalized by $\frac{U}{l}$. The lowest Reynolds number is considered, $Re = 1e4$, which corresponds to the greatest viscous stresses for the range of Reynolds numbers studied.

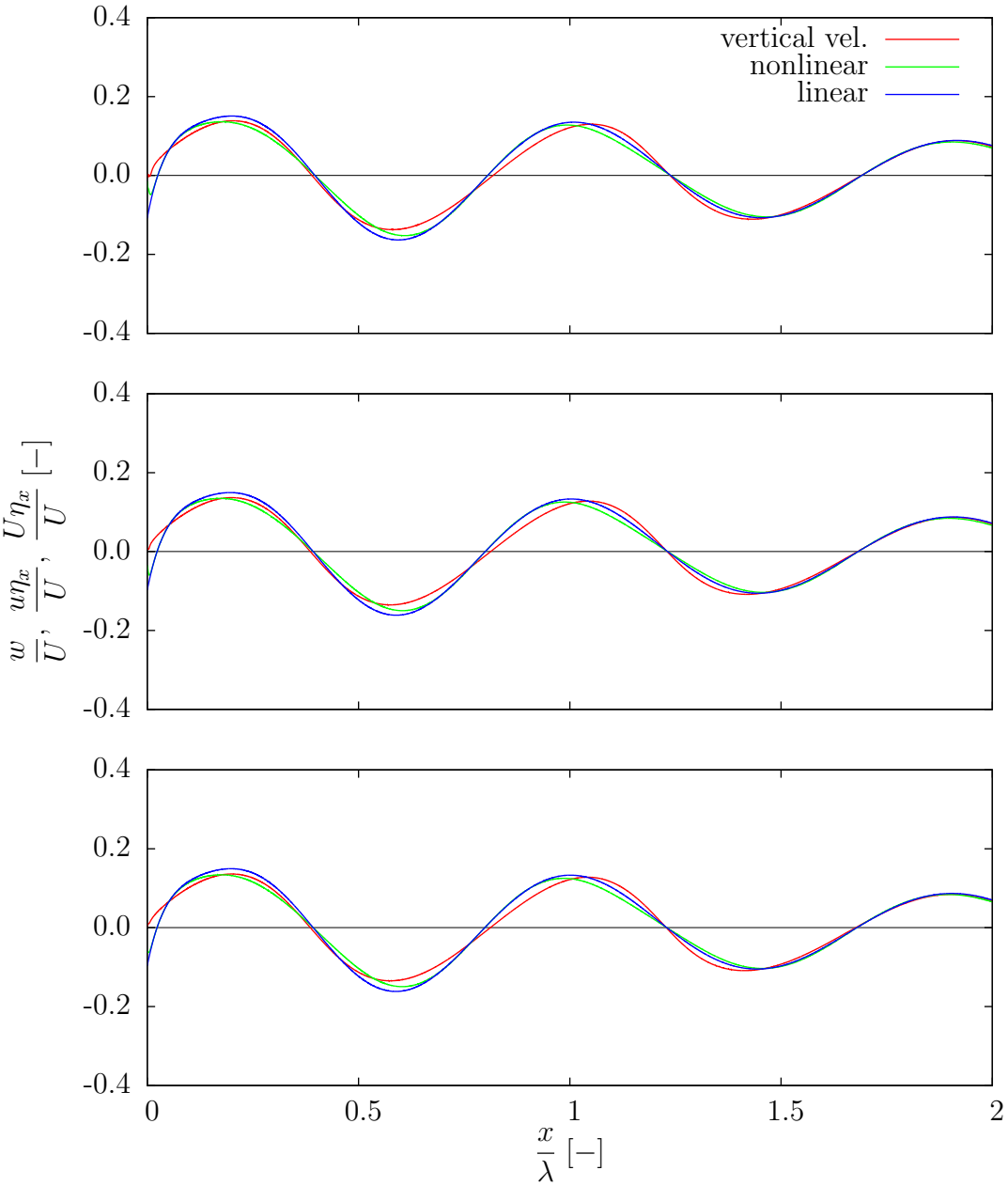

Figure 5.10: Nonlinear and linear kinematic conditions at water surface for Re=1e4 (top), Re=1e5 (middle), and Re=1e6 (bottom)

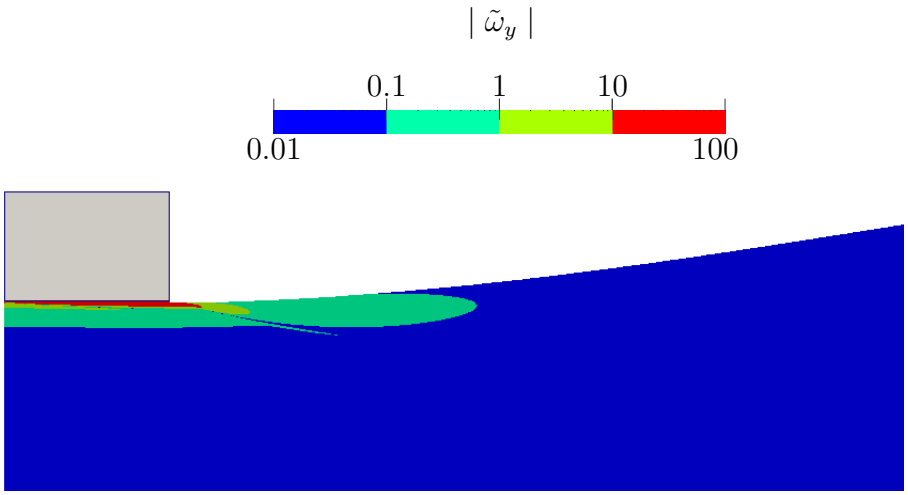

Figure 5.11: Vorticity within boundary layer and interaction with the water surface from VOF simulation

In this case, the boundary layer does not have a strong presence near the water surface. In fact, using the scale shown in Figure 5.11, it is only visible aft of the transom for less than 10% of the wavelength. These findings are consistent with those presented for the stresses at the air-water interface as well. The viscous terms, containing velocity gradients, are very small compared to the stresses arising from hydrodynamic and hydrostatic pressure. Therefore, suitable kinematic and dynamic boundary conditions are linear and inviscid, and these are adequately computed on the $z = 0$ plane. For a ship at full-scale, the Reynolds number can be greater, so the boundary layer may be relatively thinner, but the velocity gradients can be greater. Therefore, the intensity of this turbulence may cause the gradients to persist at the water surface further downstream than is being shown in this study.

5.2.2 $\mathbf{Fr_T = 2}$ – Unsteady Breaking Wave

This section presents the results for $Fr_T = 2$. The results from Section 5.2.1 show that the VOF method satisfies the stress balance interface condition and air stresses

are negligible, so only the free-surface assumption is evaluated in this section. The fundamental wavelength for this flow is $\lambda \approx 6.3m$. As with the steady wave case, this corresponds to an intermediate water depth, but the boundary condition used at the bottom does not enforce a no-penetration condition. At this Froude number, an unsteady breaking wave occurs aft of the transom. As such, a number of considerations must be made to appropriately convey important flow features. First, the wave slope varies from $0 \rightarrow \infty$, so the expression of the normal vector uses a standard global description:

$$\hat{n} = q\hat{i} + s\hat{k} \tag{5.20}$$

This results in an alternative description of the total stress vector:

$$\overline{\overline{\sigma}} \cdot \hat{n} = \begin{bmatrix} \left(\tilde{p} - Fr^{-2}\tilde{\eta}\right) q & - & 2Re^{-1}\tilde{u}_x q + Re^{-1}\left(\tilde{u}_z + \tilde{w}_x\right) s \\ -\left(\tilde{p} - Fr^{-2}\tilde{\eta}\right) s & - & Re^{-1}\left(\tilde{w}_x + \tilde{u}_z\right) q + 2Re^{-1}\tilde{w}_z s \end{bmatrix} \tag{5.21}$$

The magnitudes of the viscous terms are again summed within each component of Equation 5.21 for a conservative approach to investigate the viscous effects at the free-surface. Then, the hydrodynamic and hydrostatic pressures are presented, pn_z and $\rho g \eta n_z$, from the vertical component of the stress vector. The simulations are two-dimensional, but a slight rotation is performed about the $x-$axis to improve visualization of the iso-surfaces. For a three-dimensional investigation of interface stresses under breaking wave conditions see Filip (2013).

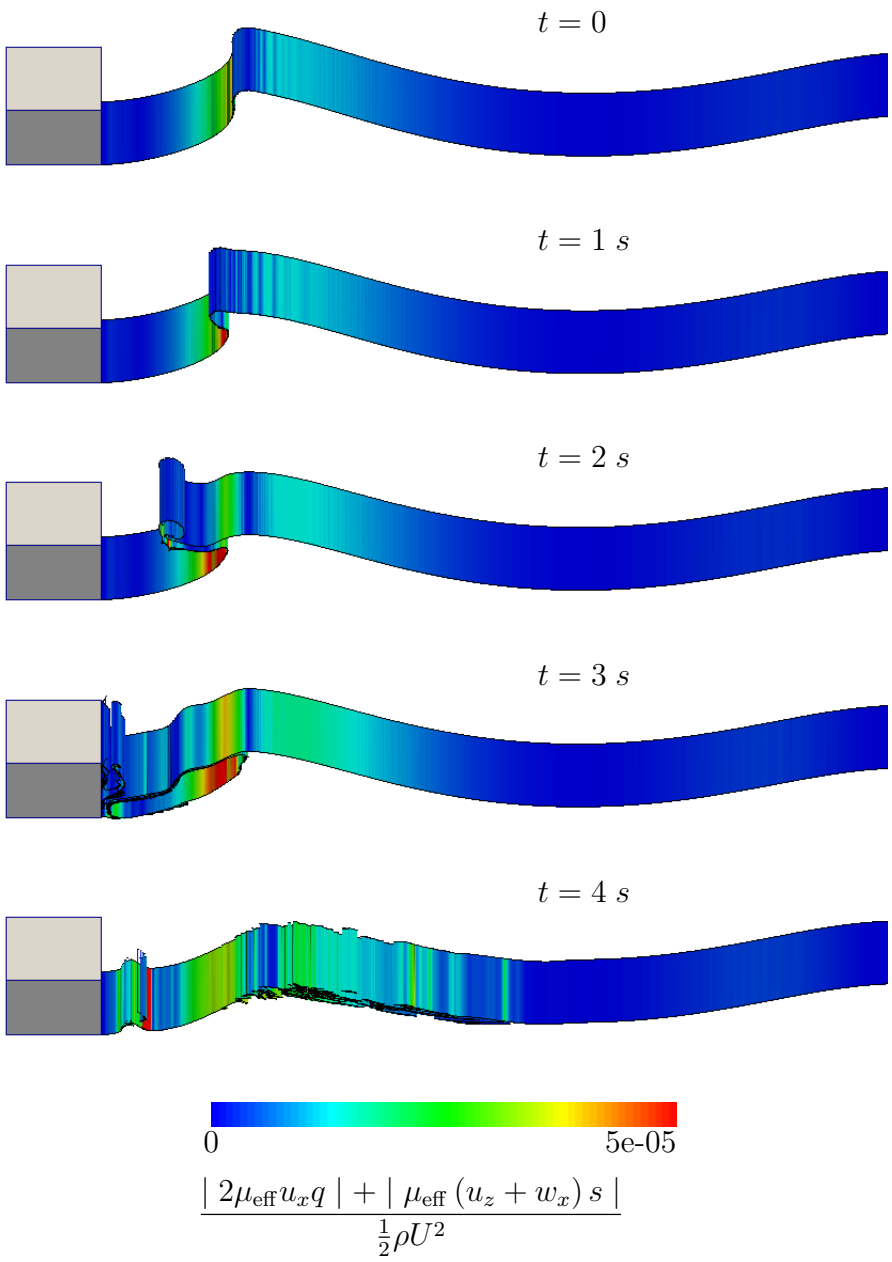

Figure 5.12: Re=1e4, Magnitudes of the horizontal viscous stresses as the wave breaks

Five instances in time are shown, each at one second intervals, to describe the breaking of the wave. At first, the formation of a nonlinear wave can be seen. The crest of this wave travels towards the transom, eventually making contact with it and splashing. As the water from the splash falls back to the surface of the water, air entrainment is produced and then washed downstream. Therefore, the final time step shown contains air bubbles beneath the water surface.

The summation of the magnitudes of viscous terms are presented in Figure 5.12 for the horizontal stress component and in Figure 5.13 for the vertical component. The quantities are very small, the majority being less than 0.005% of the stagnation pressure. So, this flow does produce viscous terms greater than those from $Fr_T = 3$ but no more than 10 times greater, indicating that a free-surface approximation is still valid.

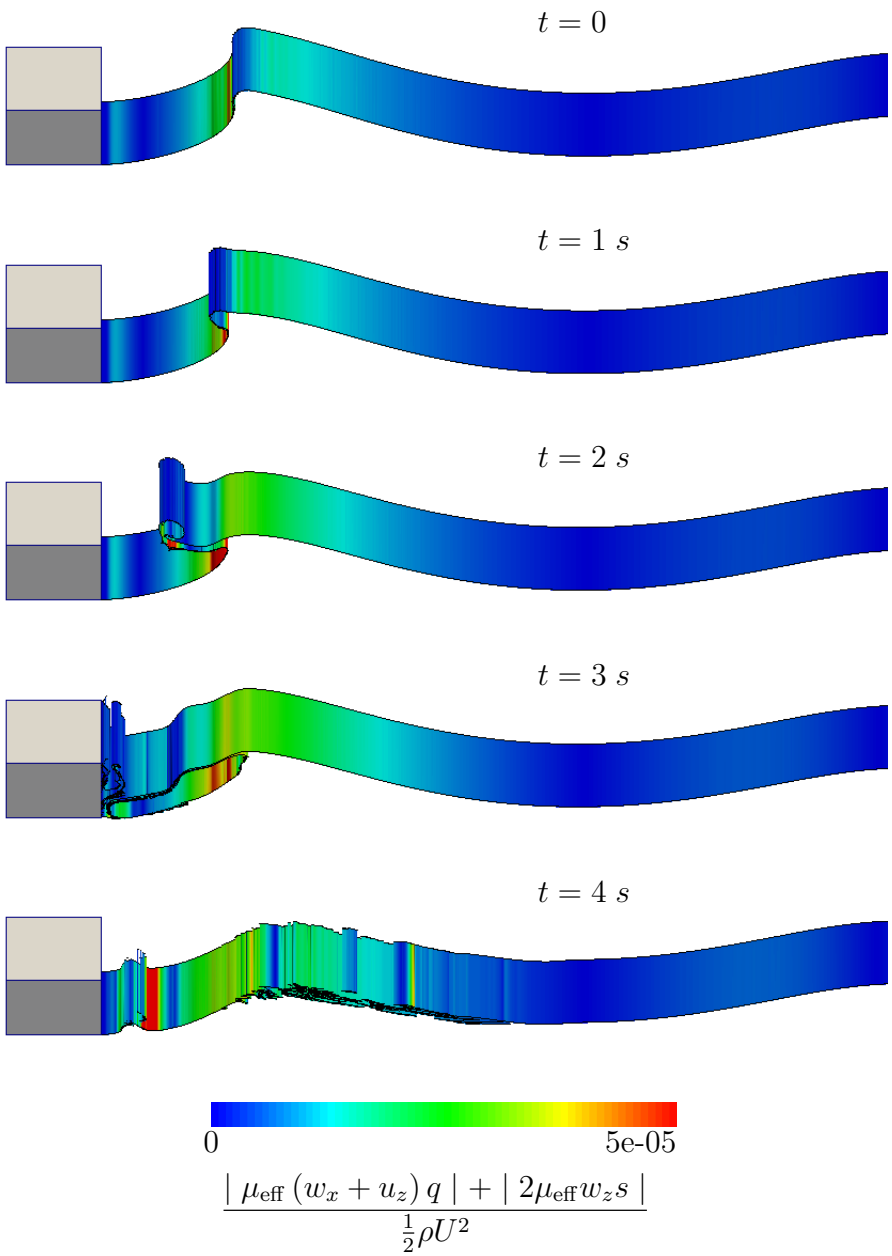

Figure 5.13: Re=1e4, Magnitudes of vertical viscous stresses as the wave breaks

The hydrodynamic and hydrostatic pressure from the vertical component of the stress vector are displayed in Figures 5.14 and 5.15. The figures are nearly identical, indicating that the dynamic and static pressure are in balance ($p = \rho g \eta$). The pressures are up to 80% of the stagnation pressure. Although the flow features from this breaking wave appear much different than the steady wave from $Fr_T = 3$, the magnitudes of the various stresses are similar. Specifically, the hydrodynamic and hydrostatic pressure are still far greater than the viscous stresses. In addition, the results do not change with changes in the Reynolds number, other than the linear scaling of the viscous terms which is also seen in the afore presented case. As such, the remaining results from this case, with $Re = 1e5$ and $1e6$, are located in Appendix A.

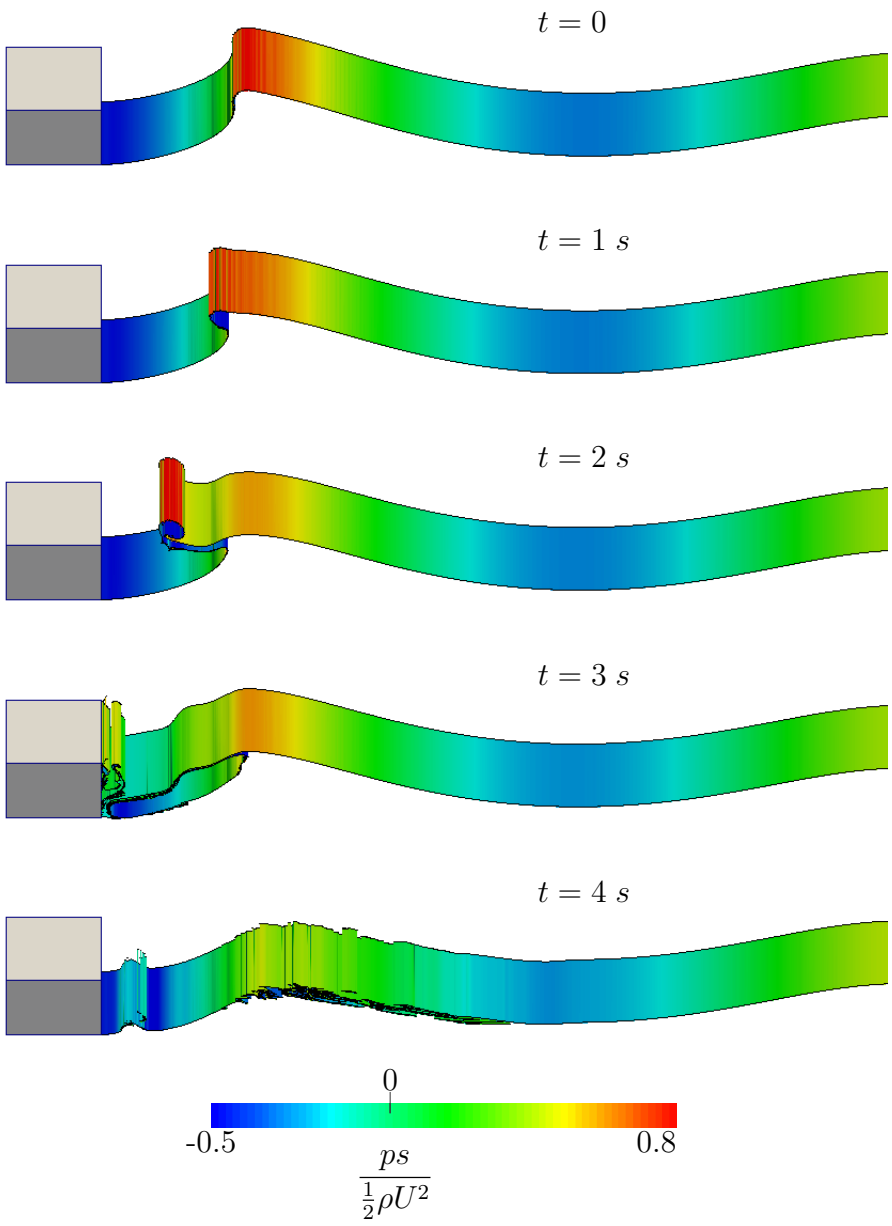

Figure 5.14: Re=1e4, Hydrodynamic pressure as the wave breaks

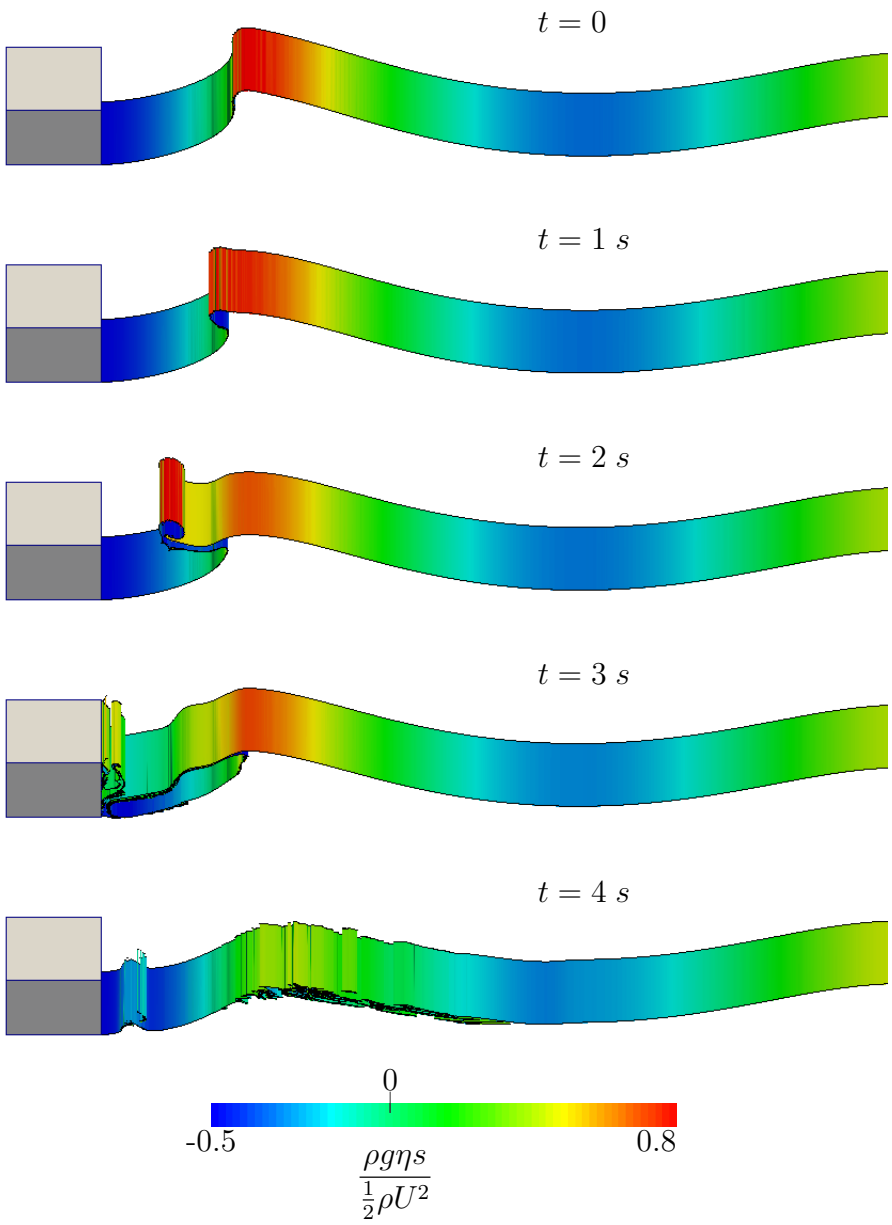

Figure 5.15: Re=$1e4$, Hydrostatic pressure as the wave breaks

The viscous stresses are small, but the use of a linearized free-surface boundary condition still raises questions as to whether this case can be approximated on the $z = 0$ plane. In order to determine this possibility, the linearized URANS method is used to replicate the experiment. The free-surface elevation and pressure are set to the bottom of the transom, $\eta = -0.25m$ and $p = -5517.5Pa$. This is the same

approach as used in the case where $Fr_T = 3$. Again, the back face of the transom employs a zero normal-gradient condition on the velocity, but the bottom, or keel, uses a no-slip condition. Figure 5.16 shows the wave elevations computed with the two methods.

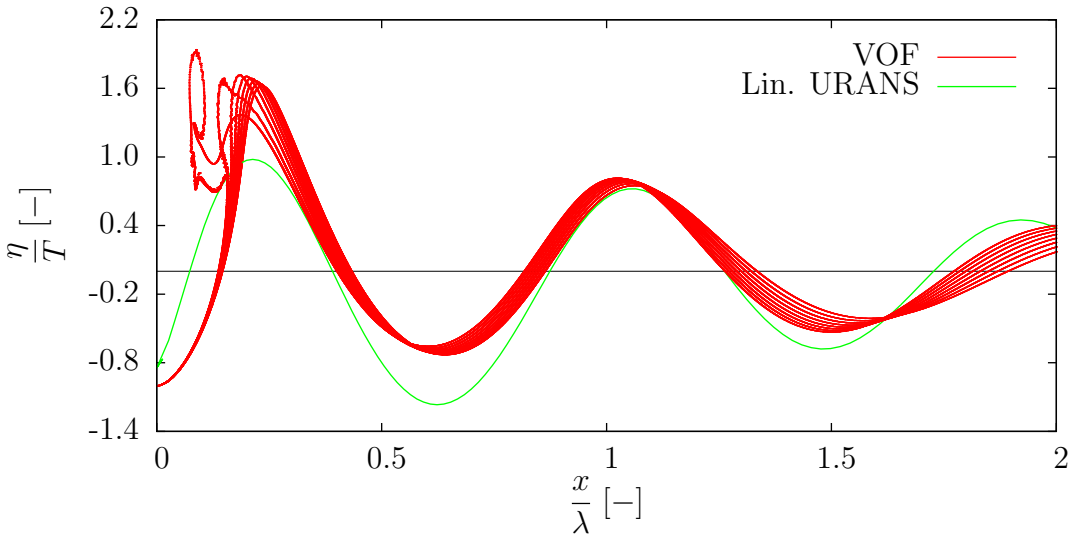

Figure 5.16: Wave elevations using VOF and linerized URANS for $Fr_T = 2$ and $Re = 1e4$

The elevation shown for the VOF method is captured at several instances in time, spanning just prior to the wave overturning through it breaking. A steady wave is produced with the linearized URANS method. It is not to suggest that one should use the linearized URANS method for the study of breaking waves, but it is promising to see how well the calculation can be transferred to the $z = 0$ plane, even within a regime that results in unsteady breaking waves. As is seen with $Fr_T = 3$, the linear conditions show a wave with lower values of elevation at crests and troughs. However, the method agrees well to VOF method in terms of the wave length which is computed.

5.2.3 $\mathbf{Fr_T = 0.2}$ – Low Froude Number Regime

This section contains the results for the set of data where $Fr_T = 0.2$. A fundamental wavelength of $\lambda \approx 0.063m$ is associated with this regime. The normal unit vector, $\hat{n}$, is expressed in terms of the water surface elevation, η. Figure 5.17 shows the water surface elevations. Changes in Reynolds number do not significantly change the water surface elevation.

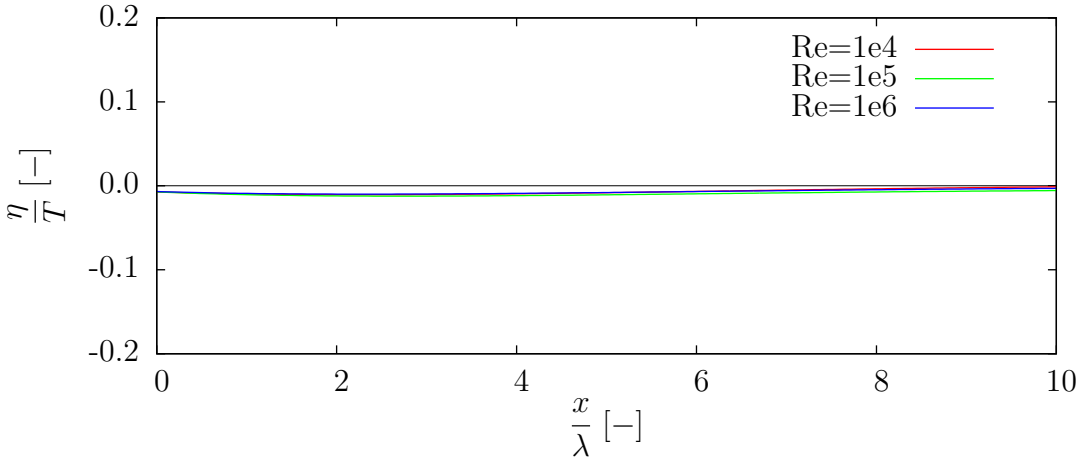

Figure 5.17: Wave elevations

For this discussion, the viscous terms are shown individually for both the horizontal and vertical components of the stress vector in Figure 5.18. The terms are very small. The static nature of this case presents difficulties with the smearing of the interface. Near the back face of the transom, the fluid does not adequately convect downstream to produce a crisp interface. Instead, a large interface exists, spanning several cells, and contains a slurry of fluid which is much denser than air. As such, using a rigorous phase-indicator variable cutoff of $\alpha = 0.99$ results in a water surface elevation which is too low. Therefore, a more suitable value of $\alpha = 0.5$ is used for the data presented at this low Froude number regime.

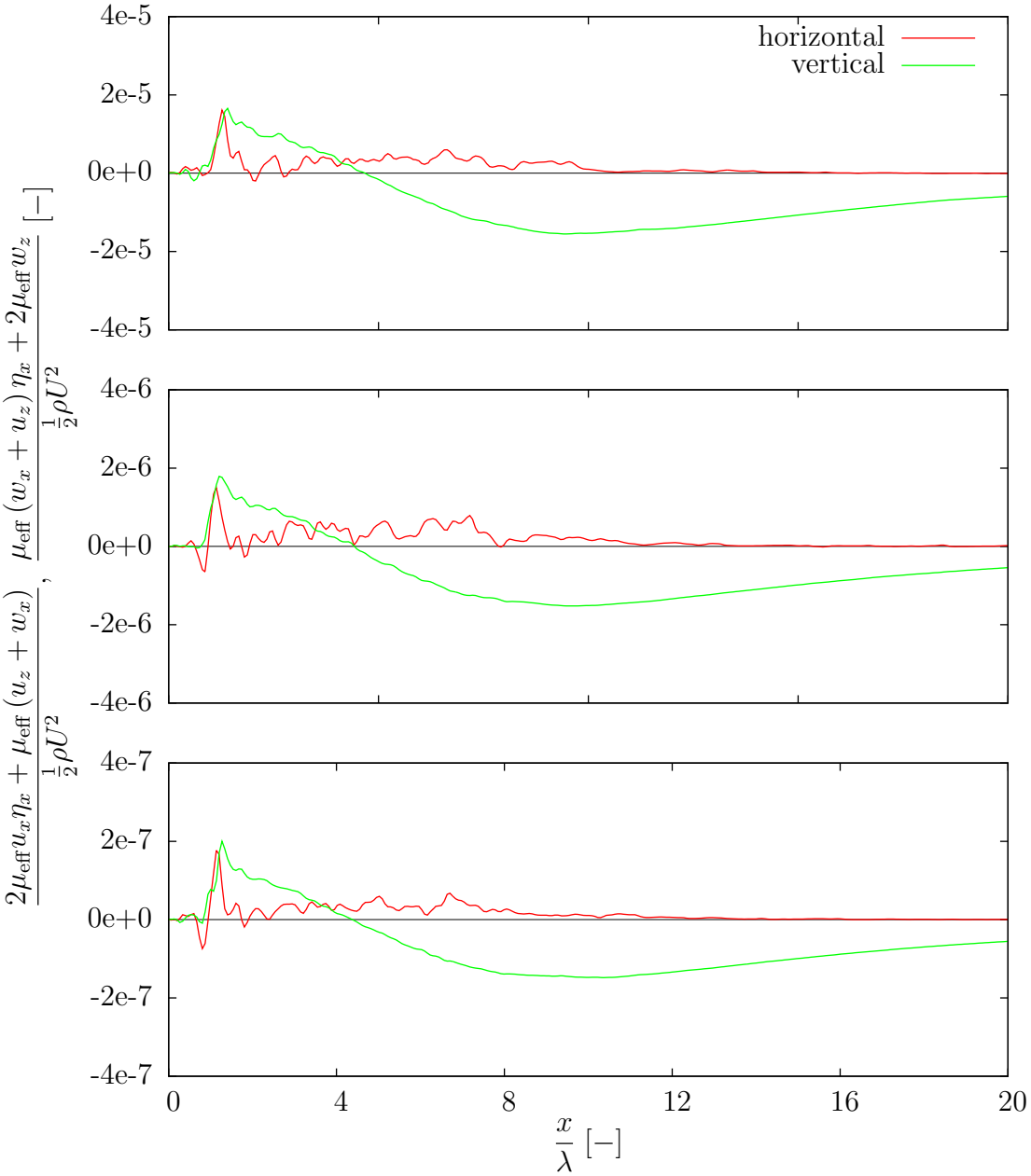

Figure 5.18: Viscous stresses for Re=1e4 (top), Re=1e5 (middle), and Re=1e6 (bottom)

Figure 5.19 presents the hydrodynamic and hydrostatic pressures from the vertical component of the stress vector. Since this case is largely governed by hydrostatic pressure, the stress scale used for non-dimensionalization is $\rho g T$. Indeed, air-water interface is disturbed little, which is reflected by the small static and dynamic pressures at the water surface. Also, the dynamic and static pressures are in balance. They are at most roughly 1% different in relation to the stress scale, $\rho g T$. The nearly flat interface causes pressures from the horizontal component of the stress vector to be even smaller, and, therefore, they are not plotted.

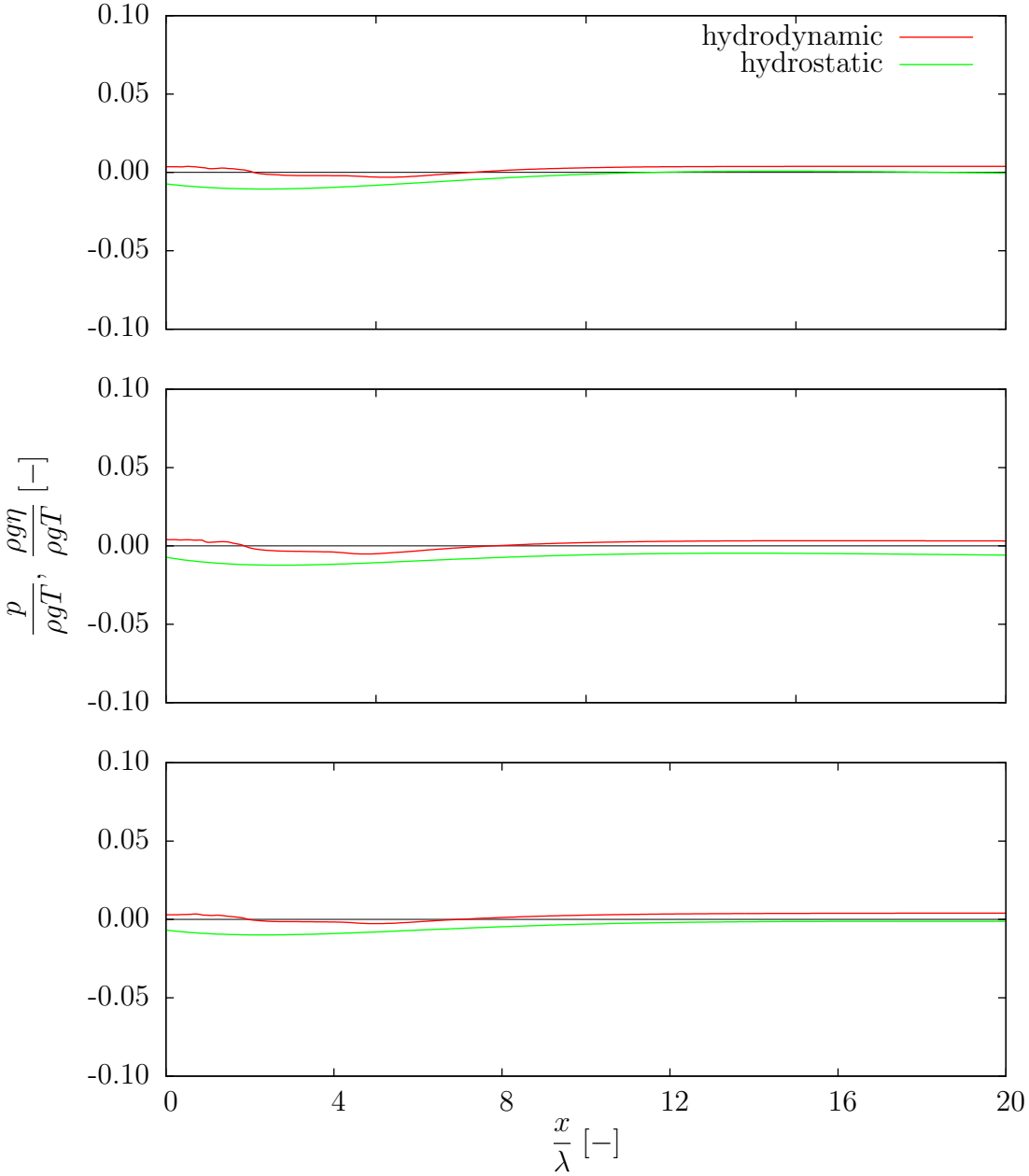

Figure 5.19: Hydrodynamic and hydrostatic pressure from vertical component of stress at water surface for Re=1e4 (top), Re=1e5 (middle), and Re=1e6 (bottom)

The comparison of the linear and nonlinear kinematic conditions can be seen in Figure 5.20. The nonlinear condition agrees slightly better with the vertical velocity from the solution close to the transom than the linear condition. Downstream, both methods perform similarly. Any differences between the linear, nonlinear, and actual values are small, being at most roughly 2% different in relation to the inlet velocity, U. Figure 5.21 displays the absolute value of vorticity in the y-direction. The recirculation region just aft of the transom corresponds to the region where the linear kinematic condition shows the largest difference. Here, the fluid velocity is less than the free-stream velocity, so the linear kinematic condition, using U, disagrees with the nonlinear condition. Still, employing the linearized condition results in a very agreeable solution to the free-surface elevation as depicted in Figure 5.22, which compares the VOF solution to the linearized URANS solution. At this Froude number, the linearized URANS simulation uses the same boundary conditions as the fully nonlinear approach. The back face of the transom uses a zero normal-gradient for the pressure and free-surface elevation. The velocity satisfies a no-slip boundary condition everywhere on the transom.

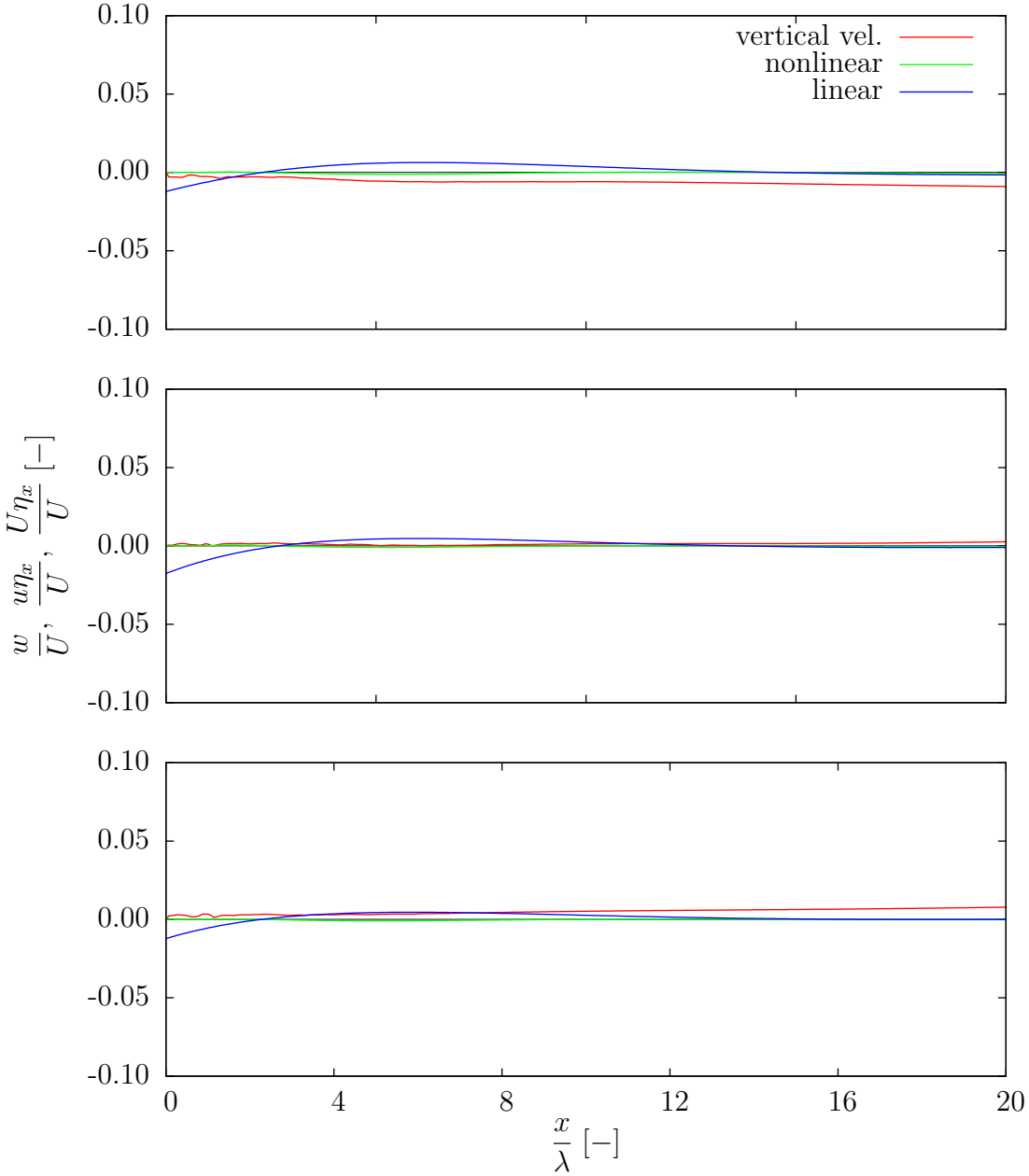

Figure 5.20: Nonlinear and linear kinematic conditions at water surface for Re=1e4 (top), Re=1e5 (middle), and Re=1e6 (bottom)

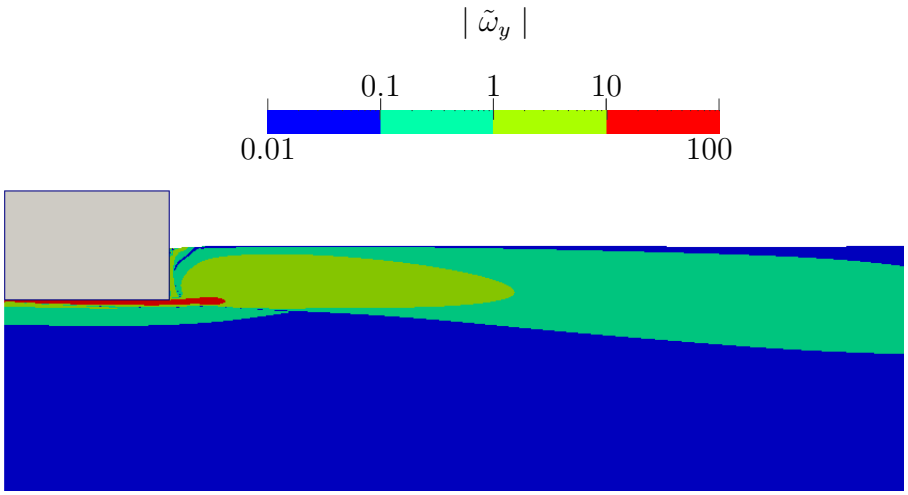

Figure 5.21: Vorticity within boundary layer and interaction with the water surface

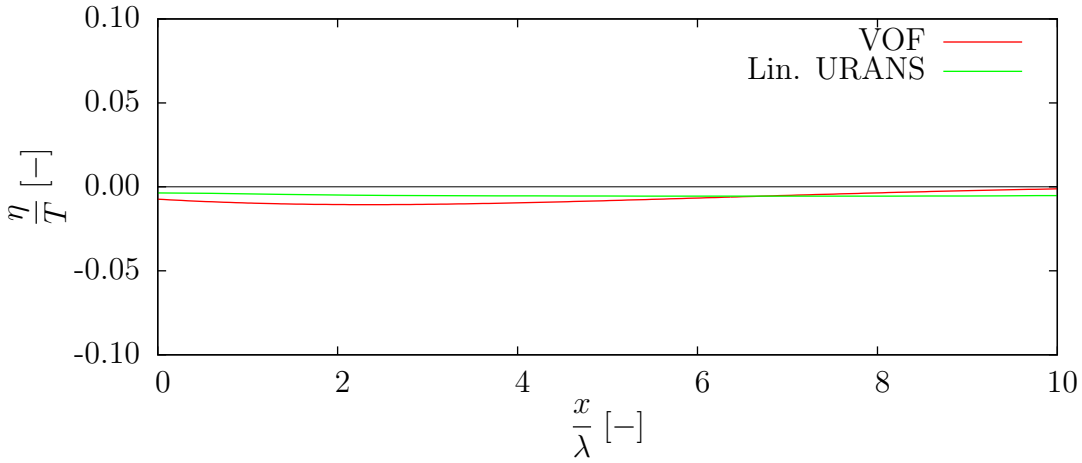

Figure 5.22: Wave elevations using VOF and linerized URANS for $Fr_T = 0.2$ and $Re = 1e4$

5.3 Summary of Findings

The two-dimensional viscous interface study allows for several important conclusions. First, the stress-balance of the air-water interface condition is satisfied using the VOF method. Any differences in stress from the air and water are very small and can be attributed to the rigor with which the phase-indicator variable thresholds are

implemented. In an attempt to measure values which are very nearly in air and water, $\alpha = 0.01$ and $\alpha = 0.99$ are chosen. This produces a finite gap between the two fluids where the interface resides. In addition, the magnitude of the stress in each fluid at the interface is shown to be very small, suggesting that only consideration of the stresses in the water through the free-surface approximation is an appropriate assumption. From here, this free-surface condition is evaluated with nine combinations of Froude and Reynolds numbers.

The ventilated transom produced with $Fr_T = 3$ results in a steady, non-breaking wave. A conservative approach is taken to determine the effect of the viscous terms in the free-surface condition by summing the magnitude of each term. It is shown that this summation is still very small and the viscous terms can be neglected. The hydrodynamic and hydrostatic pressure terms dominate in the horizontal and vertical components of the stress vector equation. Within these, the vertical terms are approximately ten times larger than the horizontal terms. Therefore, a zero total pressure condition in the vertical direction is suitable for the dynamic free-surface boundary condition. The kinematic condition is also studied with results showing little difference between a linear and a nonlinear approach, both of which agree well with the vertical velocity at the surface along the entire wave.

An unsteady breaking wave is produced at $Fr_T = 2$. This wave causes the ventilation of the transom to oscillate from fully to partially ventilated as the wave breaks and splashes against the back face of the transom. Iso-surfaces are used to convey important features of the data. The conservative summation of magnitudes is again taken when visualizing the viscous terms in the horizontal and vertical components of the stress vector. The effects of viscosity are larger in magnitude than the steady wave case, but they are still very small. It is clear that the hydrodynamic and hydrostatic pressures dominate the zero total stress condition, and they are very nearly in balance. A reasonable solution to this unsteady flow, transferred to the $z = 0$ plane,

is shown.

The final case addresses the Froude number $Fr_T = 0.2$ in which essentially no wave is generated. The viscous terms in the horizontal and vertical components of the stress vector are once again very small, being on the order of those from the case where $Fr_T = 2$. The values of the slope of the water surface, η_x, are very near zero everywhere. Therefore, the hydrodynamic and hydrostatic pressure from the horizontal component of the stress vector are practically zero. In addition, the static nature of the flow produces dynamic and static pressures in the vertical component of the stress vector which are very small. These are normalized by a static stress scale, $\rho g T$. Studying the kinematic condition shows the linear approach produces a small difference in the prediction of vertical velocity within the recirculation region just aft of the transom. The nonlinear condition agrees well with the vertical velocity in this region. Still, the linearized URANS method produces results which are very similar to those obtained with the fully nonlinear VOF method.

CHAPTER VI

Maneuvering Tests

This section presents results using the linearized URANS method on two variations of the David Taylor Model Basin (DTMB) 5415 destroyer hull form. The first variation is the DTMB 5415, which is unappended with the exception of bilge keels. In the literature, this is referred to as the bare hull. The second variation is the DTMB 5415M, which is fully appended with bilge keels, stabilizer fins, five-bladed inward-rotating propellers, spade rudders, exposed propeller shafts, and A-frame shaft brackets. This is accordingly referred to as the appended hull.

Results are mainly focused on forces and moments in the horizontal plane. These ship-fixed forces are an axial surge force, X, a lateral sway force, Y, and a yaw moment about midship, N. The propeller thrust force, T, acts along the propeller shaft axis-of-rotation. Each force and moment is presented in a dimensionless manner, as shown in Equation 6.1.

$$\begin{aligned} X', Y', T' &= \frac{X, Y, T}{0.5\rho U_c^2 A_o} \\ N' &= \frac{N}{0.5\rho U_c^2 A_o L_{\text{pp}}} \end{aligned} \tag{6.1}$$

The carriage speed is denoted with U_c. The length between perpendiculars is L_{pp}, and the lateral underwater area, A_o, is $L_{\text{pp}}T$ where T is the draft.

Unstructured grids are used for both hulls with the native semi-automatic mesh generator in OpenFOAM, snappyHexMesh, which allows for a hexahedron dominant mesh as well as boundary layer prisms on hull surfaces. The hands-off nature of snappyHexMesh coincides with the goal of design efficiency for this linearized method. The Spalart-Allmaras turbulence model is used with an adaptive wall function. Simulations are performed in an inertial, Earth-fixed reference frame. The linearization restricts body-exact ship motions to those in the horizontal-plane (surge, sway, and yaw). The rotation of propellers is performed with a sliding mesh communication, or arbitrary mesh interface (AMI) in OpenFOAM. Details of this technology can be found in Farrell and Maddison (2011), and an application is shown in McNaughton et al. (2014).

6.1 DTMB 5415 - Bare Hull

Prescribed PMM tests are conducted with the DTMB 5415 bare hull. These consist of static drift, pure sway, and pure yaw tests and are compared with experimental data from the Iowa Institute of Hydraulic Research (IIHR) (Longo et al., 2006) and from FORCE Technology in Denmark (Agdrup, 2004). The IIHR model is fixed at the dynamic sinkage and trim, whereas the FORCE Technology model is free to sink and trim. The hull used in the IIHR physical experiments is displayed in Figure 6.1, and the model characteristics are shown in Table 6.1.

Figure 6.1: DTMB 5415 bare hull model from IIHR experiments. Top photograph shows the keel and both bilge keels

Table 6.1: IIHR DTMB 5415 model principle characteristics

Item	Symbol	Value	Unit
Scale factor	λ	46.588	–
Length	L_{pp}	3.048	m
Waterline length	L_{wl}	3.052	m
Beam	B_{wl}	0.410	m
Draft	T	0.136	m
Mass	m	83.35	kg
Lateral area	A_o	0.415	m^2

Only the pure sway and pure yaw maneuvers are compared to experimental data from FORCE Technology in Denmark. The hull used in these experiments is shown in Figure 6.2, and the model characteristics appear in Table 6.2.

Figure 6.2: FORCE DTMB 5415 bare hull model

Table 6.2: FORCE DTMB 5415 model principle characteristics

Item	Symbol	Value	Unit
Scale factor	λ	35.48	–
Waterline length	L_{wl}	4.002	m
Beam	B_{wl}	0.538	m
Draft	T	0.174	m
Mass	m	190.7	kg
Lateral area	A_o	0.696	m^2

In order to monitor spatial discretization errors, three grids are used for each PMM test. The geometry of the hull corresponds to that of the IIHR 5415 model. A replica of the FORCE Technology model is not tested numerically. The grid characteristics are provided in Table 6.3. All grids contain less than one million cells, and the average y^+ values are between 40 and 60. The inertial, Earth-fixed approach to these simulations allows the same grid to be used for each of the maneuvers herein as well as many others.

Table 6.3: DTMB 5415 linearized URANS grid characteristics

	Cell Count	y^+_{avg}
Coarse	2.02×10^5	60.1
Medium	3.98×10^5	50.0
Fine	9.18×10^5	41.7

A summary of the test parameters for the maneuvering simulations is provided in Table 6.4. These correspond to the experiments performed at IIHR and those conducted numerically.

Table 6.4: DTMB 5415 maneuvering test parameters

Item	Symbol	Value	Unit
Carriage speed	U_c	1.531	m/s
Froude num.	Fr	0.280	
Reynolds num.	Re	4.464×10^{6}	
Gravity	g	9.81	m/s^2
Water density	ρ	1000	kg/m^3
Water viscosity	ν	1.00×10^{-6}	m^2/s
Static drift			
Drift angle	β	10	deg
Pure sway			
Sway amplitude	η_0	0.317	m
Sway frequency	N_{pmm}	8.021	min^{-1}
Pure yaw			
Sway amplitude	η_0	0.327	m
Yaw amplitude	ψ_0	10.2	deg
Yaw frequency	N_{pmm}	8.021	min^{-1}

6.1.1 Static Drift

The static drift simulations are compared to experimental data from IIHR. Mesh motion is governed by Equation 6.2 for the static drift test, where $\beta = 10°$:

$$\begin{aligned} \beta &= -\tan^{-1}\left(\frac{v}{u}\right) \\ U_c &= \sqrt{u^2+v^2} \end{aligned} \tag{6.2}$$

The steady nature of the static drift test presents an opportunity to perform a grid convergence study with the linearized URANS approach because determination of the time-averaged values is straight-forward compared to the unsteady forces of the dynamic cases. First, the ASME uncertainty procedure is used to find an observed order of accuracy, p (ASME, 2008). However, the ASME procedure is based on Richardson extrapolation, where the observed order of accuracy should be no greater than $p = 2$. Since unrealistic super-convergence ($p > 2$) is observed in this static drift

case, the ASME uncertainty procedure is departed from in favor of a procedure which addresses this unrealistic behavior. As such, after calculating the observed order of accuracy, the remainder of assessing the uncertainty is performed with the guidelines in Eça (2006). The approach from Eça (2006) begins with a convergence condition that is determined with Equation 6.3:

$$R = \frac{\phi_2 - \phi_1}{\phi_3 - \phi_2} \tag{6.3}$$

$$\begin{aligned} 0 < R < 1 &\Rightarrow \text{Monotonic convergence} \\ -1 < R < 0 &\Rightarrow \text{Oscillatory convergence} \\ R > 1 &\Rightarrow \text{Monotonic divergence} \\ R < -1 &\Rightarrow \text{Oscillatory divergence} \end{aligned}$$

Here, ϕ_3, ϕ_2, and ϕ_1 stand for the solutions on the coarse, medium, and fine grids. The surge force displays monotonic divergence, so an observed curve of convergence will not contribute to a comparison with the theoretical curve of convergence based on Richardson extrapolation. However, the sway force and yaw moment show monotonic convergence, so for Y' and N' such a comparison can be valuable. Both the theoretical and observed curves of convergence can be obtained using a least squares approach to solve for ϕ_o and α in Equation 6.4.

$$\phi_i = \phi_o + \alpha \left(\frac{h_i}{h_1}\right)^p \tag{6.4}$$

Here, ϕ_o represents the extrapolated value (an estimated value corresponding to cell size $h_i = 0$), and α is a constant coefficient. A representative cell size for each grid is denoted with h_i, where h_1 corresponds to the finest grid. Equation 6.4 results in theoretical curves of convergence when $p = p_{\text{th}} = 2$, and observed curves of convergence when the observed order of accuracy is used for p. The behavior of each force

and moment can be seen in Figure 6.3. The latter two show the sway force and yaw moment, respectively. Here, the monotonic grid convergence can be seen, as well as the extrapolated values as $h_i/h_1 \to 0$.

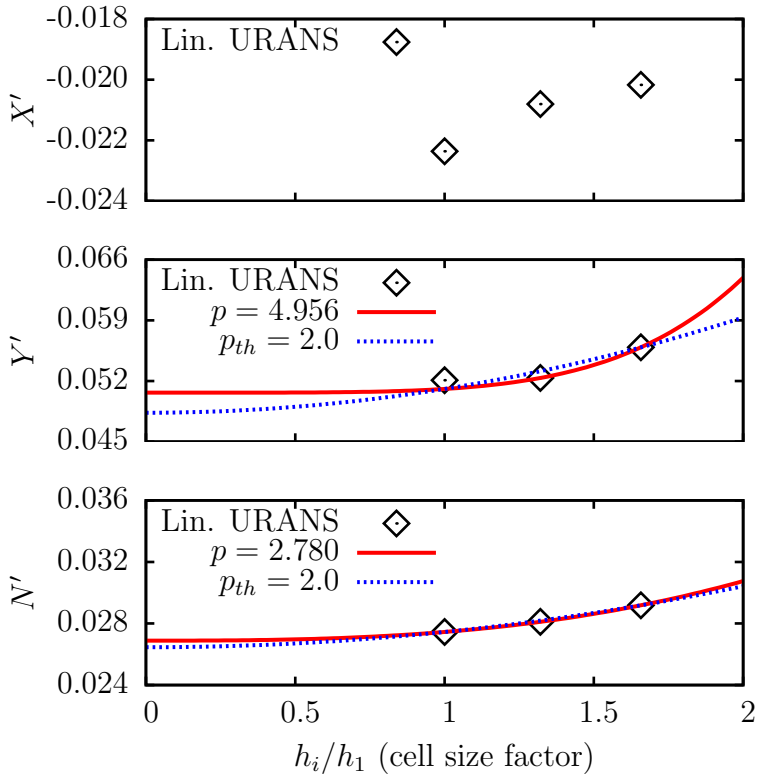

Figure 6.3: Grid convergence study for static drift

Due to the monotonic divergence and the super-convergence seen, an uncertainty assessment based on Richardson extrapolation is not reliable. Instead, a factor of safety is used, as presented in Equation 6.5:

$$\begin{aligned} U_\phi &= F_s \Delta_M \\ \Delta_M &= \max\left(\mid \phi_\mathrm{i} - \phi_\mathrm{j} \mid\right) \end{aligned} \tag{6.5}$$

The uncertainty is represented with U_ϕ. The factor of safety is F_s, and Δ_M is the maximum difference in the solution among the grids. For the monotonic divergence of the surge force, it is suggested that $F_s = 3$. The sway force and yaw moment show monotonic convergence and employ a value of $F_s = 1.25$. These findings are summa-

rized in Figure 6.4, where the fine grid results are plotted with the uncertainties.

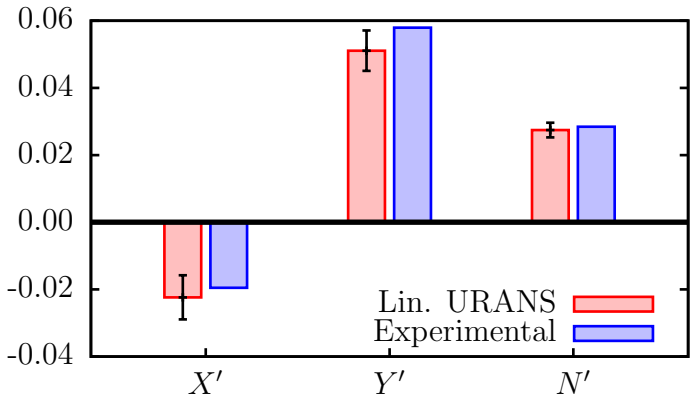

Figure 6.4: Forces and moment with numerical uncertainties for static drift

To highlight benefit of the linearized URANS method, the static drift simulation was repeated using a double-body approximation which is a common approach to maneuvering simulations mainly due to its simplicity and efficiency. This method enforces a flat free-surface, and thus it does not account for wave effects. For this reason, it is also referred to as a zero-Froude number approximation. The coarse grid containing just over 200,000 cells is used with both approaches for the comparison. Figure 6.5 shows the major differences in the dynamic pressure solution at the $z = 0$ calm-water plane. This can also be viewed as the solution to the free-surface elevation, since dynamic pressure and elevation are directly related ($p = \rho g \eta$). Both show a high pressure zone corresponding to the bow wave on the windward side, but the linearized URANS method accurately solves for the waves that are generated on the leeward side. These waves dissipate rapidly away from the hull simply due to the coarseness of the grid. Along with obtaining accurate forces, efficiency is a primary goal, so grids containing as few cells as possible are used.

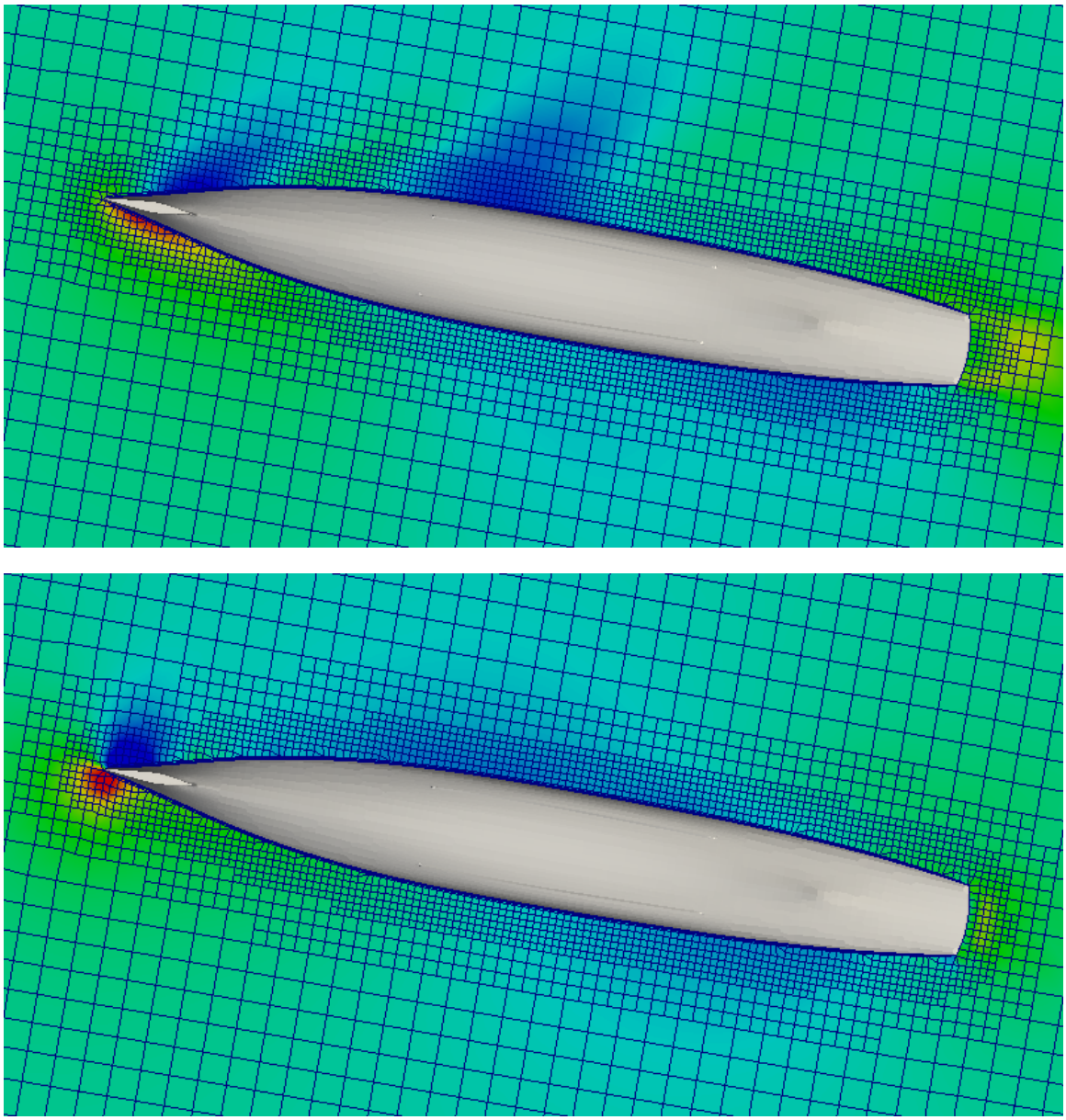

Figure 6.5: Coarse grid pressure comparison of linearized URANS (top) and double-body (bottom) for static drift $\beta = 10^{\circ}$

To give a more quantitative comparison, the forces obtained using both techniques are shown in Figure 6.6. Both methods perform well in predicting the surge force obtained with the physical experiments. However, the zero Froude approach shows a difference of over 20% for both the sway force and yaw moment. On the other hand, the linearized URANS method still compares well to the experiments being less than 5% different in all categories.

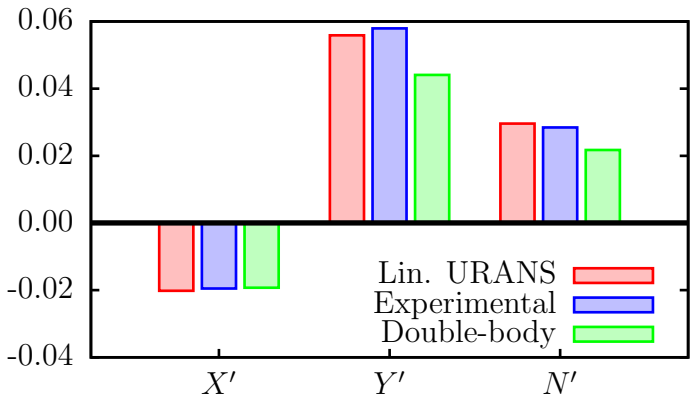

Figure 6.6: Static drift for linearized URANS and Double-body

The computational expense of each method is also important. The linearized URANS method requires 10% more computing time than the double-body simulation. Specifically, 9.29 hours vs. 8.43 hours on 12 processors for 60 seconds of simulated time. For a slightly greater expense, the improved accuracy of accounting for first-order wave effects is significant and still possible to obtain with workstation computing.

6.1.2 Pure Sway

Results for the pure sway test are compared to both IIHR and FORCE Technology experiments. The mesh motion for the pure sway test is shown in Equation 6.6:

$$\eta_{\text{sway}} = -\eta_0 \sin\left(\frac{2\pi N_{\text{PMM}}}{60} t\right) \tag{6.6}$$

The numerical carriage velocity is a constant $U_c = 1.531 m/s$, and the corresponding sway motion period is $7.48 s$. In addition to the experimental data from the two testing facilities, results from a fully nonliner method are provided from Miller (2008). These are obtained with CFDShip-Iowa which uses a level-set method to solve for the location of the water surface. One set of CFDShip-Iowa results correspond to simulations performed with a domain that is consistent with the dimensions of the

tank at IIHR. The second set corresponds to the FORCE Technology tank dimensions. As such, results are grouped by testing facility and the corresponding CFDShip-Iowa data. The linearized URANS results are the same within these two groups. The fully-nonlinear grids employ just over 4.5 million cells. Table 6.5 shows the dimensions of the two tanks.

Table 6.5: Comparison of IIHR and FORCE tank dimensions

	Length	Width	Depth	[m]
IIHR	100	3	3	
FORCE	240	12	5.5	

Forces and moments compared to IIHR data over one PMM period are displayed in Figure 6.7. The surge force from the linearized URANS results does not possess the amount of variation that the experimental signal does, but the time-averaged values of each are quite similar. The time-averaged values are in slightly worse agreement for the CFDShip-Iowa results. The linear predictions of sway force show a noticeable shift with respect to the experimental data, but they are otherwise in good agreement. The CFDShip-Iowa prediction is in excellent agreement with the experiments. This may indicate that the physical tank boundaries affect the forces and need to be modeled numerically as in the CFDShip-Iowa results. Indeed, the tank is only $3m$ wide, so the sway amplitude of $\eta_0 = 0.317m$ causes the model to traverse over 20% of the tank width. Lastly, all methods display good agreement of the predicted yaw moment.

Forces and moments compared to FORCE Technology data over one PMM period are displayed in Figure 6.8. The time-averaged values of the linearized URANS surge force are in decent agreement with experimental data. Fully-nonlinear data shows great agreement, even with prediction of the variation in amplitude of the surge force. The linear predictions of sway force again show a noticeable phase shift with respect to the experimental data, but they are otherwise in close agreement, and the CFDShip-Iowa prediction is very close to the experiments. Each method shows

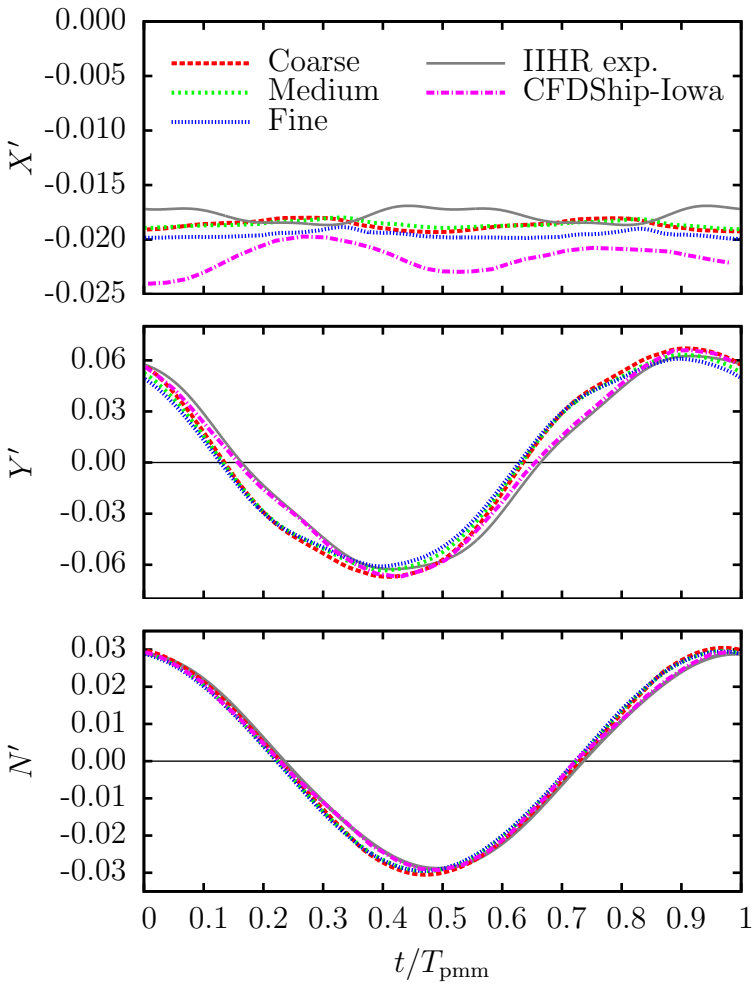

Figure 6.7: Forces and moment during pure sway compared to IIHR experiments

similar predictions of the yaw moment.

A highly important feature of these results is the very little difference between the three grids employing the linear method. Using 400,000 cells shows almost no difference than using just over 900,000 cells. Even the coarse grid with approximately 200,000 cells provides impressive predictions. Furthermore, the coarseness of these grids is seldom, if ever, seen being used with fully nonlinear methods. In general, far greater resolution is needed to see the grid-to-grid agreement that is demonstrated with the linearized URANS method. For instance, the nonlinear results compared here are obtained on a grid with 4.5M cells.

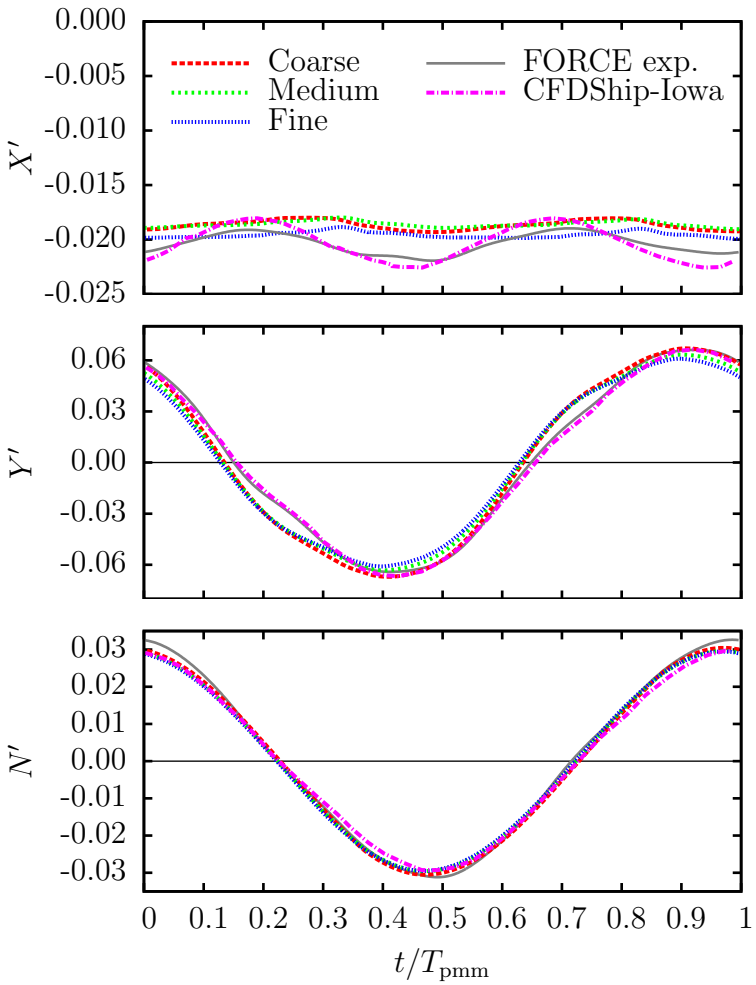

Figure 6.8: Forces and moment during pure sway compared to FORCE Technology experiments

6.1.3 Pure Yaw

The motion governing the pure yaw maneuver appears in Equation 6.7:

$$\begin{aligned} \psi_{\text{yaw}} &= -\psi_0 \cos\left(\frac{2\pi N_{\text{PMM}}}{60} t\right) \\ \eta_{\text{sway}} &= -\eta_0 \sin\left(\frac{2\pi N_{\text{PMM}}}{60} t\right) \end{aligned} \tag{6.7}$$

For this test, the sway amplitude is $\eta_0 = 0.327m$, and the maximum heading angle is $\psi_0 = 10.2°$. As with the pure sway tests, results from both IIHR and FORCE are shown along with CFDShip-Iowa data corresponding the the two tank dimen-

sions. The three grids from the linearized URANS simulations are the same for both comparisons.

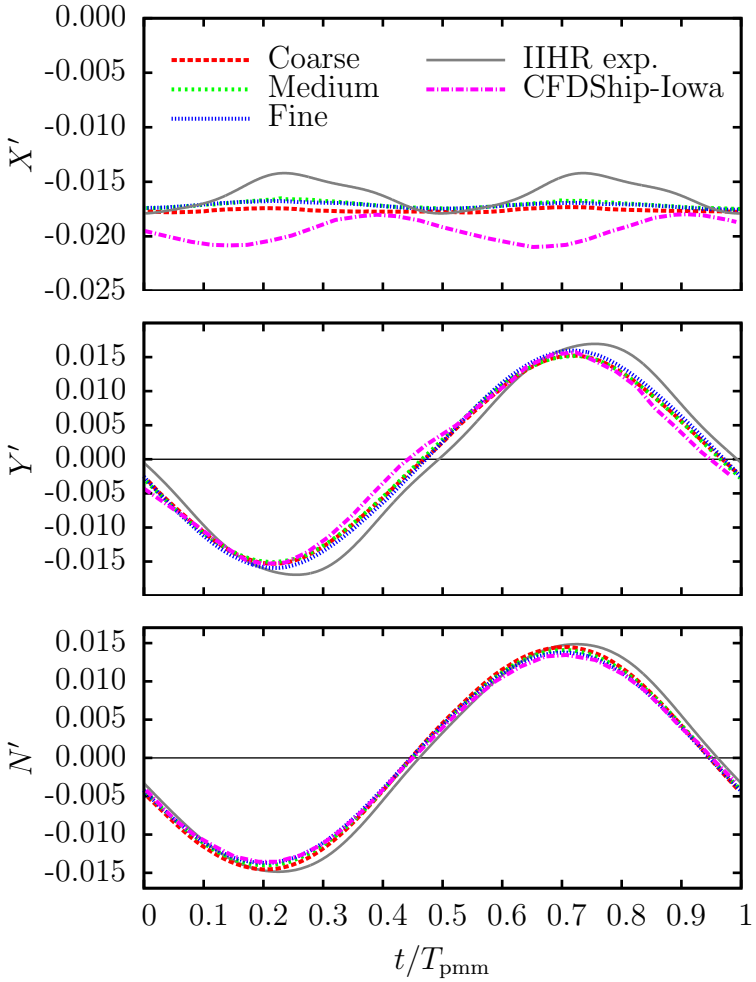

Figure 6.9: Forces and moment during pure yaw compared to IIHR experiments

Results for the forces and moments compared to the IIHR experiments appear in Figure 6.9. Predictions of the surge force from the linear simulations do not fully capture the variation in the amplitude of the signal from the experimental data. However, the time-averaged values from both agree closely. The variation in amplitude is obtained with the CFDShip-Iowa simulation, but the average of the force is less comparable to the experiment. All numerical methods show reasonable consistency in predicting the sway force except for a slight shift compared to the experiments. Finally, all numerical and experimental data is in quite close agreement for the yaw

moment.

Results corresponding to FORCE Technology experiments are displayed in Figure 6.10. Far less variation is seen in the amplitude of the surge force compared to the IIHR tank in Figure 6.9. The CFDShip-Iowa simulations show the closest predictions to the experiments, but the linearized URANS data are also closely predictive. A noticeable difference in the experimental sway force can been seen, as it shows a larger amplitude than each numerical method. This may be because the model is free to heave and pitch in the experiments. The linear simulations show the closest agreement to this experimental force. Lastly, each method agrees well in predicting the yaw moment.

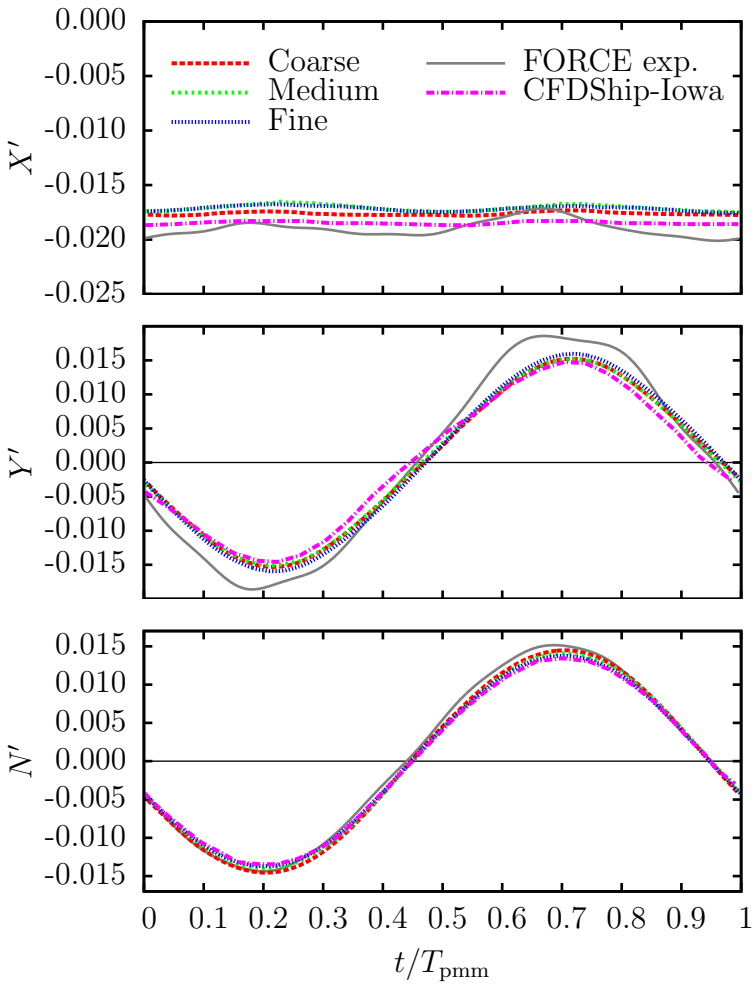

Figure 6.10: Forces and moment during pure yaw compared to FORCE Technology experiments

6.1.4 CPU Requirements

Computational efficiency is also a primary goal of the linearized URANS methodology. The CPU expense is calculated by multiplying the walltime with the number of processors. This expense is reported in CPU hours for the dynamic maneuvers on each grid in Table 6.6.

The solution of one PMM period using linearized URANS simulations can require far less time than the nonlinear methods. The time step was manually set with CFDShip-Iowa, and these simulations require the greatest amount of processing time. Additionally, it should be noted that the CPU hours for the linearized

Table 6.6: CPU hours per PMM period

	Pure sway	Pure yaw
Coarse	11.5	10.4
Medium	56.3	35.8
Fine	221.9	196.0
CFDShip-Iowa	322	322

URANS maneuvers correspond to conservative simulations with no under-relaxation and maximum allowable Courant numbers of just $C_{\max} = 2$. VOF simulations reported in Vukčević et al. (2014) using the IIHR model require roughly 72 CPU hours per PMM period. This is less computationally expensive than the fine grid, but the VOF simulations use a maximum Courant number of $C_{\max} = 50$. A similar setting would greatly increase the speed of the linearized URANS simulations.

The low computational expense required by the linearized URANS method makes it suitable for use on a multi-core workstation. Computing clusters are often inaccessible to designers. The ability to use machines already present in the workplace shows promise that RANS-based maneuvering simulations can be brought into engineering practice more immediately.

6.1.5 Flow Field Data

In this section, the linearized free-surface approach is used in conjunction with large eddy simulation (LES) and a grid of approximately four million cells for the pure sway maneuver. The turbulence model implemented is a dynamic one-equation eddy-viscosity model. The purpose of this investigation is to determine the effect of linearization on the flow around the hull. Results are compared to particle image velocimetry (PIV) data from IIHR. Five categories of data are presented, all in a ship-fixed reference frame. These are shown at four phases throughout one PMM period, as seen in Figure 6.11. The sampling location is the same for each moment in time and is located at $x/L_{\text{pp}} = 0.935$ from the bow. Quantities of a bow-aligned

axial velocity, a lateral velocity, a vertical velocity, an axial vorticity, and a turbulent kinetic energy are examined. All values have been non-dimensionalized using the carriage speed, $U = 1.531m/s$ and the model length, $L_{\text{pp}} = 3.048m$.

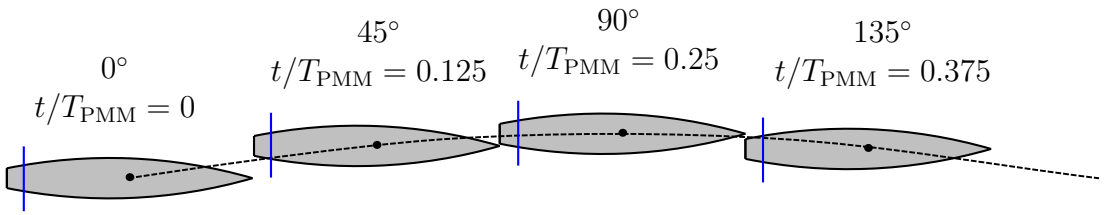

Figure 6.11: PIV sampling points and locations for pure sway

The effects of the linearization are most prevalent in Figure 6.12 which shows the axial velocity. The linearization neglects the perturbation velocity which is not small everywhere in the domain. In fact, it is equal to the ship velocity on the surface of the hull. This results in the large difference between the experimental and LES results. The PIV data also capture the vortex that the sonar dome generates. The first instance of this feature is seen directly below the keel in the first contour plot of Figure 6.12. For the most part, this vortex is not captured with the linearized LES method. It is likely that a finer grid is necessary to more accurately resolve the flow field data. More agreeable predictions are seen with the lateral velocity presented in Figure 6.13. The perturbation velocity in sway is not as large as in surge, so the effects of using a linear free-surface condition are not as noticeable. Again, the vortex from the sonar dome is not as apparent as in the PIV data. These general conclusions apply to the vertical velocity as well, shown in Figure 6.14. Qualitatively, the axial vorticity in Figure 6.15 is similar to the PIV data. However, the vorticity from the PIV shows distinct circular structures, whereas the linearized LES data are more elongated. Again, a probable cause for this is insufficient grid resolution. Lastly, the turbulent kinetic energy is displayed in Figure 6.16. Compared to the PIV figures, the numerical data are rather poor, especially in the last two phases in time. This may be due to an unresolved grid or an issue with the turbulence model.

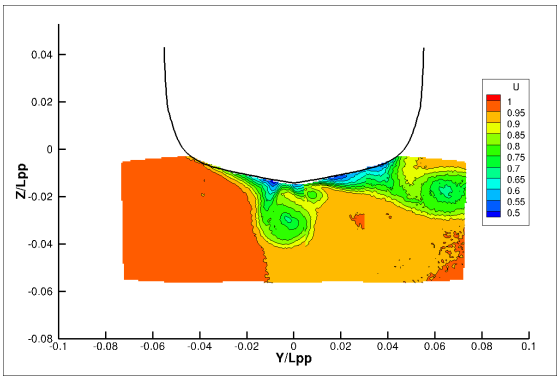

EFD at $t/T_{\mathrm{PMM}} = 0$

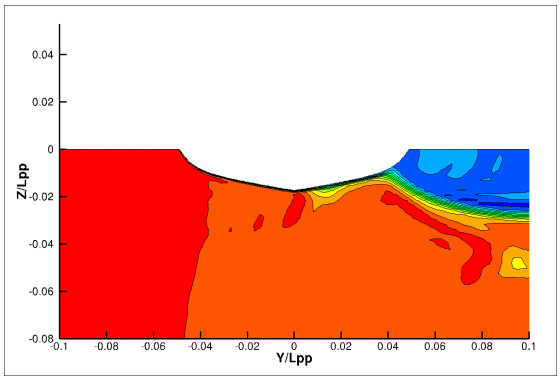

Linearized LES at $t/T_{\mathrm{PMM}} = 0$

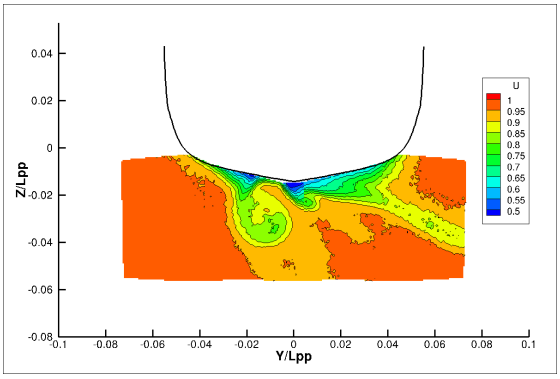

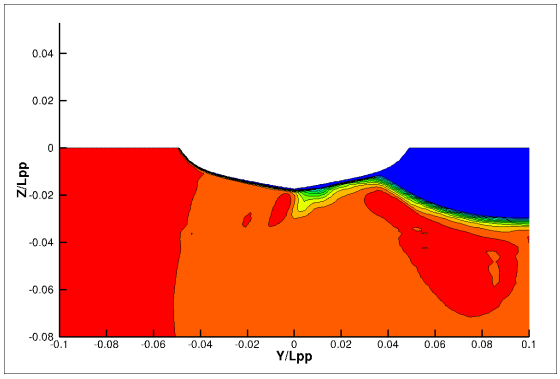

$t/T_{\mathrm{PMM}} = 0.125$

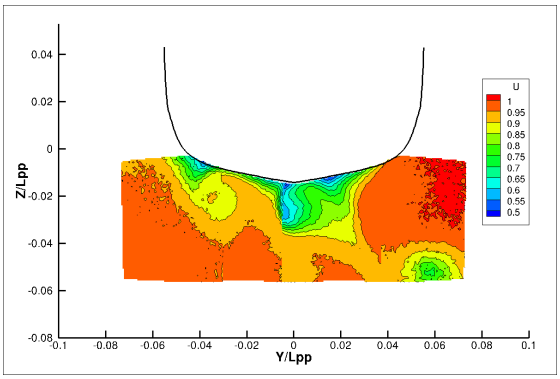

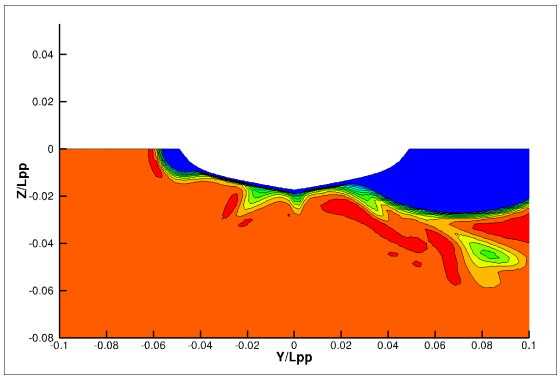

$t/T_{\mathrm{PMM}} = 0.25$

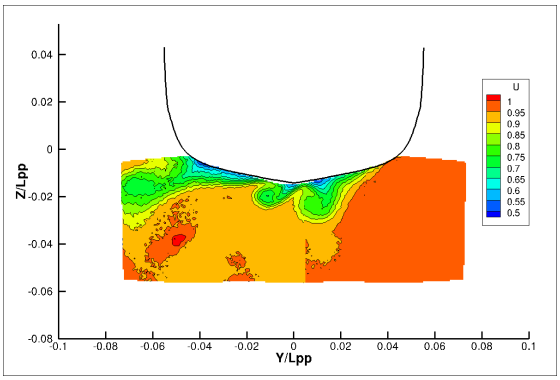

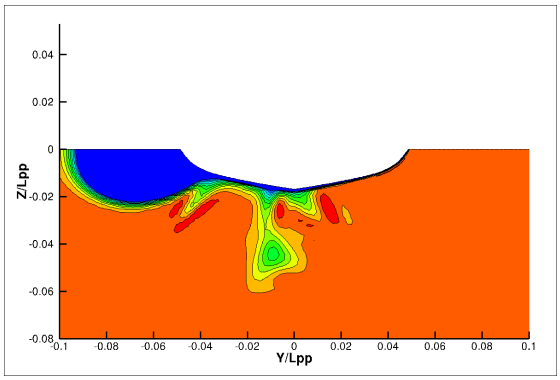

$t/T_{\mathrm{PMM}} = 0.375$

Figure 6.12: Axial velocity comparison

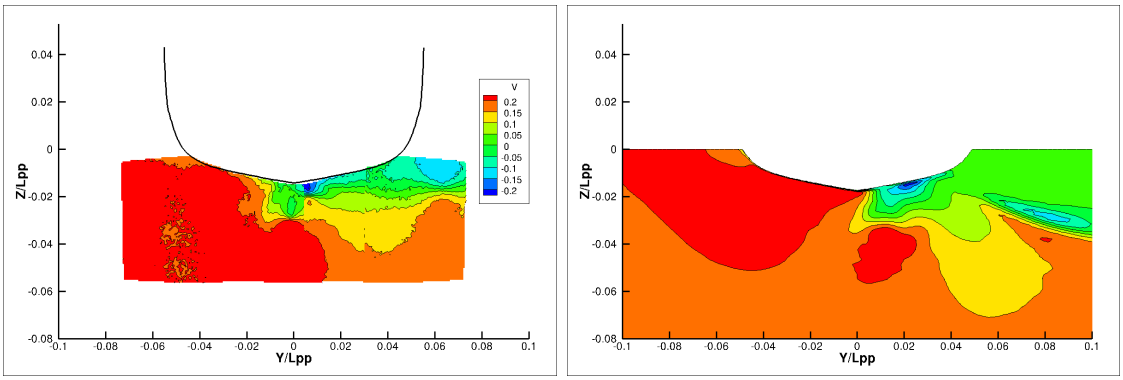

EFD at $t/T_{\mathrm{PMM}} = 0$ Linearized LES at $t/T_{\mathrm{PMM}} = 0$

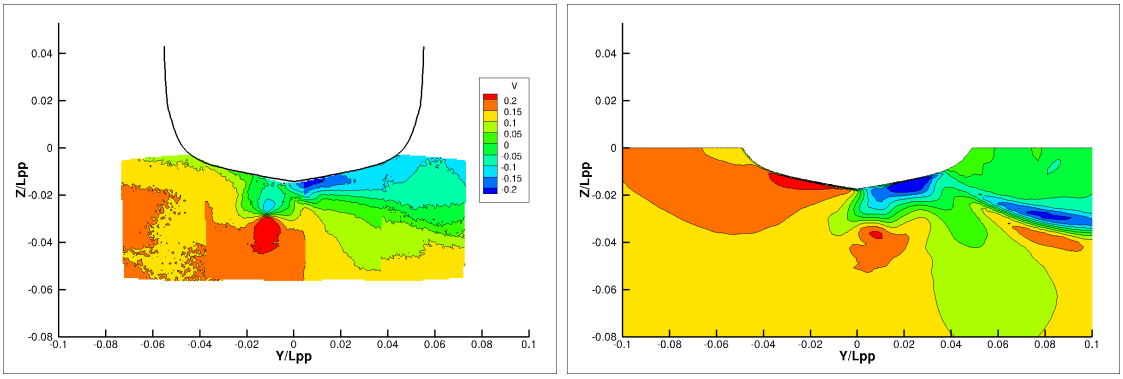

$t/T_{\mathrm{PMM}} = 0.125$

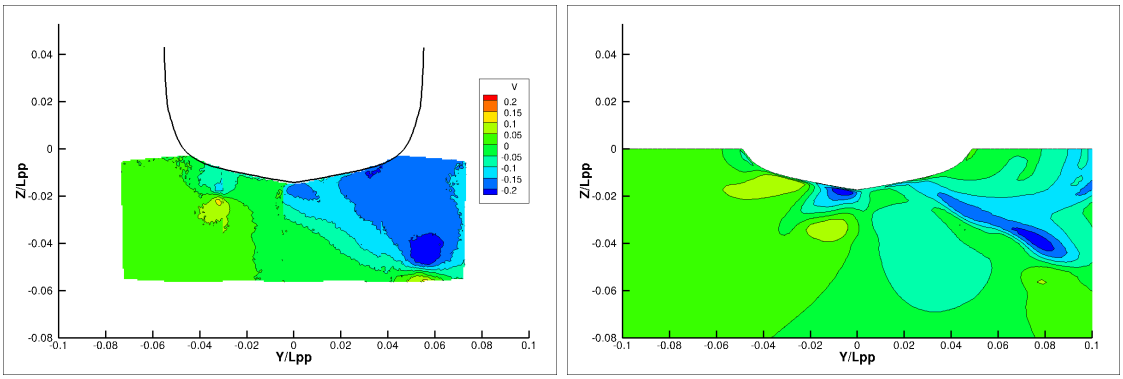

$t/T_{\mathrm{PMM}} = 0.25$

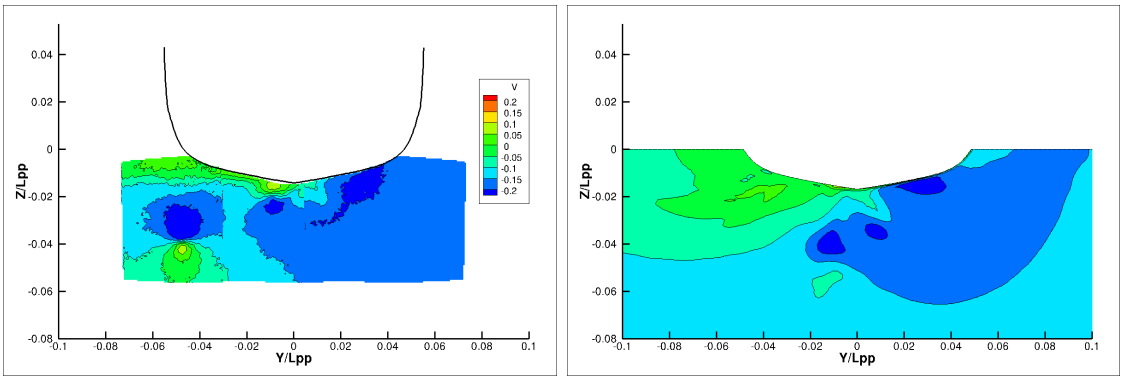

$t/T_{\mathrm{PMM}} = 0.375$

Figure 6.13: Lateral velocity comparison

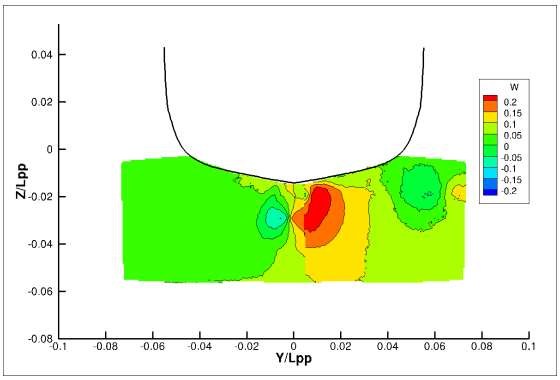

EFD at $t/T_{\mathrm{PMM}} = 0$

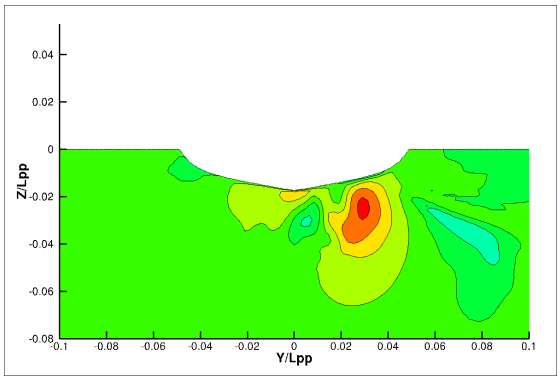

Linearized LES at $t/T_{\mathrm{PMM}} = 0$

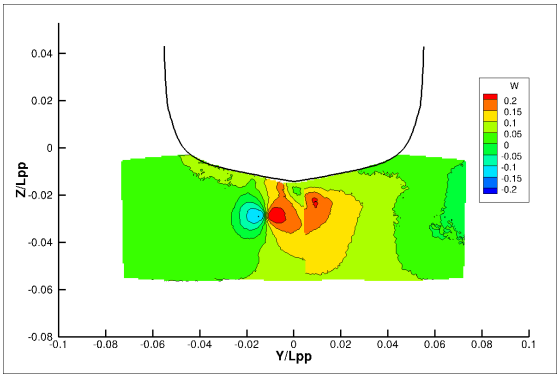

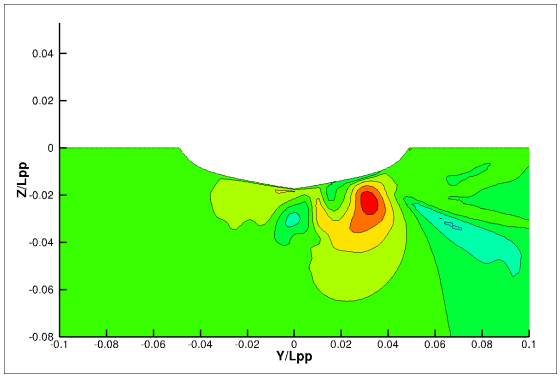

$t/T_{\mathrm{PMM}} = 0.125$

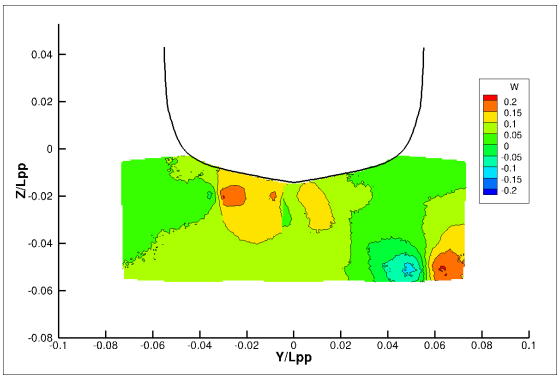

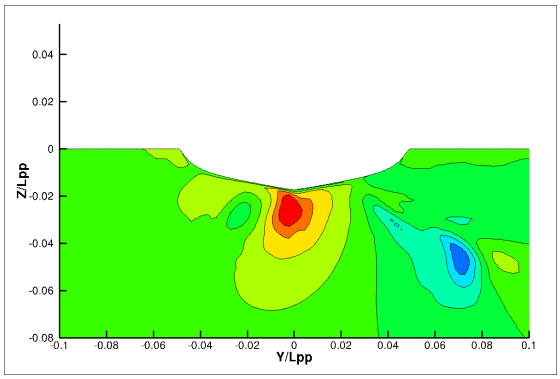

$t/T_{\mathrm{PMM}} = 0.25$

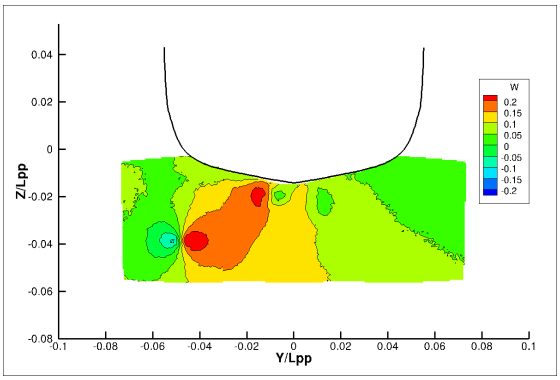

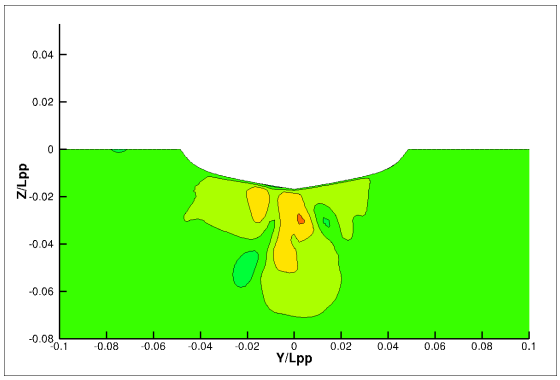

$t/T_{\mathrm{PMM}} = 0.375$

Figure 6.14: Vertical velocity comparison

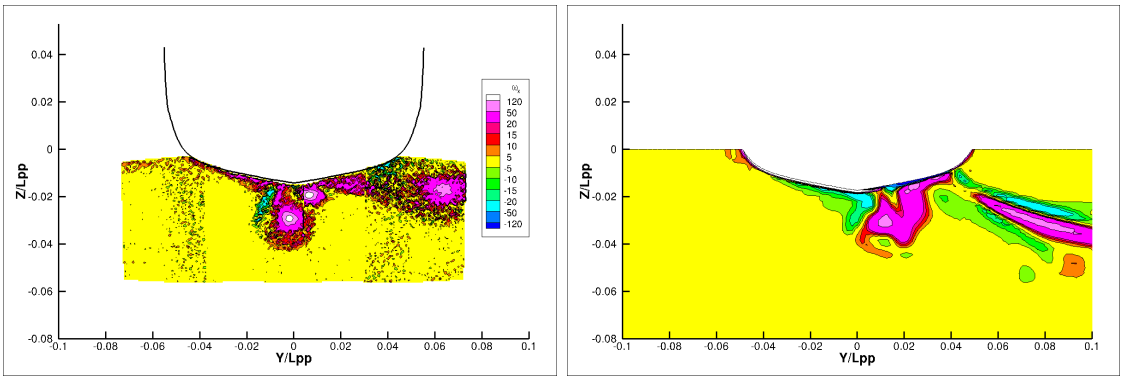

EFD at $t/T_{\mathrm{PMM}} = 0$ Linearized LES at $t/T_{\mathrm{PMM}} = 0$

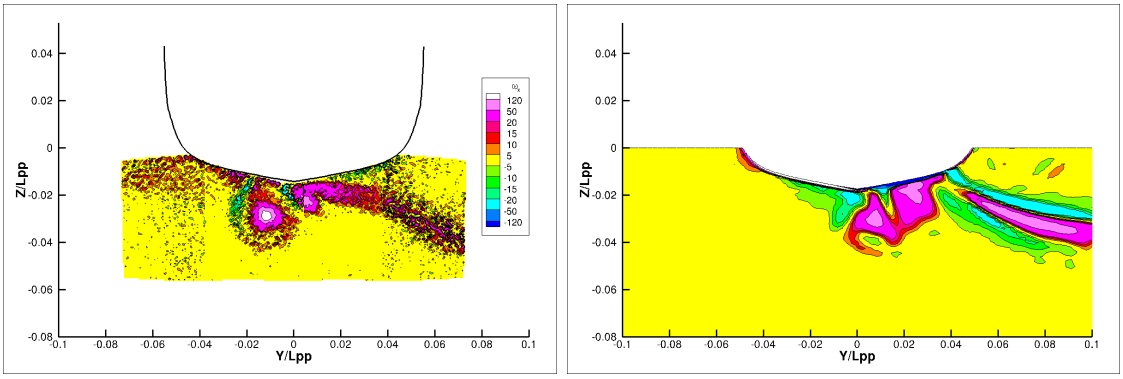

$t/T_{\mathrm{PMM}} = 0.125$

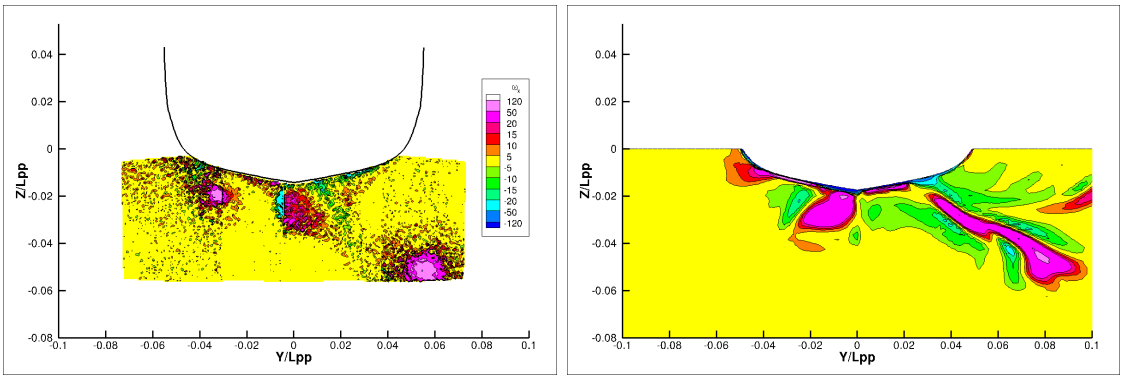

$t/T_{\mathrm{PMM}} = 0.25$

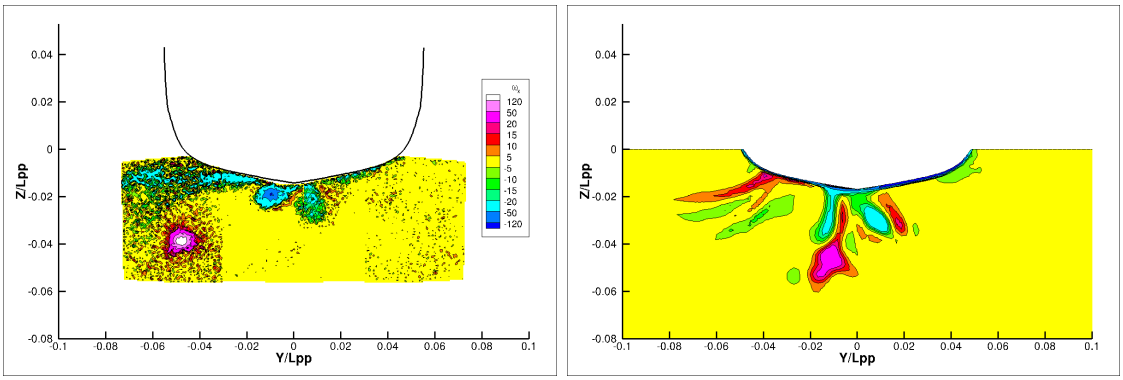

$t/T_{\mathrm{PMM}} = 0.375$

Figure 6.15: Axial vorticity comparison

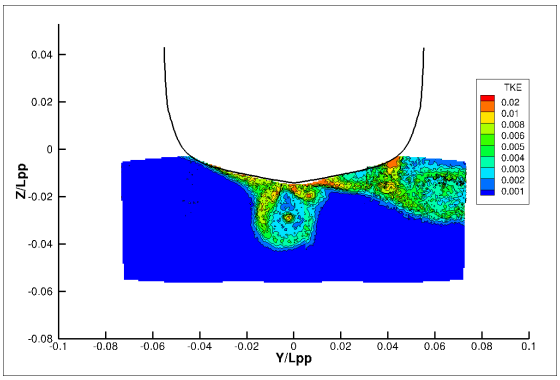

EFD at $t/T_{\mathrm{PMM}} = 0$

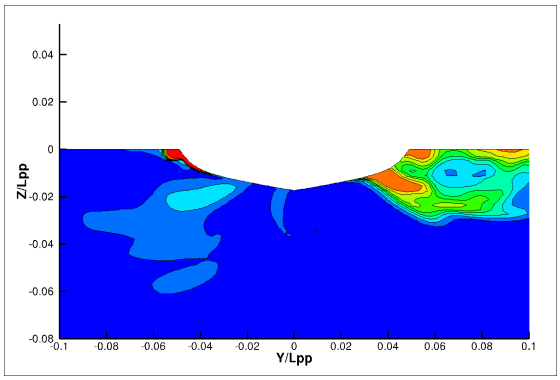

Linearized LES at $t/T_{\mathrm{PMM}} = 0$

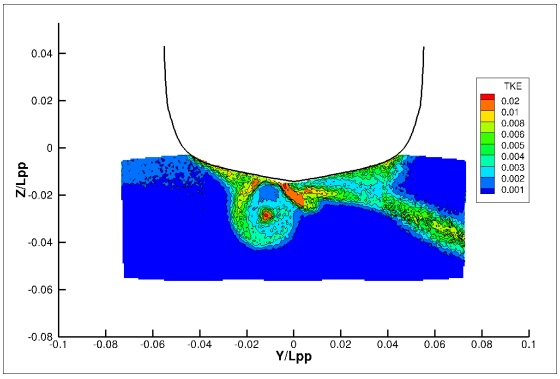

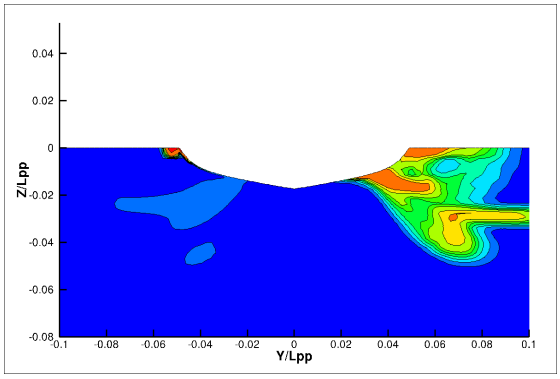

$t/T_{\mathrm{PMM}} = 0.125$

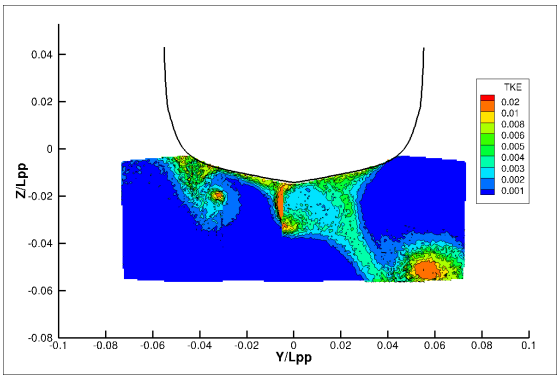

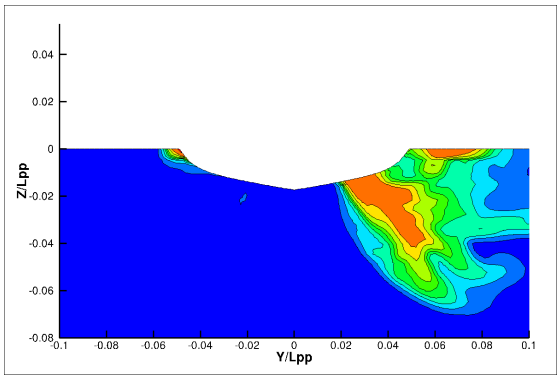

$t/T_{\mathrm{PMM}} = 0.25$

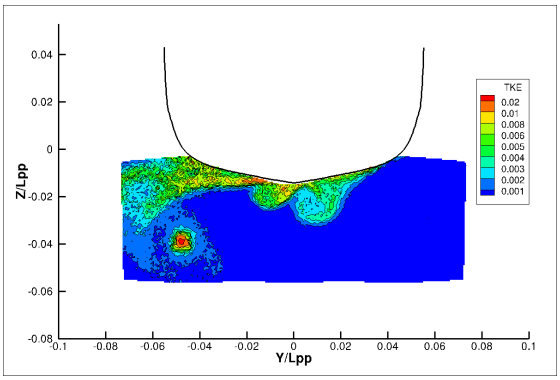

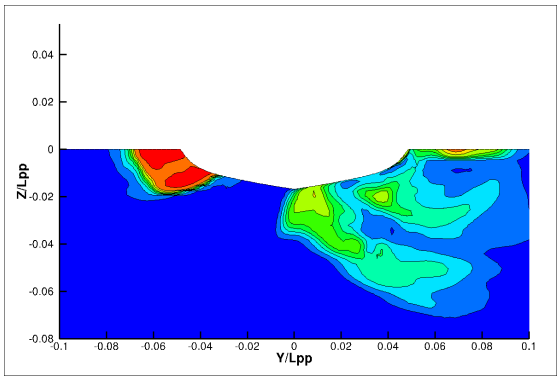

$t/T_{\mathrm{PMM}} = 0.375$

Figure 6.16: Turbulent kinetic energy comparison

6.2 DTMB 5415M - Appended Hull

This section contains results from a prescribed motion maneuver using the appended 5415M destroyer model. The simulation performed with the linearized URANS method is compared to experimental data obtained at MARIN and shown in Hallmann (2007). A photograph showing the stern region of the model is in Figure 6.17. The test performed is a static drift test with a drift angle of $\beta = 10°$. The propellers rotate during the test, but the rudders remain fixed at zero deflection angle. In addition to the many appendages, this model is approximately one meter longer than the bare hull. The model characteristics are shown in Table 6.7.

Figure 6.17: DTMB 5415M appended hull model from MARIN experiments

Table 6.7: MARIN DTMB 5415M model principle characteristics

Item	Symbol	Value	Unit
Scale factor	λ	35.480	
Length	L_{pp}	4.002	m
Waterline length	L_{wl}	4.007	m
Beam	B_{wl}	0.537	m
Draft	T	0.173	m
Lateral area	A_o	0.692	m^2
Propeller diameter	D	0.173	m
Num. of blades		5	

The complex geometry arising from the many appendages presents difficulties in grid generation as well as flow resolution. Figure 6.18 shows the hull, appendages, and free-surface on the coarse grid obtained with the semi-automatic mesh-generator native to OpenFOAM, snappyHexMesh. The edges of the appendages are defined well even with this coarse grid of less than 300,000 cells. The interaction between the appendages is an important feature of the maneuver, so a fine grid is used with a uniform refinement block in the stern region. This fine grid consists of just over 1.7 million cells. A summary of these grids appears in Table 6.8. All results discussed in this section correspond to those obtained with the fine grid.

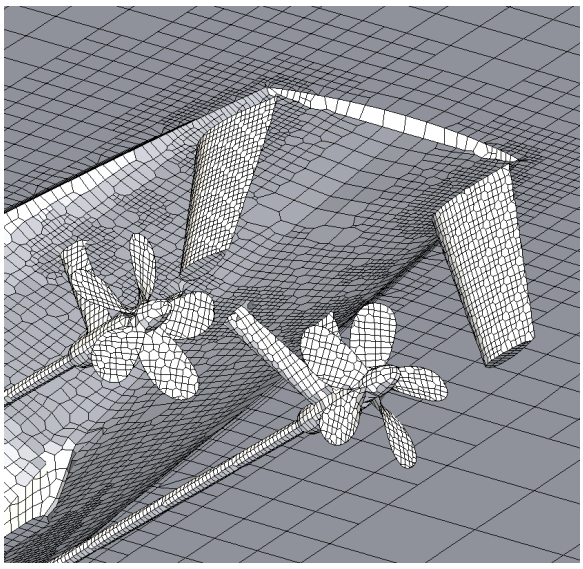

Figure 6.18: Coarse grid discretization of the stern region

Table 6.8: DTMB 5415M linearized URANS grid characteristics

	Cell Count	y^+_{avg}
Coarse	2.90×10^5	69.1
Fine	1.77×10^6	41.6

Table 6.9: DTMB 5415M maneuvering test parameters

Item	Symbol	Value	Unit
Model speed	U	1.554	m/s
Froude num.	Fr	0.248	
Reynolds num.	Re	5.19×10^6	
Gravity	g	9.81	m/s^2
Water density	ρ	1000	kg/m^3
Water viscosity	ν	1.00×10^{-6}	$\text{m}^2\text{/s}$
Static drift			
Drift angle	β	10	deg
Propeller freq.	n_{prop}	10.82	s^{-1}

The parameters of the maneuver performed with the appended hull are displayed in Table 6.9. The drift angle of the static drift test is the same as with the bare hull, $\beta = 10°$.

The dimensionless, global hydrodynamic forces from the static drift test are presented in Figure 6.19. There is a significant difference between the linearized URANS data and the experiments. Although these experiments are difficult to perform and replicate using physical models (for example, performing a symmetric test at $\beta = -10°$), there are several probable causes for the numerical forces not predicting those of the experiment. A main concern is the refinement and modeling of turbulence in the region of the appendages. This fine grid is likely under-resolved and poorly modeling the turbulence. Boundary layer prisms are not present on all the surfaces as they are difficult to generate on small, complex geometries such as the shafts, struts, and propellers. In addition, the Spalart-Allmaras turbulence model is employed with an adaptive wall function. These results may indicate that a wall function is not appropriate for this geometry, and lower y^+ restrictions should be implemented.

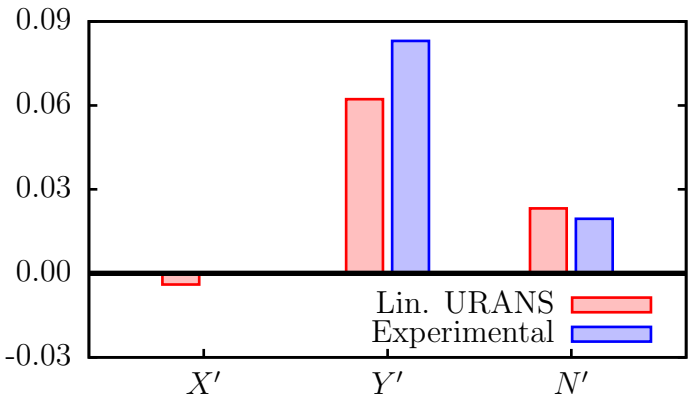

Figure 6.19: Force and moment comparison for linearized URANS fine grid and experimental static drift case

First, the sway force, Y', is approximately 25% under-predictive. If indeed this is due to the under-resolved grid, a finer grid may show a greater sway force on the appendages. A greater force in this location corresponds with a reduction in the yaw moment, which is currently over-predicted with the linearized URANS method. Lastly, the experiment shows a near-zero surge force due to the propeller thrust canceling the drag force. The linear results show a small negative surge force, indicating the propeller thrust is under-predicted. This is confirmed in Figure 6.20 where the thrust from each propeller is roughly 15% less than the experiment. Again, it is possible that a finer grid and turbulence modeling or wall function treatment should be reconsidered.

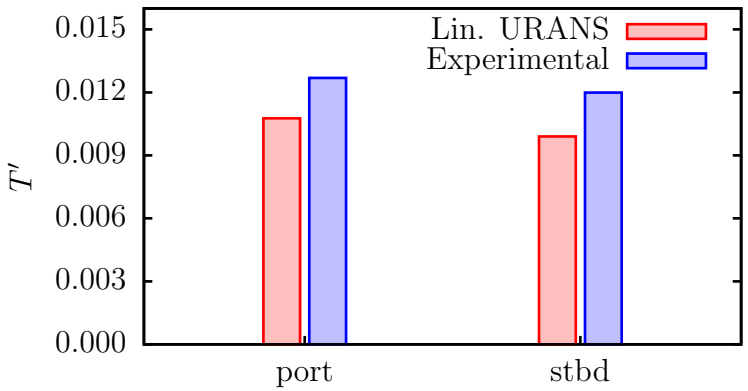

Figure 6.20: Propeller thrust from the fine grid during static drift compared to experimental value

Adding the difference in numerical and experimental thrust force to the surge force does result in a near-zero surge force, $X' = 0.005$. Nevertheless, the time series from the port-side propeller in Figure 6.21 shows a steady state is achieved with a time-averaged thrust, but there is a variation in force about this mean.

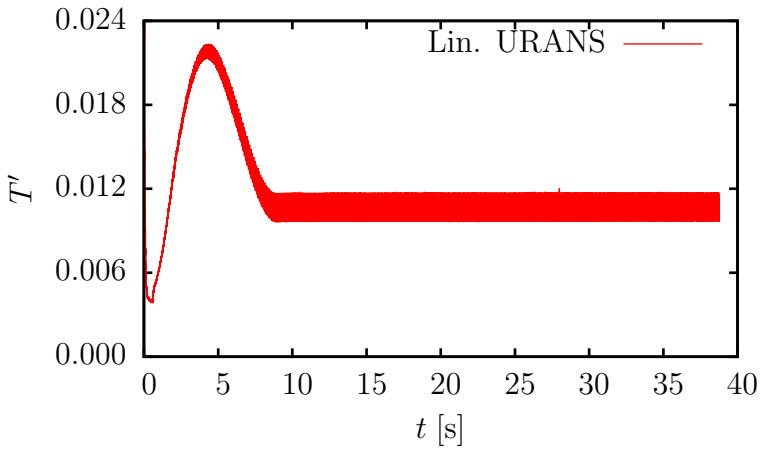

Figure 6.21: Propeller thrust during static drift over time

Closer inspection of the variation within the propeller thrust is displayed in Figure 6.22. Here, the impulses in the signal are seen to coincide with blade-passings. The propellers have five blades, so five impulses per revolution are produced. The angle of the A-frame bracket supporting the propeller shaft is such that blades simultaneously pass behind each leg of the bracket.

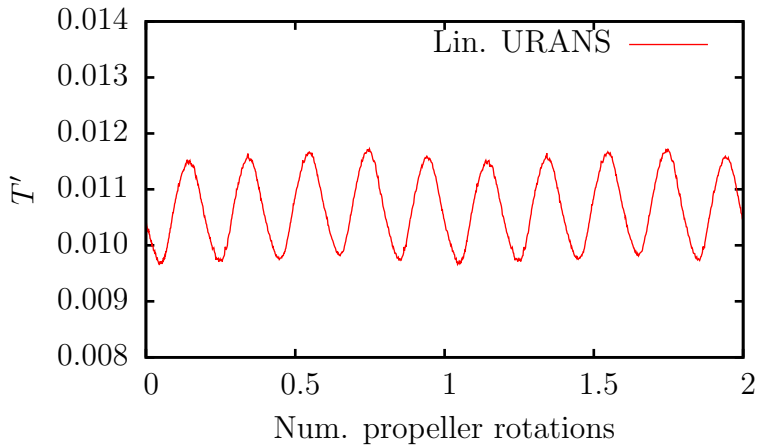

Figure 6.22: Propeller thrust during static drift showing impulses due to blade-passings

Overall, the difficulties with modeling an actual propeller and obtaining an accurate thrust suggest that alternatives such as a body force model may be a worthwhile pursuit with the linearized URANS method.

CHAPTER VII

Conclusions and Future Work

7.1 Summary

A linearized free-surface URANS method is shown to be a promising approach to accurately predicting ship maneuvering. The simplification of satisfying a first-order wave condition gives rise to computational savings compared to fully nonlinear methods, as there is far less of a need to resolve grids near the surface of the water. Grid convergence is more readily achieved using many fewer cells than required with fully nonlinear methods. The single-phase approach accounts for the viscous effects which are of great importance in maneuvering, especially the interactions between the hull, propellers, and rudders. Ship hulls with moving rudders and rotating propellers may be simulated with fully rigid meshes in an inertial, Earth-fixed frame of reference.

A viscous air-water interface study has been performed in a two-dimensional manner with a transom stern geometry. Typical flows produced in ship maneuvering are replicated by varying the acceleration due to gravity, g, and the molecular viscosity, μ. The range of transom-based Froude numbers tested ($Fr_T = 3$, $Fr_T = 2$, $Fr_T = 0.3$) result in a steady wave, an unsteady breaking wave, and a nearly flat air-water interface. A range of Reynolds numbers are also tested ($Re = 1e4$, $Re = 1e5$, $Re = 1e6$), but this has far less of an effect on the flow. Viscous terms are shown to simply scale linearly with the changes in molecular viscosity, μ. The findings from this study jus-

tify the use of linearized dynamic and kinematic free-surface boundary conditions in conjunction with the RANS variables for ship maneuvering prediction. The suitability of a linearized free-surface is further shown with a replication of the study using the linearized URANS method. The wave elevations at each Froude number compare well to those obtained with a fully nonlinear VOF method.

An initial test of the linearized URANS method in a ship-fixed reference frame is applied to a KCS hull model performing forward speed tests at a range of Froude numbers. The wave profile along the hull is compared against experiments, and the agreement is quite good. Slight differences at the transom may be improved with the use of the custom boundary condition for the free-surface elevation, imposed at the free-surface/body juncture, which these simulations do not employ. In addition, the sinkage and trim are calculated and shown to compare very well with the experimental data.

A David Taylor Model Basin 5415 destroyer hull is extensive tested with a variety of prescribed motion maneuvers. A bare hull version of the model, fitted only with bilge keels, undergoes static drift, pure sway, and pure yaw maneuvers. For the static drift simulations, the linearized URANS method is shown to require only a slight increase in computational expense of 10% compared to a double-body approximation. However, the linearized approach agrees with experimental data within 5% for the surge force, sway force, and yaw moment. The double-body approximation differs by over 20% for the sway force and yaw moment. The linearized URANS method continues to agree closely with experimental predictions for the pure sway and pure yaw maneuvers. Nonlinear simulations show little improvement in force predictions, and at times less accurate results are displayed. The computational expense required for the forces compared is up to 30 times less for the linearized URANS method than a fully nonlinear level-set approach.

The appended version of the DTMB 5415 hull is analyzed with a static drift

maneuvering test. The five-bladed propellers operate at the design speed rotation rate for each simulation. Results are not closely agreeable to the experimental data. It is possible that greater resolution is required near the transom which contains many appendages with complex geometries.

The results discussed in this thesis are an initial application and validation of the technology, but they have shown the linearized URANS method to be a viable option for ship designers compared to model tests and fully nonlinear CFD. Time and cost savings allow for an increased number of hull forms to be evaluated, which in turn provides a more complete exploration of a design space. Novel hull forms may be better suited for their needs due to a more optimized geometry. There exists much room for improvement with the linearized URANS method, but this only provides an opportunity for naval architects to improve the designs of the largest moving objects in the world.

7.2 Contributions

- It is demonstrated that the VOF method satisfies the air-water interface condition, with the stresses from the air and the water being small at the interface. The small values of stress from the air demonstrate the suitability of the free-surface assumption for ship maneuvering prediction. The terms within the total stress vector of the water are evaluated to determine which terms to include in a pressure boundary condition. For each case, it is shown that the viscous terms are extremely small and may be neglected. Furthermore, the hydrodynamic and hydrostatic pressures are shown to dominate. Therefore, assigning an inviscid, zero total pressure condition at the $z = 0$ calm-water plane is justified for the linearized URANS method.

- The linearized kinematic condition is shown to differ little from the nonlin-

ear condition and the actual condition from the solution of the transom stern studies. This truly quantitative investigation has further justified the use of a linearized kinematic condition for maneuvering simulations beyond the classical linearization procedures.

- A URANS maneuvering prediction toolkit employing a linearized free-surface has been developed. It is a single-phase finite-volume method built within the OpenFOAM environment. Several unique features are implemented in a custom fashion. A new pressure boundary condition coupled with a free-surface cell-extrusion solves the linearized dynamic and kinematic free-surface boundary conditions, respectively. These are solved in an inertial, Earth-fixed reference frame. Multiple new mesh motion functions exist allowing for pure sway, pure yaw, and free running model tests. Hulls with rotating propellers and moving rudders are also possible, and gradual motion development over time is used extensively in the new motion functions to aid in reducing problems associated with impulsive starts.

7.3 Future Work

All results generated with the linearized URANS method presented in this thesis are calculated with a maximum Courant number of just $C_{\max} = 2$. Stability issues arise with Courant numbers greater than two. Although the exact cause is not known, it is believed that this is from the implementation of the kinematic free-surface boundary condition and is a problem which can be overcome. Fully nonlinear methods can employ Courant numbers of $C_{\max} = 50$ for ship maneuvering problems. Therefore, investigating the cause of this instability with the linearized URANS method presents an opportunity to increase the computational efficiency of the method, possibly by an order of magnitude.

An additional source of instability is found within the quality of grids which may be used with the linearized URANS method. Grids which are seemingly suitable for computations in terms of non-orthogonality, skewness, resolution, et cetera, can result in diverging values of the free-surface elevation. This may be directly related to the issues previously described with increasing the maximum allowable Courant number. It may be possible that a unique investigation is required in order to determine the discretization requirements for applying the kinematic free-surface boundary condition.

The custom boundary condition used at the intersection of the body and the free-surface allows users to select an angle where the condition on the free-surface elevation transitions from a zero normal-gradient condition to a mixed condition. The angle is the difference between the body velocity and the body normal vector. The boundary condition should be further developed to include a another angle at which the condition becomes fixed-value. Currently, the condition only becomes fixed-value when the vectors are aligned. Additional development could include a feature which dynamically changes the boundary condition based on the magnitude of the body velocity. In other words, a dynamically changing fixed-value. This may be useful near the transom stern of an accelerating hull, where the free-surface elevation is initially at the calm waterline but gradually decreases as the vessel increases speed.

The linearized URANS method is studied extensively with prescribed motion maneuvers resembling those performed with PMMs. Rotating arm simulations are also of concern to designers due to the rotary maneuvering coefficients that may be obtained, and this is an area where the linearized URANS method could be further tested. In addition, free-running model tests are possible, and these self-propelled simulations are valuable for a number of reasons. They may provide knowledge of propeller meshing requirements for accurate thrust prediction which is important for achieving design speed in a self-propelled model test. Also, zig-zag and turning cir-

cle tests could indicate whether neglecting roll, heave, and pitch is still a suitable approximation.

Results from LES simulations are provided in this thesis, but subsequent studies may provide valuable insight about the extent to which the linearized free-surface changes the fluid flow for ship maneuvering. The method may be suitable for studies such as propeller inflow simulations while remaining less computationally burdensome than fully nonlinear LES.

Lastly, waves could be added to the linearized URANS tool to provide predictions for maneuvering in regular and irregular waves. The ability to perform these simulations in an efficient manner is extremely important to designers. A goal to motivate future work is to develop the capability to accurately and robustly perform full-scale, self-propelled maneuvers in an irregular seaway.

APPENDIX

APPENDIX A

Viscous Interface Study – Unsteady Breaking Wave

This appendix contains iso-surfaces from the unsteady breaking wave case in the two-dimensional transom stern canonical study. The transom-based Froude number is $Fr_T = 2$. Results are shown for Reynolds numbers of $Re = 1e5$ and $Re = 1e6$. A discussion of the results corresponding to $Re = 1e4$ appears in Chapter V. Four iso-surfaces are associated with each Reynolds number. First, two figures are used to display the dimensionless viscous stresses from the total stress vector. One is from the horizontal component of the of the vector and the other from the vertical component, in this form respectively:

$$\frac{\mid 2\mu_{\text{eff}} u_x q \mid + \mid \mu_{\text{eff}} \left(u_z + w_x\right) s \mid}{\frac{1}{2}\rho U^2} \tag{A.1}$$

$$\frac{\mid \mu_{\text{eff}} \left(w_x + u_z\right) q \mid + \mid 2\mu_{\text{eff}} w_z s \mid}{\frac{1}{2}\rho U^2} \tag{A.2}$$

The main conclusion from the investigation of the viscous stresses is that they are very small at the surface of the water. Additionally, the viscous terms scale linearly with changes in Reynolds number within the studied range ($Re = 1e5 - 1e6$). The

small magnitude of these terms suggests that they may be neglected when seeking appropriate boundary conditions for a free-surface approximation. Next, two figures are used to display the dimensionless hydrodynamic and hydrostatic pressures from the vertical component of the stress vector:

$$\frac{ps}{\frac{1}{2}\rho U^2} \tag{A.3}$$

$$\frac{\rho g \eta s}{\frac{1}{2}\rho U^2} \tag{A.4}$$

The most important observation from the hydrostatic and hydrodynamic pressure is that they are much greater than the viscous stresses at the surface of the water. They are the most influential terms when considering a suitable pressure boundary condition to apply with a free-surface approximation. Also, the iso-surface from the static pressure and dynamic pressure are nearly identical, indicating that they are in balance. Thus, collecting the dominant terms from the total stress vector results in a single, inviscid total pressure condition in the vertical direction:

$$p - \rho g \eta = 0 \tag{A.5}$$

This is the boundary condition used for the dynamic pressure at the free-surface of the linearized URANS method.

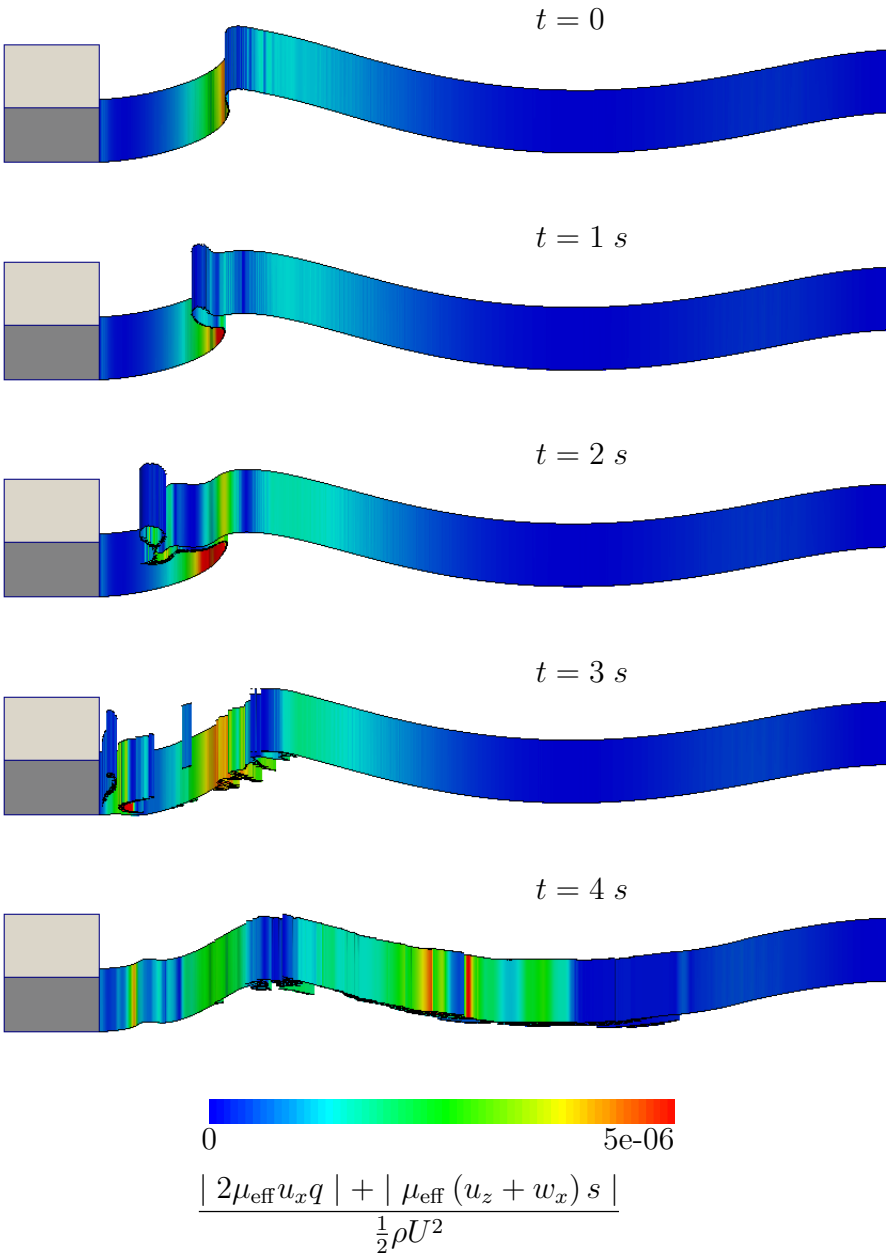

Figure A.1: Re=1e5, Magnitudes of the horizontal viscous stresses as the wave breaks

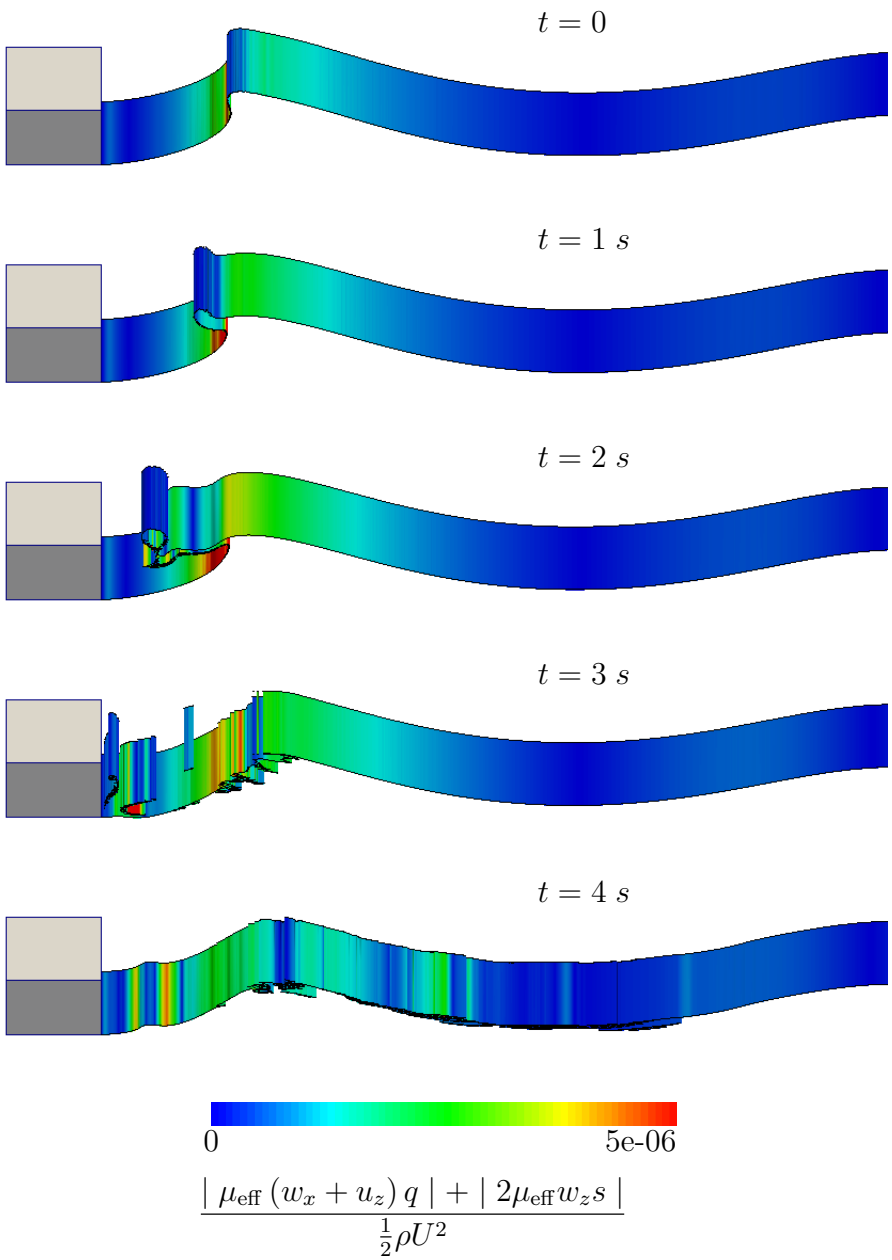

Figure A.2: Re=1e5, Magnitudes of the vertical viscous stresses as the wave breaks

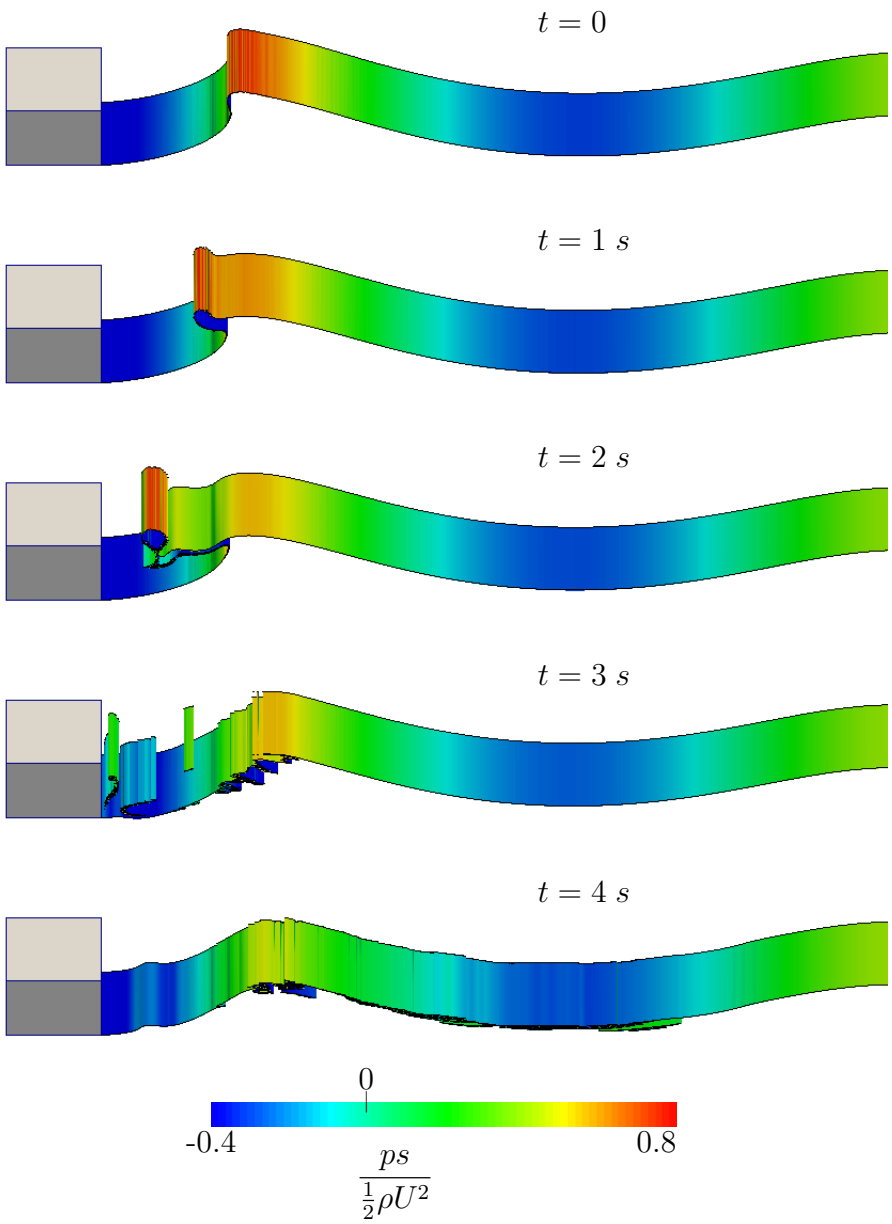

Figure A.3: Re=1e5, Hydrodynamic pressure as the wave breaks

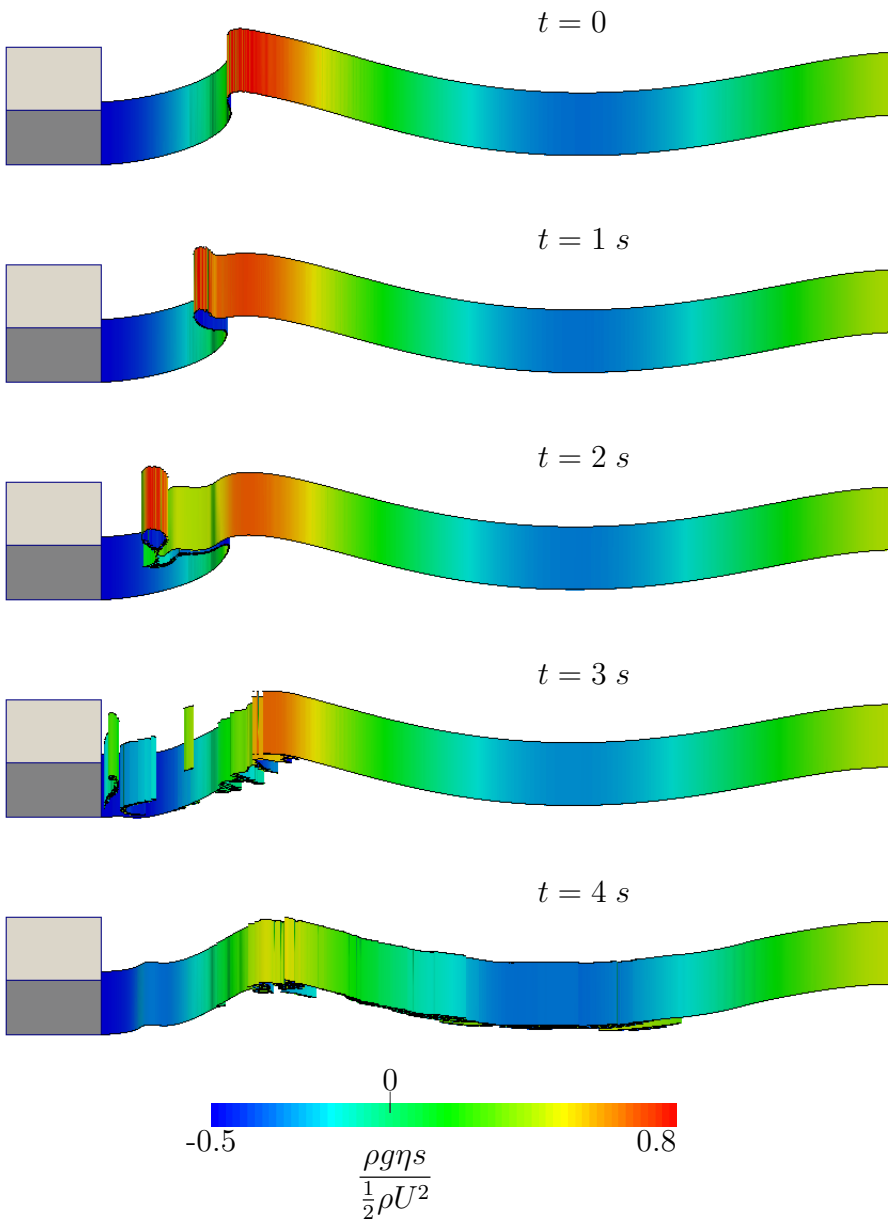

Figure A.4: Re=1e5, Hydrostatic pressure as the wave breaks

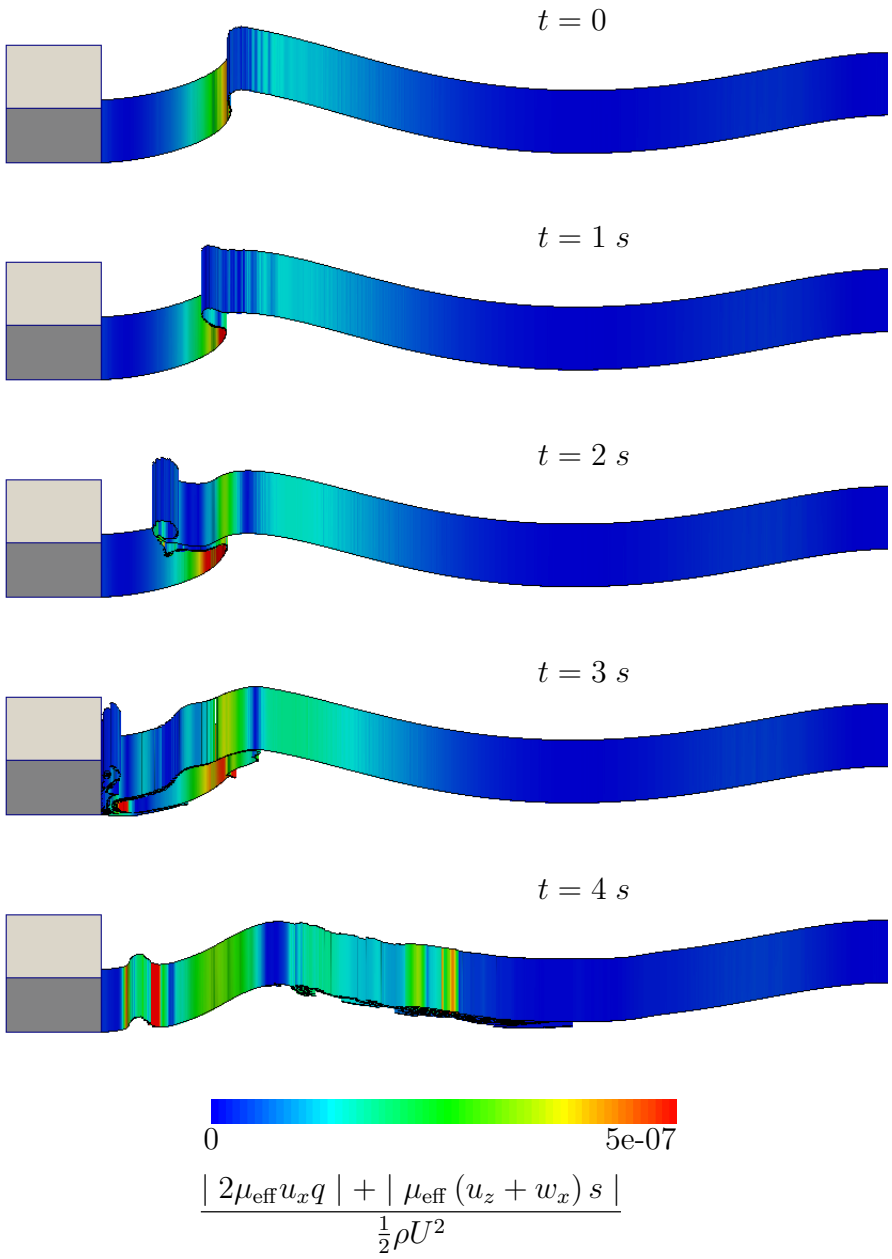

Figure A.5: Re=1e6, Magnitudes of horizontal viscous stresses as the wave breaks

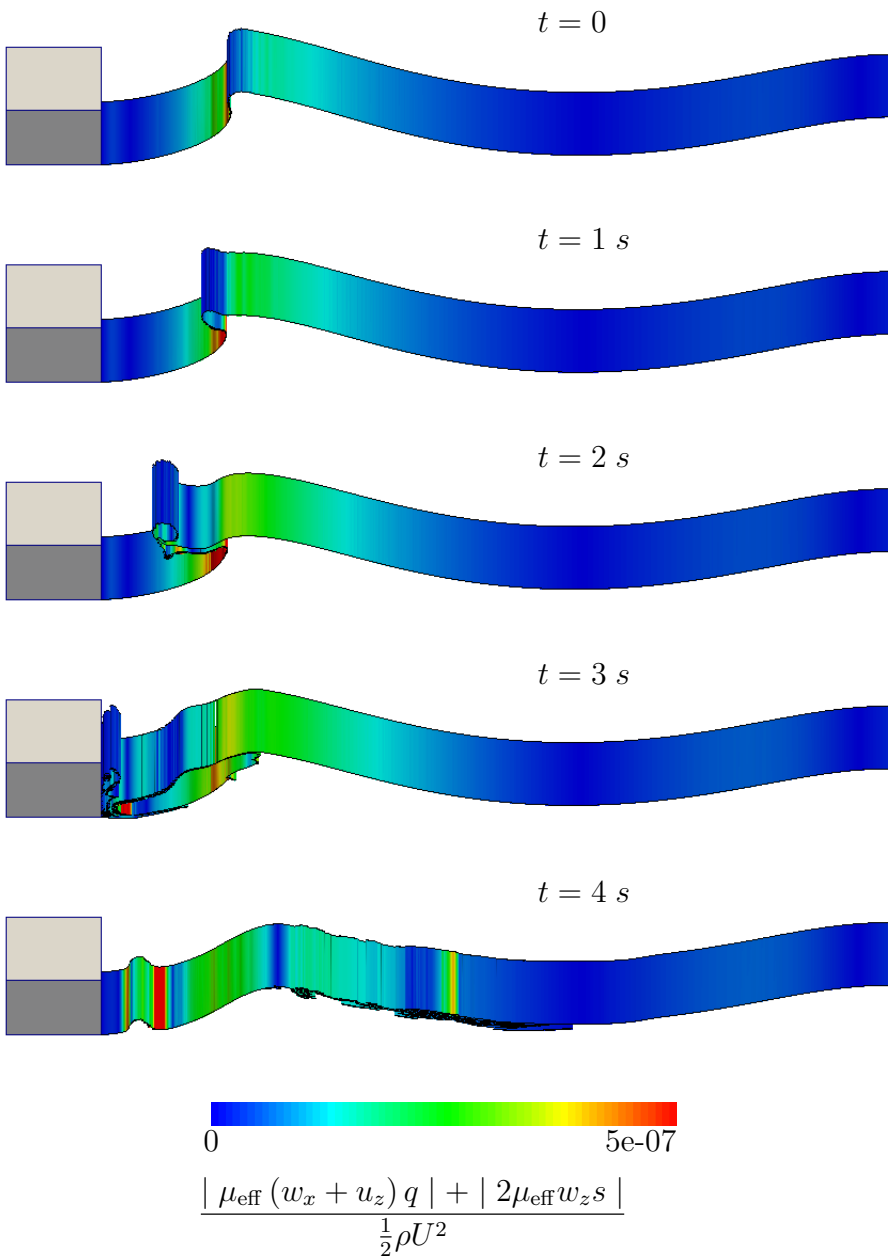

Figure A.6: Re=1e6, Magnitudes of vertical viscous stresses as the wave breaks

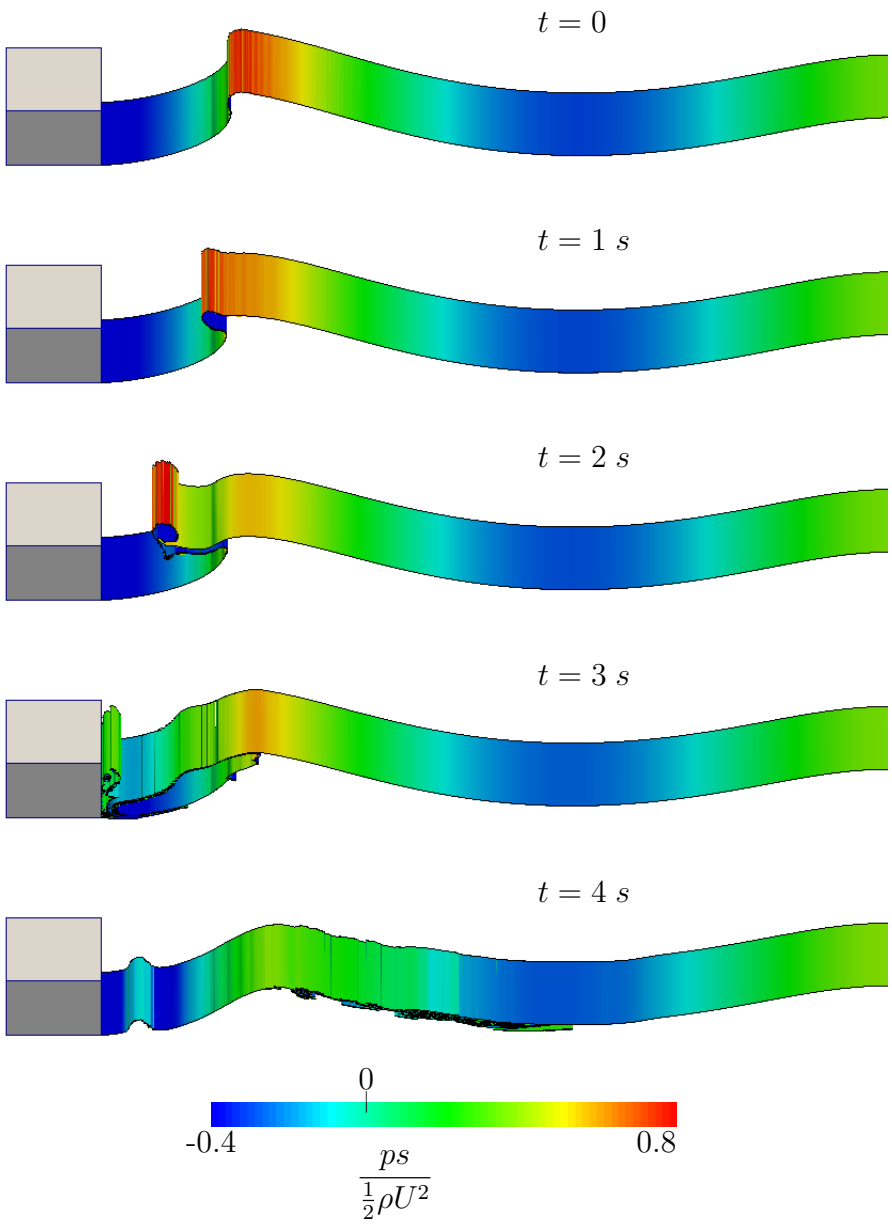

Figure A.7: Re=1e6, Hydrodynamic pressure as the wave breaks

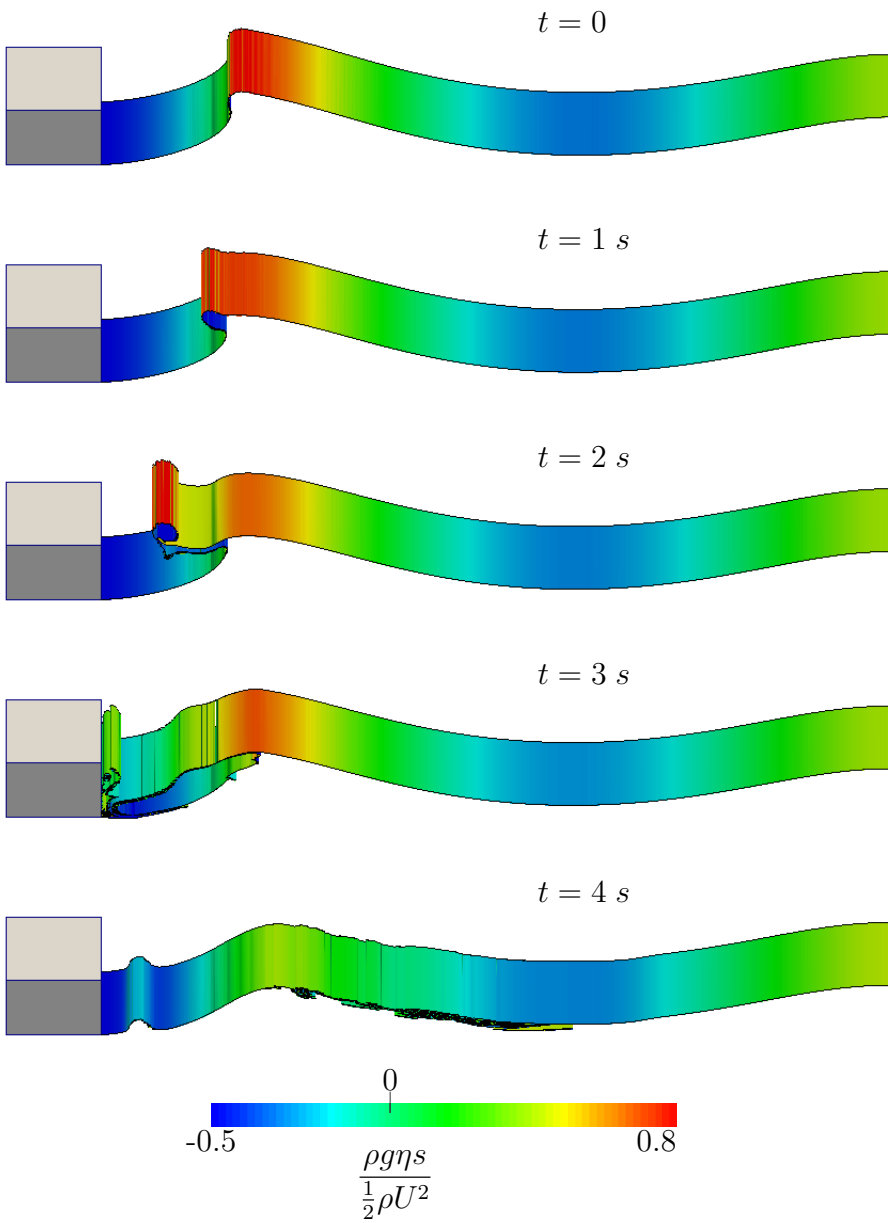

Figure A.8: Re=1e6, Hydrostatic pressure as the wave breaks

BIBLIOGRAPHY

BIBLIOGRAPHY

ABS. Guide for vessel maneuverability, March 2006.

Agdrup, K. Model test report. Technical report, FORCE Technology, Denmark, 2004.

Araki, M., Ohashi, K., and Hirata, N. KVLCC2 simulations with overset grid method. In Otzen and Simonsen (2014).

ASME. Procedure for estimation and reporting of uncertainty due to discretization in CFD applications, 2008.

Barton, I. E. Comparison of SIMPLE- and PISO-type algorithms for transient flows. *International Journal For Numerical Methods In Fluids*, 26:459–483, 1998.

Beck, R. F. and Loken, A. E. Three-dimensional effects in ship relative-motion problems. *Journal of Ship Research*, 33:261–268, 1989.

Beck, R. F., Newman, J. N., and Tuck, E. D. Hydrodynamic forces on ships in dredged channels. *Journal of Ship Research*, 19, 1975.

Belenky, V. and Falzarano, J. Rating-based maneuverability standards. Technical report, American Bureau of Shipping, 2006.

Broglia, R., Muscari, R., and Mascio, A. D. Numerical simulations of the pure sway and pure yaw motion of the kvlcc-1 and 2 tankers. In Stern and Agdrup (2008).

Broglia, R., Dubbioso, G., Durante, D., and Di Mascio, A. Simulation of turning circle by CFD: Analysis of different propeller models and their effect on manoeuvring prediction. *Applied Ocean Research*, 39:1–10, 2013.

Burg, C. O. E. and Marcum, D. L. Moving towards high-fidelity RANS calculations of maneuvering surface vessels using unstructured grids. In *8th International Conference on Numerical Ship Hydrodynamics*, 2003.

Carrica, P. M., Ismail, F., Hyman, M., Bhushan, S., and Stern, F. Turn and zigzag maneuvers of a surface combatant using a URANS approach with dynamic overset grids. *Journal of Marine Science and Technology*, 18(2):166–181, 2012.

Cope, D. M. Design of a free-running 1/30th Froude scaled model destroyer for in-situ hydrodynamic flow visualization. Master's thesis, Massachusetts Institute of Technology, 2012.

de Boer, J. Model making to the tune of 150 a year. Technical report, MARIN, 2009.

Eça, L. Discretization uncertainty estimation based on a least squares version of the grid convergence index. October 2006.

Farrell, P. and Maddison, J. Conservative interpolation between volume meshes by local Galerkin projection. *Computational Methods in Applied Mechanics and Engineering*, 200:89–100, 2011.

Filip, G. P. *High-Resolution Numerical Simulation of Turbulent Interfacial Marine Flows*. PhD thesis, University of Michigan, 2013.

Furukawa, Y., Nakiri, Y., Kijima, K., and Ibaragi, H. The prediction of the manoeuvrability of KVLCC1 and KVLCC2. In Stern and Agdrup (2008).

Gillespie, J. W. *A Network Science Approach to Understanding and Generating Ship Arrangements in Early-Stage Design*. PhD thesis, University of Michigan, 2012.

Hallmann, R. Applicability rotating arm: validation and extension of the rotating arm functionality in the seakeeping and manoeuvring basin. Technical report, MARIN, 2007.

Havelock, T. H. The resistance of a ship among waves. In *Proceedings of the Royal Society of London*, volume 161 of *Series A, Mathematical and Physical Sciences*, pages 299–308. The Royal Society, August 1937.

Havelock, T. H. The pressure of water waves upon a fixed obstacle. In *Proceedings of the Royal Society of London*, volume 175 of *Series A, Mathematical and Physical Sciences*, pages 409–421. The Royal Society, July 1940.

Hirt, C. W. and Nichols, B. D. Volume of fluid (VOF) method for the dynamics of free boundaries. *Journal of Computational Physics*, 39:201–225, 1981.

Hochbaum, A. C., Vogt, M., and Gatchell, S. Manoeuvering prediction for two tankers based on RANS simulations. In Stern and Agdrup (2008).

Holtrop, J. and Mennen, G. G. J. A statistical power prediction method. *International Shipbuilding Progress*, 25:253–256, 1978.

Holtrop, J. and Mennen, G. G. J. An approximate power prediction method. *International Shipbuilding Progress*, 29:166–170, 1982.

Hong, W. and Walker, D. T. Reynolds-averaged equations for free-surface flows with application to high-Froude-number jet spreading. *J. Fluid Mech.*, 417:183–209, 2000.

IMO. Explanatory notes to the standards for ship manoeuvrability, 2002.

Issa, R. J. Solutions of the implicitly discretised fluid flow equations by operator-splitting. *Journal of Computational Physics*, 1986.

ITTC. Recommended procedures - testing and extrapolation methods: Manoeuvrability: Free-sailing model test procedure, 2002.

Jasak, H. *Error Analysis and Estimation for the Finite Volume Method with Applications to Fluid Flows*. PhD thesis, Imperial College, University of London, 1996.

Kelvin, B. On ship waves. In *Institution of Mechanical Engineers*. Institution of Mechanical Engineers, 1887.

Kim, K. Simulation of surface ship dynamics using unsteady RANS codes. Technical report, Office of Naval Research, 2002.

Kim, S. Y. and Kim, Y. G. Prediction of maneuvering performance for KVLCC1 and KVLCC2 based on PMM data. In Stern and Agdrup (2008).

Kring, D. C., Parish, M. K., Milewski, W. M., and Connell, B. S. H. Simulation of maneuvering in waves for a high-speed surface effect ship. In *11th International Conference on Fast Sea Transportation*. Navatek, Ltd, September 2011.

Lafaurie, B., Nardone, C., Scardovelli, R., Zaleski, S., and Zanetti, G. Modeling merging and fragmentation in multiphase flows with SURFER. *Journal of Computational Physics*, 113:134–147, 1994.

Lincoln, C. C., Eda, H., and Landsburg, A. C. *Principles of Naval Architecture: Volume III - Motions in Waves and Controllability*. The Society of Naval Architects and Marine Engineers, 1989.

Longo, J., Yoon, H.-S., Toda, Y., and Stern, F. Phase-averaged 3DPIV/wave elevations and force/moment measurements for surface compatant in PMM maneuvers. In *Proc. 26th ONR Symposium on Naval Hydrodynamics*, Rome, Italy, 2006.

Maki, K. J. *Transom Stern Hydrodynamics*. PhD thesis, University of Michigan, 2006.

Maki, K. J. and Wilson, W. M. Steady drift force calculation on the naval destroyer hull 5415. In Stern and Agdrup (2008).

McNaughton, J., Afgan, I., Apsley, D. D., Rolfo, S., Stallard, T., and Stansby, P. K. A simple sliding-mesh interface procedure and its application to the CFD suimulation of a tidal-stream turbine. *International Journal For Numerical Methods In Fluids*, 74:250–269, 2014.

Miller, R. W. PMM calculations for the bare and appended DTMB 5415 using the RANS solver CFDSHIP-IOWA. In Stern and Agdrup (2008).

Newman, J. N. and Tuck, E. O. Hydrodynamic interaction between two ships. In *Proceedings of the 10th Symposium on Naval Hydrodynamics*, pages 35–70, 1974.

Noblesse, F. and Yang, C. Elementary water waves. *Journal of Engineering Mathematics*, 59:277–299, 2007.

Noblesse, F., Delhommeau, G., Huang, F., and Yang, C. Practical mathematical representation of the flow due toa distribution of sources on a steadily advancing ship hull. *Journal of Engineering Mathematics*, 71:367–392, 2011.

Noblesse, F., Huang, F., and Yang, C. The Neumann-Kelvin theory of ship waves. *Journal of Engineering Mathematics*, 79:1–20, 2013.

Otzen, J. F. and Simonsen, C. D., editors. *Proceedings SIMMAN 2014 Workshop*, Copenhagen, Denmark, December 2014.

Parsons, M. G., Chung, H., Nick, E., Daniels, A., Liu, S., and Patel, J. Intelligent ship arrangements: A new approach to general arrangement. *Naval Engineers Journal*, 120:51–65, 2008.

Pivano, L. *Thrust Estimation and Control of Marine Propellers in Four-Quadrant Operations*. PhD thesis, Norwegian University of Science and Technology, April 2008.

Rood, E. P. *Fluid Vortices*, volume 30. Springer Netherlands, 1995.

Rosemurgy, W. J., Edmund, D. O., Maki, K. J., and Beck, R. F. A velocity decompostion approach for steady free-surface flow. In *29th Symposium on Naval Hydrodynamics*. The National Academies Press, August 2012.

Salvesen, N., Tuck, E. D., and Faltinson, O. Ship motions and sea loads. In *The Sociecty of Naval Architects and Marine Engineers*, 1970.

Sclavounos, P. D. and Thomas, B. S. Optimal control theory applied to ship maneuvering in restricted waters. *Journal of Engineering Mathematics*, 58:301–315, 2007.

Shen, L., Zhang, X., Yue, D. K. P., and Triantafyllou, G. S. The surface layer for free-surface turbulent flows. *J. Fluid Mech.*, 386:167–212, 1999.

Shen, L., Triantafyllou, G. S., and Yue, D. K. P. Turbulent diffusion near a free surface. *J. Fluid Mech.*, 407:145–166, 2000.

Shen, L., Zhang, C., and Yue, D. K. P. Free-surface turbulent wake behind towed ship models: experimental measurements, stability, analyses and direct numerical simulations. *J. Fluid Mech.*, 469:89–120, 2002.

Shen, Z., Wan, D., and Carrica, P. M. RANS simulations of free maneuvers with moving rudders and propellers using overset grids in OpenFOAM. In Otzen and Simonsen (2014).

Simonsen, C. D., Otzen, J. F., Klimt, C., Larsen, N. L., and Stern, F. Maneuvering predictions in the early design phase using CFD generated PMM data. In *29th Symposium on Naval Hydrodynamics*, August 2012.

Singer, D. J., Doerry, N., and Buckley, M. E. What is set-based design? *Naval Engineers Journal*, 121:31–43, 2009.

Söding, H. Limits of potential theory in rudder flow predictions. In *22nd Symposium on Naval Hydrodynamics*. The National Academies Press, 1999. ISBN 9780309065375.

Spalart, P. R. and Allmaras, S. R. A one-equation turbulence model for aerodynamic flows. In *AIAA Meeting 92-0439*, January 1992.

Stern, F. and Agdrup, K., editors. *Proceedings SIMMAN 2008 Workshop*, Copenhagen, Denmark, 2008.

Strock, J. and Brown, A. Methods for naval ship concept and propulsion technology exploration in a CGX case study. *Naval Engineers Journal*, 120:95–122, 2008.

Tanizawa, K. and Naito, S. An application of fully nonlinear numerical wave tank to the study on chaotic roll motions. In Chung, J. S., Matsui, T., Naito, S., and Sayed, M., editors, *Proceedings of the Eighth (1998) International Offshore and Polar Engineering Conference*, volume 3, pages 280–287. International Society of Offshore and Polar Engineers, May 1998.

Toxopeus, S. L. Deriving mathematical manoeuvring models for bare ship hulls using viscous flow calculations. *Journal of Marine Science and Technology*, 14:30–38, 2009.

Turnock, S. R., Phillips, A. B., and Furlong, M. URANS simulations of static drift and dynamic manouveres of the KVLCC2 tanker. In Stern and Agdrup (2008).

Ueno, M., Tsukada, Y., and Kitagawa, Y. Rudder effectiveness correction for scale model ship testing. *Ocean Engineering*, 92:267 – 284, 2014.

van Brummelen, H. *Numerical Methods for Steady Viscous Free-Surface Flows*. PhD thesis, University of Amsterdam, 2002.

Vukčević, V., Östman, A., and Jasak, H. Rapid simulations of pure sway motion using FVM in OpenFOAM. In Otzen and Simonsen (2014).

Wang, H., Tian, X., Zou, Z., and B., W. Experimental and numerical researches on the viscous hydrodynamic forces acting on a KVLCC2 model in oblique motion. In Stern and Agdrup (2008).

Yeh, H. *Advances in Coastal and Ocean Engineering*. World Scientific Publishing, 1995.